Measurement of the Production and Muonic Decay Rate of W and Z Bosons in $p\bar{p}$ collisions at $\sqrt{s} = 1.8\,\mathrm{TeV}$ with the DØ Detector

Cecilia Elena Gerber

A Dissertation to be presented

In Partial Fulfillment of the Requirements

For the Degree of

Doctor of Philosophy in Physics

Universidad de Buenos Aires
Argentina

1994

This document is the english version of the PhD thesis "Determinación de las secciones eficaces de producción de los bosones W y Z en su decaimiento muónico en colisiones $\overline{p}p$ a $\sqrt{s} = 1.8$ TeV con el detector DØ" to be presented in the Universidad de Buenos Aires. Quotations from this dissertation are allowable, provided that accurate acknowledement of source is made.

Abstract

A measurement of the W and Z bosons production cross sections in their muonic channel is presented for $p\bar{p}$ collisions at $\sqrt{s} = 1.8$ TeV. The value for the total width of the W boson $(, _W)$ is extracted from the cross sections ratio. The analysis is based on 13.4 ± 1.6 pb^{-1} of data recorded during the first collider run of the DØ detector at the Fermi National Accelerator Laboratory Tevatron in 1992–1993. The obtained results

$$\sigma B(W \to \mu\nu) = 1.86 \pm 0.06(stat) \pm 0.19(sys) \pm 0.22(lum) \text{ nb},$$

$$\sigma B(Z \to \mu\mu) = 0.155 \pm 0.020(stat) \pm 0.016(sys) \pm 0.019(lum) \text{ nb},$$

$$R \equiv \frac{\sigma B(W \to \mu\nu)}{\sigma B(Z \to \mu\mu)} = 12.0^{+1.8}_{-1.4}(stat) \pm 1.0(sys),$$

$$, _W = 1.83 \pm 0.24(stat) \pm 0.15(syst) \pm 0.05(theory + LEPsyst) \text{ GeV},$$

are in good agreement with other experimental determinations as well as with theoretical predictions.

Acknowledgements

As a member of the DØ experiment, I am grateful to each of the almost 400 collaborators without whose time and effort, in both large and small ways, this work would not have been possible. In particular I would like to thank the members of the muon system and the WZ physics group, for their constant support during my years as a graduate student in DØ .

I am especially grateful to Paul Quintas and Darien Wood, with whom I shared long hours of work and discussion that lead to the completion of this analysis. It would not have been possible without their tireless efforts. In particular I would like to thank Darien for taking the time to read the drafts of this thesis and to thoroughly answer all my questions.

I would like to thank my advisor in Buenos Aires, Ricardo Piegaia, for giving me the oportunity to do research in a place like Fermilab. I am also extremely grateful to my advisor at DØ , Gene Fisk, for taking such good care of me.

Finally, I would like to thank my husband Daniel Elvira for sharing the last seven years of his life with me. I would have never made it without his love and support.

I dedicate this work to my parents,

Elena and Adolfo,

and to my husband,

Daniel.

Contents

1 Introduction **1**
- 1.1 The Standard Model 2
- 1.2 IVB production in hadron colliders 5
- 1.3 Description of the Analysis 13

2 Experimental Description **17**
- 2.1 The Tevatron at Fermilab 17
- 2.2 The DØ detector 19
  - 2.2.1 The DØ central detector 21
  - 2.2.2 The DØ calorimeter 24
  - 2.2.3 The DØ muon detection system 25
  - 2.2.4 Trigger and Data Acquisition 31
- 2.3 Luminosity Monitoring at DØ 33

3 Event Reconstruction **37**
- 3.1 Interaction Vertex Determination 37
- 3.2 Muon Reconstruction 38
- 3.3 Jet Reconstruction 41
- 3.4 Missing Transverse Energy Determination 42
- 3.5 Example of reconstructed events 43

4 Monte Carlo Event Simulation **47**
- 4.1 Event Generators 48
- 4.2 Detector Simulation 49
- 4.3 Trigger Simulation 50
- 4.4 Realistic detector effects 51

5 Event Selection **57**
- 5.1 Offline Muon Identification 57
  - 5.1.1 Loose Muon Definition 59
  - 5.1.2 Tight Muon Definition 64
- 5.2 Candidate Samples Selection 73

5.2.1 Data set used 73
5.2.2 Event Selection 74

6 Efficiencies and Backgrounds **77**
6.1 Selection Efficiencies 77
6.1.1 "Loose" Muon Efficiency 77
6.1.2 Trigger Efficiency 81
6.1.3 "Tight" Muon Efficiency 86
6.2 Background Estimates 88
6.2.1 Cosmic Background 88
6.2.2 QCD Background 90
6.2.3 Physics Backgrounds 93

7 Cross Sections **97**
7.1 $W \to \mu\nu$ and $Z \to \mu\mu$ candidate samples 97
7.2 Cross Section Measurements 103
7.3 Measurement of R and , $_W$ 105

8 Conclusions **111**

A Comparison of efficiencies as derived from data, default Monte Carlo and smeared Monte Carlo. **113**

B Summary of Acceptance and Efficiencies. **117**

List of Figures

1.1 Lowest order diagrams for the hadronic production of Intermediate Vector Bosons: (a) The Drell–Yan process, (b) The QCD annihilation process, (c) The QCD Compton process. 7

1.2 The Z decay into a pair of charged leptons can be directly identified through a peak in the dilepton invariant mass distribution. This distribution corresponds to Monte Carlo simulated events that do not include the detector resolution. 9

1.3 The transverse momentum spectrum of the decay products from a W decay peaks at about half the value of the W mass for the charged lepton (left) and for the neutrino (right). This distributions correspond to Monte Carlo simulated events that do not include the detector resolution. 10

1.4 The transverse mass distribution peaks at about the mass of the W boson. This distribution corresponds to Monte Carlo simulated events that do not include the detector resolution. 12

2.1 Schematic view of the Fermilab accelerator complex. 18

2.2 The DØ detector. 20

2.3 The DØ central detector. 22

2.4 The DØ Calorimeter. 25

2.5 Elevation view of the DØ detector. The different regions of the muon system are displayed. 26

2.6 Total interaction lengths of the calorimeter and the muon system as a function of the polar angle θ. 27

2.7 Assembly of a 3–deck muon chamber. 28

2.8 Top: Cross section of a wide angle PDT cell. The lines represent the equi–potential electrostatic field produced by the anode wire and the cathode pads. Bottom: Diamond pattern cathode pad strips of the wide angle PDT cell. 29

2.9 Luminosity delivered and accepted during DØ's run 1A. 35

3.1 The full DØ top view of a $Z \to \mu\mu$ candidate is shown. Each of the muon tracks has hits in the three layers of the muon system, a matching track in the central detectors and points to the reconstructed interaction vertex, that is displaced from the geometrical center of the detector. A small jet has also been reconstructed in the central calorimeter. 44

3.2 The DØ lego plot is shown for an event where a muon and a neutrino (represented by the missing energy $\not{E}_T$) recoil against a jet. All the objects found by the reconstruction program are clearly labeled, their transverse energy can be observed on a vertical scale and their relative position in the $\eta\varphi$ space is also indicated. The η coordinate of the $\not{E}_T$ is not actually measured, so it is displayed arbitrarily at $\eta = 0$. 45

4.1 Transverse mass distribution for a $W \to \mu\nu$ sample and invariant mass distribution for a $Z \to \mu\mu$ sample generated without detector simulator and with the design and actual resolution detector simulation. The $W(Z)$ histograms are normalized to the number of events in the sample with no detector simulation. 53

4.2 Parameterization of the muon momentum resolution as a function of muon momentum. The dots are points obtained from a sample of smeared $W \to \mu\nu$ Monte Carlo events; the full line is the parameterized representation of the muon momentum resolution. . 55

5.1 The energy deposited in the calorimeter in the direction of the muon is plotted for a signal and a background sample for CF and EF muon tracks.The arrows indicate the position of the quality cut. Real muons produced in collider events deposit an energy in the calorimeter that is consistent with the passage of one minimum ionizing particle; tracks that do not originate from the interaction vertex deposit less energy in the calorimeter along the path from the muon chambers to the vertex. 63

5.2 The Muon Global Fit χ^2 is plotted for a signal and a background sample for CF and EF tracks. The arrows indicate the position of the quality cut. 68

5.3 The distributions for $\Delta\varphi$ and $\Delta\theta$ between the muon and the matching CD track are plotted for CF and EF muon tracks. The arrows indicate the position of the quality cut. Tightening the allowed opening angle between the muon and the matching CD track reduces the number of fake track matches. 69

5.4 The muon impact parameters are plotted for CF and EF tracks.The arrows indicate the position of the quality cut. For any prompt muons the impact parameter distributions peak at zero with a finite width produced by multiple scattering and measurement errors; for cosmic rays the primordial impact parameter distributions are flat. 70

5.5 The floating time shift t_0^f is plotted for signal and background samples for CF and EF tracks.The arrows indicate the position of the quality cut. Prompt muons give a t_0^f distribution which peaks at zero since they are produced in coincidence with beam crossing. For cosmics, the time of arrival is random, and the probability is enhanced for cosmics which arrive a bit early. 71

5.6 The two nearest neighbors isolation variable I_μ and the Halo Energy $E(0.6) - E(0.2)$ are plotted for CF and EF tracks. The arrows indicate the position of the quality cut used to define an isolated muon. 72

6.1 The t_0^f distribution for the candidate sample is fitted to a linear sum of the signal and background shape(top). The dotted line corresponds to the clean sample, the dashed line to the cosmic/combinatoric tracks and the solid histogram to their linear sum. The candidate sample shape is given by the data points (bottom). 89

6.2 The $E(0.6) - E(0.2)$ distribution for the candidate sample is fitted to a linear sum of the signal and background shape(top). The dotted line corresponds to isolated tracks, the dashed line to muons originating from QCD processes and the solid histogram to their linear sum. The candidate sample shape is given by the data points (bottom). 92

7.1 Top: The $\mu - \nu$ transverse mass is plotted for the $W \to \mu\nu$ sample in full line and for the combined backgrounds in dotted line. Bottom: the same distribution is shown for the $W \to \mu\nu$ sample after background subtraction and compared to a smeared Monte Carlo. The sample is given by the data points, and the histogram is the Monte Carlo prediction. 99

7.2 Top: The p_T^μ distribution is plotted for the $W \to \mu\nu$ sample in full line and for the combined backgrounds in dotted line. Bottom: the same distribution is shown for the $W \to \mu\nu$ sample after background subtraction and compared to a smeared Monte Carlo. The sample is given by the data points, and the histogram is the Monte Carlo prediction. 100

7.3 Top: The η_μ distribution is plotted for the $W \to \mu\nu$ sample (dots) and for a smeared Monte Carlo that has been run through the trigger simulator (histogram). Bottom: The W p_T distribution is plotted for the $W \to \mu\nu$ sample (dots) and compared to the same distribution for the $W \to e\nu$ sample in dotted line. 101
7.4 Top: The dimuon invariant mass is plotted for the $Z \to \mu\mu$ sample in full line and for the combined backgrounds in dotted line. Bottom: the same distribution is shown for the $Z \to \mu\mu$ sample after background subtraction and compared to a smeared Monte Carlo. The sample is given by the data points, and the histogram is the Monte Carlo prediction. 102
7.5 Comparison of the obtained cross sections with other experimental results [55] and theoretical expectations [54]. The two curves are the extremes obtained with different parton density functions. . . 104
7.6 Comparison of the obtained cross sections ratio with other experimental results [55, 56]. All the 92/93 results, both for DØ and for CDF, are preliminary. 106
7.7 The 95% confidence level limit for , $_W$ is obtained integrating over the complete range of , $_W$ and restricting the calculation to the region that excludes non–physical values for , $_W$. 108
7.8 , $_W$ is plotted as a function of the top quark mass. Based on the limits for , $_W$ obtained in the previous plot, the 95% confidence level lower limit on the top mass is extracted. 109

List of Tables

1.1 Schematic representation of the Standard Model: Constituents are doublets of quarks and leptons in three generations. Forces are mediated by gauge bosons with dimensionless couplings. 5

1.2 Theoretical predictions of the total production cross sections of the intermediate vector bosons at three different perturbation levels. . 14

5.1 Summary of selection cuts used to define a single high p_T isolated muon. 58

5.2 Luminosities for each of the five running periods considered in the analysis. The major changes that occurred at these run boundaries are described in the text. The prescales are not included in the luminosities, for they will be considered as part of the trigger efficiencies; the average factor is included at the bottom of this table for completion only. 74

6.1 Loose muon efficiency for the $W \to \mu\nu$ selection. The first error in the total acceptance calculation is statistical, the second is systematic. 80

6.2 Loose muon efficiencies for the $Z \to \mu\mu$ selection. The first error in the total acceptance calculation is statistical, the second is systematic. 80

6.3 Prescale factors and ratios of efficiencies for "HIGH" and "MAX" filters. 85

6.4 Single muon trigger efficiencies, corresponding to the triggers used in the $W/Z \to \mu$ cross section calculation. The efficiencies correspond to muon tracks that have been reconstructed offline. The preshutdown EF data have been excluded, for the trigger efficiency is not known for that period. 86

6.5 Tight single muon efficiencies. 88

6.6 Background Summary to $W \to \mu\nu$ and $Z \to \mu\mu$ samples. 95

7.1 Number of events in the $W \to \mu\nu$ and $Z \to \mu\mu$ candidate samples for each running period and geographic region. 98

A.1 Muon Identification cut efficiencies derived from data, default Monte Carlo and smeared Monte Carlo. 114
A.2 Muon trigger efficiencies derived from data, default MC, and smeared Monte Carlo, for offline reconstructed tracks. Only statistical errors are shown for the Monte Carlo samples. 115

B.1 Acceptance and Efficiencies affecting the $W/Z \rightarrow \mu$ analysis. . . . 118

Chapter 1

Introduction

"What is the world made of?" "How do the elementary constituents of matter interact with each other?"

The first documented attempt to answer those questions was made 26 centuries ago in ancient Greece by Maximenes of Miletus who proposed that the world is made of air, fire, earth and water, and that all forms of matter can be obtained by rarefying air. This theory turned out to be extremely simple, but also very inaccurate. About 500 years ago, a new age began for modern science when Galileo Galilei introduced the idea of actually verifying the scientific hypotheses by stringent experimental tests.

During the last century physicist have explored nature by studying the basic interactions between fundamental particles. The early experiments in particle physics used radioactive sources to produce energetic particles. An example of this kind of experimental settings is Rutherford's discovery of the atomic nucleus [1].

With the recent technological development, particle accelerators were built to provide for more energetic interactions. The modern accelerators encompass fixed target machines as well as electron–positron and hadron–hadron colliders, which cover a wide range of physical processes. The data obtained from the

numerous experiments operating at those accelerators is used not only to test current theoretical models but also to provide motivation for new ones.

Present–day particle physics research represents man's most organized effort to answer the very same old questions. This thesis hopes to somehow contribute to that effort. Using data collected with the DØ detector at the Fermilab $\overline{p}p$ collider at $\sqrt{s} = 1.8$ TeV during 1992–1993, it presents the experimental determination of the W and Z bosons production cross section in the muon channel. The cross section ratio is furthermore combined with theoretically calculated magnitudes and other experimental determinations to obtain the value of the total width of the W boson.

This thesis is organized as follows: chapter 1 briefly describes the analysis and its theoretical motivation. The Tevatron accelerator at Fermilab and the DØ detector were used to obtain the experimental data this analysis is based on; they are described in chapter 2. Chapter 3 deals with the event reconstruction and chapter 4 with the Monte Carlo simulation of collider data. The muon identification developed for the cross section measurements and the $W \to \mu\nu$ and $Z \to \mu\mu$ event selections are included in chapter 5. The efficiencies for those selections are summarized in chapter 6, together with the estimation of the background contamination that remains in the final data samples. Finally, chapter 7 shows the results of this experimental work, and chapter 8 summarizes the conclusions.

1.1 The Standard Model

Elementary particle physics deals basically with the study of the ultimate constituents of matter and the nature of the interactions between them. It is well known that the everyday life is properly described by Newton's laws of classical

mechanics. But for objects that travel at speeds comparable to the speed of light c, the classical rules need to be modified by special relativity; furthermore, for objects that are very small (roughly at the subatomic level), classical mechanics is supersede by quantum mechanics. As elementary particles are both *fast* and *small*, their description falls under the domain of the quantum field theory.

In the last years a theory has emerged that encompass all known elementary particle interactions except gravity[1]. That theory describes our current knowledge about the dynamics of elementary particles and is know as the Standard Model for matter and energy. Since its introduction in the 1970's, it has passed every experimental test that was performed with ever increasing sophisticated accelerators and detectors.

In the present state of our knowledge, leptons and quarks are considered to be the elementary constituents of matter. Together with the four fundamental interactions (the strong, electromagnetic, weak and gravitational forces) they represent the basic ingredients for a description of the physical world.

The Standard Model describes the interaction between quarks and leptons by means of two mathematical models: Quantum Chromodynamics (QCD) and the Electroweak Theory [2, 3, 4]. QCD, which is based on the $SU(3)$ group, accounts for the strong interaction; the Electroweak Theory, which successfully unifies the electromagnetic and weak interactions, is based on a group structure of $SU(2)_L \times U(1)$.

The fundamental particles considered by the Standard Model are fermions or bosons. The fermions are quarks or leptons with spin $\frac{1}{2}$, that are considered to be the constituents of matter. The bosons have spin 1 and are responsible for

[1]For the interaction between fundamental particles the gravitational force is so weak compared to the other forces that it can be neglected.

mediating the strong and electroweak forces.

The model considers the existence of six electrically charged quarks (Up, Down, Charm, Strange, Top and Bottom) paired in three generations as shown in Table 1.1. The existence of all the quarks except for the Top quark has been experimentally verified. Statistically limited evidence for Top quark production has been recently reported [5]. It is expected that a large amount of data will be recorded at the Fermilab Tevatron during the next couple of years to confirm or deny that report.

Each quark has an additional degree of freedom called color, and labeled Red, Green or Blue. Quarks can only exist in color singlet states and thus can not be isolated. Quarks bound in color singlet states form the hadrons which are found in nature. As the quarks carry electric and color charges, they are subject to both strong and electroweak forces.

The second group of fermions are the leptons, which also appear paired in three families (see table 1.1). The electron, muon and tau are massive particles which carry a negative electric charge $e = 1.6 \times 10^{-19}$ C and thus are subject to electroweak forces. These leptons are paired with three neutrinos, which are light (possibly massless) electrically neutral particles, that only experience weak interactions.

The gauge bosons are responsible for mediating the fundamental forces. The coupling constants describing the strength of these forces are all dimensionless.

The strong force, which acts between particles carrying color, is mediated by eight gluons. Gluons are electrically neutral bosons that carry color charge and therefore undergo self–interactions. The photon γ and the three intermediate vector bosons (IVB) W^+, W^- and Z^0 mediate the electroweak force. The model

Table 1.1: Schematic representation of the Standard Model: Constituents are doublets of quarks and leptons in three generations. Forces are mediated by gauge bosons with dimensionless couplings.

Quarks	Leptons
$u\ d$	$e\ \nu_e$
$c\ s$	$\mu\ \nu_\mu$
$t\ b$	$\tau\ \nu_\tau$

Interaction	Coupling	Gauge Bosons
Strong	g_S	gluons
EM	e	photon
Weak	g_W	$W^+\ W^-\ Z^0$

also predicts the existence of a neutral scalar Higgs boson, which is a remnant of the mechanism that breaks the $SU(2) \times U(1)$ symmetry and generates the W and Z boson masses. So far no experimental evidence exists for the Higgs boson.

1.2 IVB production in hadron colliders

The Electroweak Theory [2, 3, 4] developed by Glasgow, Weinberg and Salam in the 1960's successfully united the electromagnetic and weak interactions, and described a wide range of physical phenomena with great accuracy. In this model the electromagnetic interaction is mediated by the photon γ and the charged weak interaction is mediated by the W bosons. The model also predicted the existence of a neutral boson Z mediator of the neutral weak interaction, unobserved at that time.

The discovery of neutral current interactions by neutrino experiments in 1973 [6] was a great triumph for the electroweak model. Following on this indirect evidence

for the W and Z bosons, high energy hadron–hadron colliders were proposed to search for direct evidence of the IVB [7].

The $Sp\bar{p}S$ at CERN with a center of mass energy $\sqrt{s} = 546$ GeV was the first of these machines. Using 4π detectors and looking for the signal of both leptons in the decay of the W or the Z, the UA1 and UA2 experiments saw direct evidence of W and Z production in 1983 [8]. In subsequent years, with a center of mass energy $\sqrt{s} = 630$ GeV, these collaborations accumulated large data sets of W and Z events identifying them in their decays to electrons, muons, taus and hadrons [9].

In 1985, the Tevatron at Fermilab began operation in the colliding beam mode with a center of mass energy $\sqrt{s} = 1800$ GeV. CDF first saw the W and Z during the 1987 run [10], and accumulated more statistics during the 1988–1989 run. During the 1992–1993 Tevatron run at Fermilab, both CDF and DØ accumulated large amounts of W and Z events based on the 30 pb^{-1} of integrated luminosity delivered by the accelerator.

Proton–antiproton collisions are complicated by the fact that the hadrons are not fundamental particles but are composed of valence quarks, gluons and sea quarks which appear as virtual pairs. The production of the IVB in $\bar{p}p$ collisions can be described using the Drell–Yan process [11], with the quark–antiquark annihilation as the dominant amplitude. If only valence quarks are considered, the elementary processes are:

$$u\bar{d} \rightarrow W^+ \qquad d\bar{u} \rightarrow W^- \qquad u\bar{u}, d\bar{d} \rightarrow Z^0$$

These first order processes are modified by higher order QCD corrections,which are described by additional diagrams as in figure 1.1 (b) and (c) with emission or absorption of gluon radiation. Another effect of gluon radiation is to give the

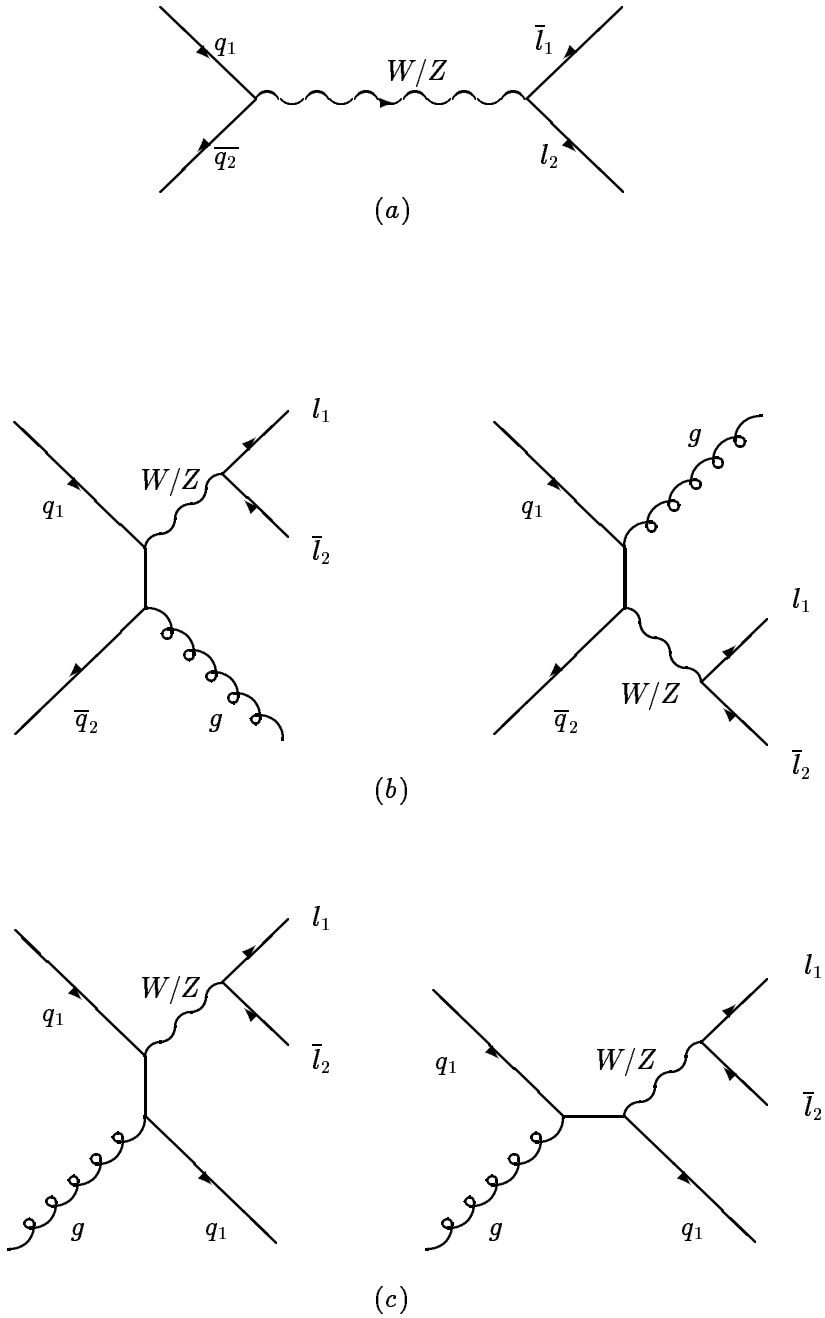

Figure 1.1: Lowest order diagrams for the hadronic production of Intermediate Vector Bosons: (a) The Drell–Yan process, (b) The QCD annihilation process, (c) The QCD Compton process.

produced bosons a transverse momentum much larger than the expected from the lowest order process.

The particles not involved in the production of the IVB are "spectators" that can be involved in low energy interactions called the "underlying event". In $\overline{p}p$ collisions, the momentum of the two involved partons (quarks or gluons) is not known in the longitudinal direction along the beam pipe, but is considered to be zero in the perpendicular plane. In addition, small angle products of the collision can be lost by entering the beam pipe and thus escaping detection; therefore the collisions are described using quantities that are defined transverse to the beam, which are the ones that are conserved in these kind of processes.

The experimental signature of the production of charged or neutral gauge bosons is easiest to identify by their leptonic decays:

$$W^{\pm} \rightarrow l^{\pm}\nu_l \qquad Z^0 \rightarrow l^+l^-$$

Although the decay into q and $\bar{q}$ has the largest branching ratio ($\approx$ 70%) it also has the largest contamination arising from strong interaction processes, which are dominated by dijet events. In spite of the small branching ratio of the leptonic decays ($\approx$ 10%(3%) for each leptonic[2] channel for $W(Z)$ bosons [12]), these modes suffer from the lowest QCD contamination and therefore provide the cleanest sample of W and Z events obtainable in hadron colliders.

The Z decay into a pair of high p_T charged leptons can be directly identified through a peak in the dilepton invariant mass, as can be seen in figure 1.2. In this case backgrounds from continuum Drell–Yan pairs and heavy quark decays are essentially negligible.

[2]The branching ratio for the $Z \rightarrow \nu\bar{\nu}$ channel is $\approx$ 20%, the 3% cited above refers to the e^+e^-, $\mu^+\mu^-$ and $\tau^+\tau^-$ decay modes.

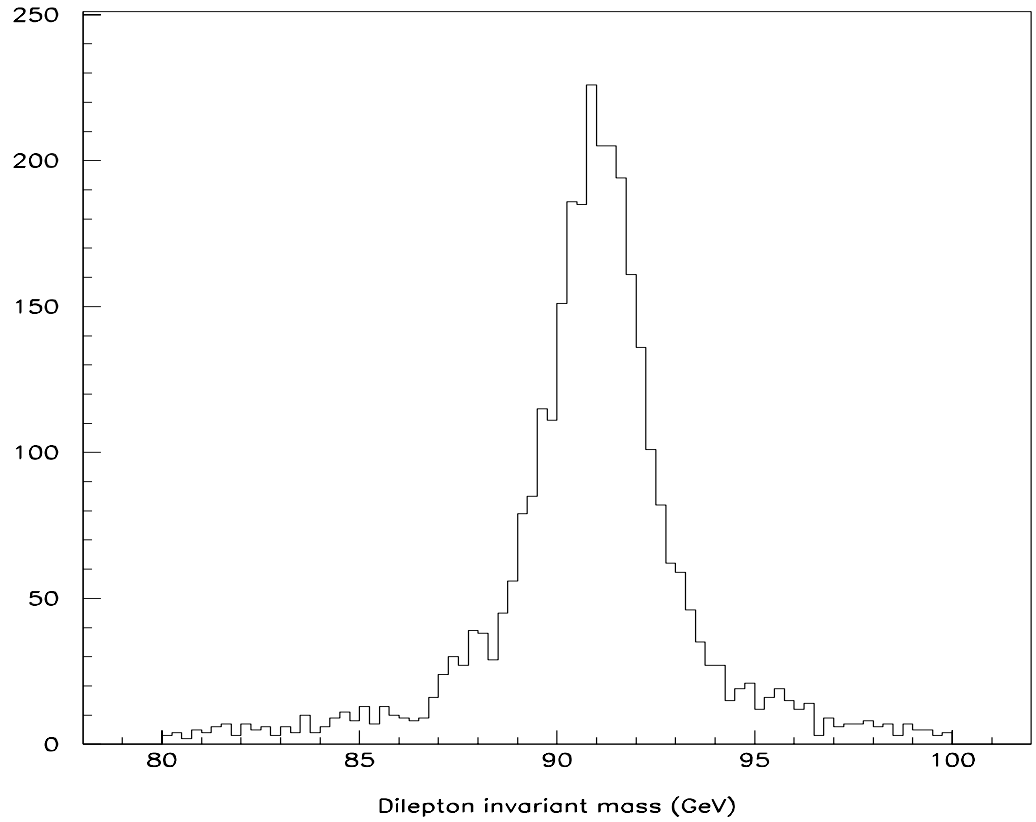

Figure 1.2: The Z decay into a pair of charged leptons can be directly identified through a peak in the dilepton invariant mass distribution. This distribution corresponds to Monte Carlo simulated events that do not include the detector resolution.

The situation is less favourable for the leptonic decay modes of the charged weak boson W. Although the detection of one high p_T charged lepton is relatively straightforward, the observation of the accompanying neutrino has to be made based on kinematic arguments. A momentum imbalance in the transverse plane is a signal for the presence of one or more noninteracting particles, presumably neutrinos.

The charged lepton and the neutrino from a W decay are very energetic due

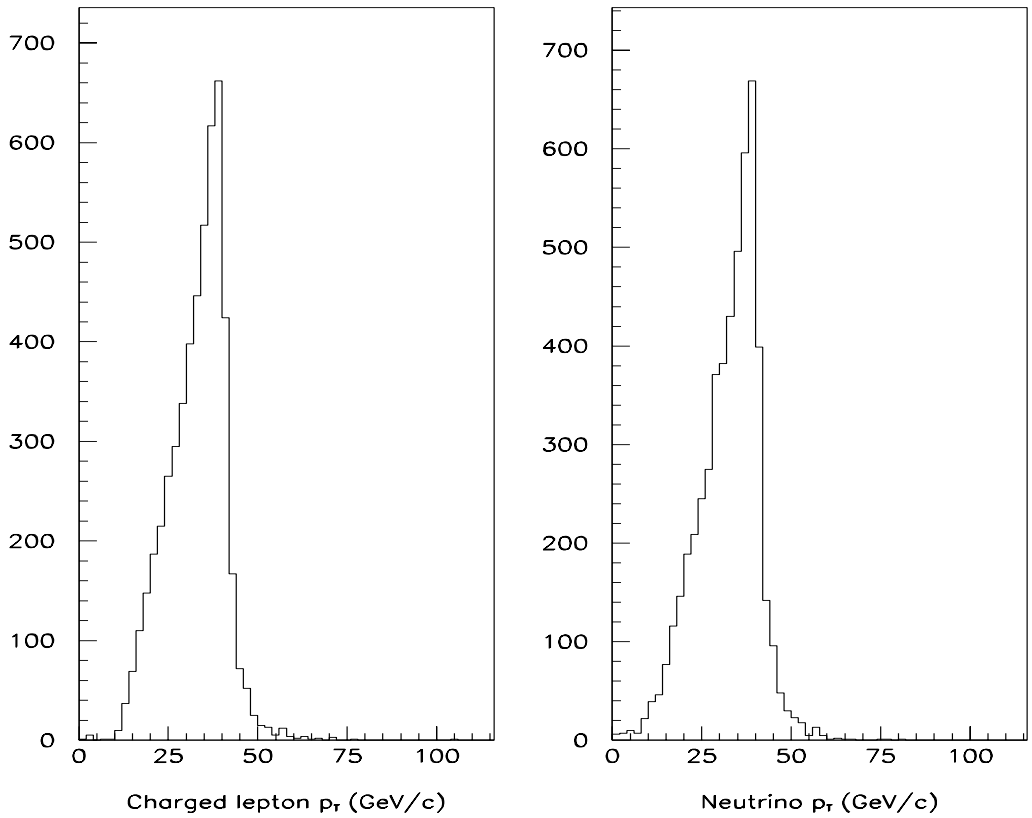

Figure 1.3: The transverse momentum spectrum of the decay products from a W decay peaks at about half the value of the W mass for the charged lepton (left) and for the neutrino (right). This distributions correspond to Monte Carlo simulated events that do not include the detector resolution.

to the large mass of the W boson from which they originate. Since the considered process is a two body decay of a heavy object into two light products, a peak exists in the transverse momentum spectrum of the decay products, at about half the value of the W mass as shown in figure 1.3.

The transverse mass of the W is defined as

$$M_T(l\nu_l) = \sqrt{2p_T(l)p_T(\nu_l)\{1 - cos\,[\varphi(l) - \varphi(\nu_l)]\}}$$

with φ the azimuth angle in the transverse plane to the beam pipe. The quantity $M_T(l\nu_l)$ has the property that

$$0 \leq M_T(l\nu_l) \leq M_W$$

where the equality holds for events with no longitudinal momentum components and the distribution peaks at about the mass of the W boson as can be seen in figure 1.4. The right end of the spectrum is smeared by the finite width of the W and by the W transverse momentum, arising from the intrinsic p_T of the constituents and from QCD corrections.

There are numerous tests of the Standard Model that can be performed by hadron collider experiments. Since the first direct observation of the IVBs, together with the measurement of their mass and width, many essential predictions of the model about the properties of the bosons have been experimentally verified. Some extra information can be obtained by combining the findings on the W and Z, to provide more precise tests of the model. One possible analysis of this kind is presented in the next section.

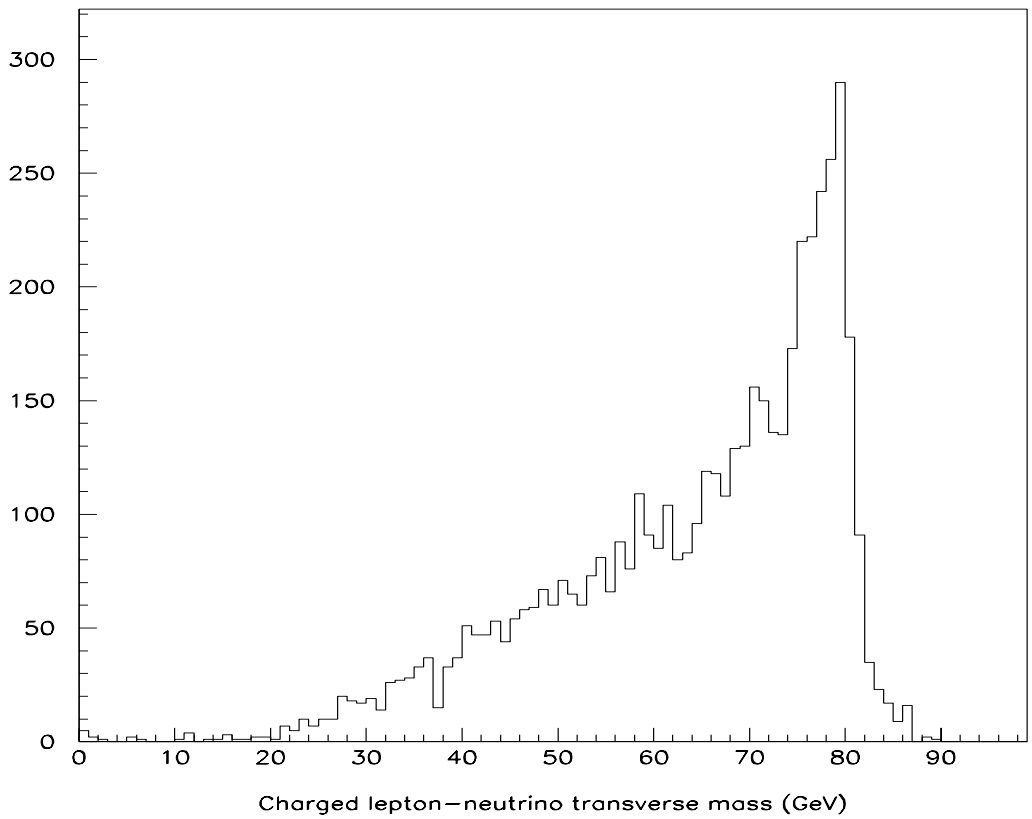

Figure 1.4: The transverse mass distribution peaks at about the mass of the W boson. This distribution corresponds to Monte Carlo simulated events that do not include the detector resolution.

1.3 Description of the Analysis

Hadron collider experiments do not measure $,_W$ and $,_Z$ very precisely, but they can determine the ratio $,_W/,_Z$ indirectly by measuring

$$R \equiv \frac{\sigma(\overline{p}p \to W + X)BR(W \to l\nu)}{\sigma(\overline{p}p \to Z + X)BR(Z \to l^+l^-)} = \frac{\sigma_W^l}{\sigma_Z^l} \tag{1.1}$$

defined as the ratio of the W and Z production cross sections times the branching ratio for leptonic decays. This ratio can be expressed in terms of fundamental quantities as follows:

$$R = \frac{\sigma_W}{\sigma_Z} \quad \frac{,(W \to l\nu)}{,(Z \to l^+l^-)} \quad \frac{,_Z}{,_W} \tag{1.2}$$

where $\sigma_W \equiv \sigma(\overline{p}p \to W + X)$ and $\sigma_Z \equiv \sigma(\overline{p}p \to Z + X)$ are the total cross sections for W and Z production, and the , 's are the total and partial widths for boson decays.

The first two ratios on the right hand side of equation 1.2 can be computed based on some limited assumptions about the standard gauge couplings of leptons and light quarks. R itself can be measured by hadron collider experiments, which enables the calculation of $,_Z/,_W$.

The calculation of the inclusive production cross sections for the W and Z bosons can be obtained as a convolution integral over the parton distribution functions. Reference [13] uses the theoretical predictions by Hamberg, Van Neerven and Matsuura [14] which are complete up to the $O(\alpha_S^2)$ order for the corrections to the Drell–Yan K–factor for the boson production. Table 1.2 lists the values for the total cross sections for the W and Z production at $\sqrt{s} = 1.8$ TeV and

of their ratio for each of the three perturbation orders as obtained in [13]. The biggest uncertainty in the calculation of the total cross sections arises from the parton distribution functions; in particular, the uncertainty in the calculation of the cross section ratio σ_W/σ_Z is dominated by the uncertainty on the ratio of the d and u valence quark densities [13], since the W and Z bosons couple differently to the two types of quarks.

Table 1.2: Theoretical predictions of the total production cross sections of the intermediate vector bosons at three different perturbation levels.

Order	σ_W (nb)	σ_Z (nb)	σ_W/σ_Z
Born Level	16.19	4.91	3.30
$O(\alpha_s)$	18.97	5.79	3.27
$O(\alpha_s^2)$	19.15	5.88	3.26

The ratio of the partial widths , $(W \to l\nu)/$, $(Z \to l^+l^-)$ into charged leptons can be evaluated using the Standard Model couplings

$$, (W \to l\nu) = \frac{G_F m_W^3}{6\pi\sqrt{2}} \tag{1.3}$$

$$, (Z \to l^+l^-) = (1 - 4\sin^2\theta_W + 8\sin^2\theta_W)\frac{G_F m_Z^3}{12\pi\sqrt{2}} \tag{1.4}$$

Combining equations 1.3 and 1.4, gives

$$\frac{, (W \to l\nu)}{, (Z \to l^+l^-)} = \frac{2m_W^3/m_Z^3}{1 - 4\sin^2\theta_W + 8\sin^2\theta_W} \tag{1.5}$$

By using the Sirlin renormalization scheme, which chooses m_W, m_Z and G_F as the fundamental parameters and fixes

$$\sin^2\theta_W \equiv 1 - \frac{m_W^2}{m_Z^2} \tag{1.6}$$

to all orders in perturbation theory, it is possible to calculate the ratio of the partial widths from the most accurate values for m_W/m_Z available at present.

The experimental determination of the σ_W^l and σ_Z^l cross sections can be computed according to the formulas

$$\sigma_W^l = \frac{N_W - N_B}{\varepsilon_W A_W L_W} \tag{1.7}$$

$$\sigma_Z^l = \frac{N_Z - N_B}{\varepsilon_Z A_Z L_Z} \tag{1.8}$$

where N_W (N_Z) is the number of W (Z) candidates observed, N_B is the estimated number of background events to the sample, ε is the total efficiency for detecting the signal events inside the geometrical acceptance (A) of the detector and L is the integrated luminosity corresponding to the considered samples. The uncertainty on the geometrical acceptance is dominated by the choice of structure functions for they can alter the rapidity distribution of the IVB. The systematic errors in the computation of $R = \sigma_W^l/\sigma_Z^l$ are smaller than those on the individual cross sections, because many common sources of error cancel, including all of the error on the luminosity and part of the errors on the acceptance and selection efficiency.

The precise determination of the total widths of the W and Z bosons is an interesting test of the Standard Model because they are inclusive measurements that are sensitive to unobserved decay modes of the IVB, regardless of whether or not they can be detected. The total width of the Z has been measured to very

high precision ($< 1\%$) at LEP [15], placing severe constraints on the existence of new particles produced in neutral weak decays.

The total width of the W is known with an order of magnitude less precision than for the Z. Therefore, the corresponding limits on charged weak decays are much less stringent. In particular, the existence of a light top quark with unconventional decay modes is not ruled out if $m_t < m_W - m_b$. Although precision electroweak data suggest that the top quark is much heavier than m_W, these predictions are made within the framework of the three-generation minimal standard model. Extensions of the standard model can allow a wider range of top quark masses to be compatible with both the LEP data and with the constraints from direct top quark searches. It is therefore of interest to determine Γ_W itself with improved precision in order to rule out unexpected W decay modes. Given the precise measurement of Γ_Z, the calculation of R in hadron colliders gives the best determination of Γ_W obtainable at this time.

Chapter 2

Experimental Description

2.1 The Tevatron at Fermilab

The accelerator complex at the Fermi National Accelerator Laboratory (Fermilab) [16] consists of several accelerator and storage systems used to produce collisions between protons and antiprotons, with a center of mass energy $\sqrt{s} =$ 1.8 TeV. Figure 2.1 shows a schematic view of the Fermilab accelerator.

The process starts with a Cockcroft–Walton generator that produces a beam of H^- ions at an energy of 750 KeV, which is then injected into a linear accelerator. There the ions are accelerated to approximately 400 MeV, and injected into a circular booster ring. In the booster, the H^- ions are stripped of their electrons and the protons are further accelerated to an energy of 8 GeV. The protons are then injected into a 6.28 km proton synchroton, called the Main Ring. The Main Ring performs two tasks: it accelerates the protons to an energy of 150 GeV before injecting them into the Tevatron, and it serves as a source of 120 GeV protons for antiproton production. The Tevatron shares the same 2 km diameter tunnel as the Main Ring, but accelerates the particles up to an energy of 900 GeV, using superconducting magnets.

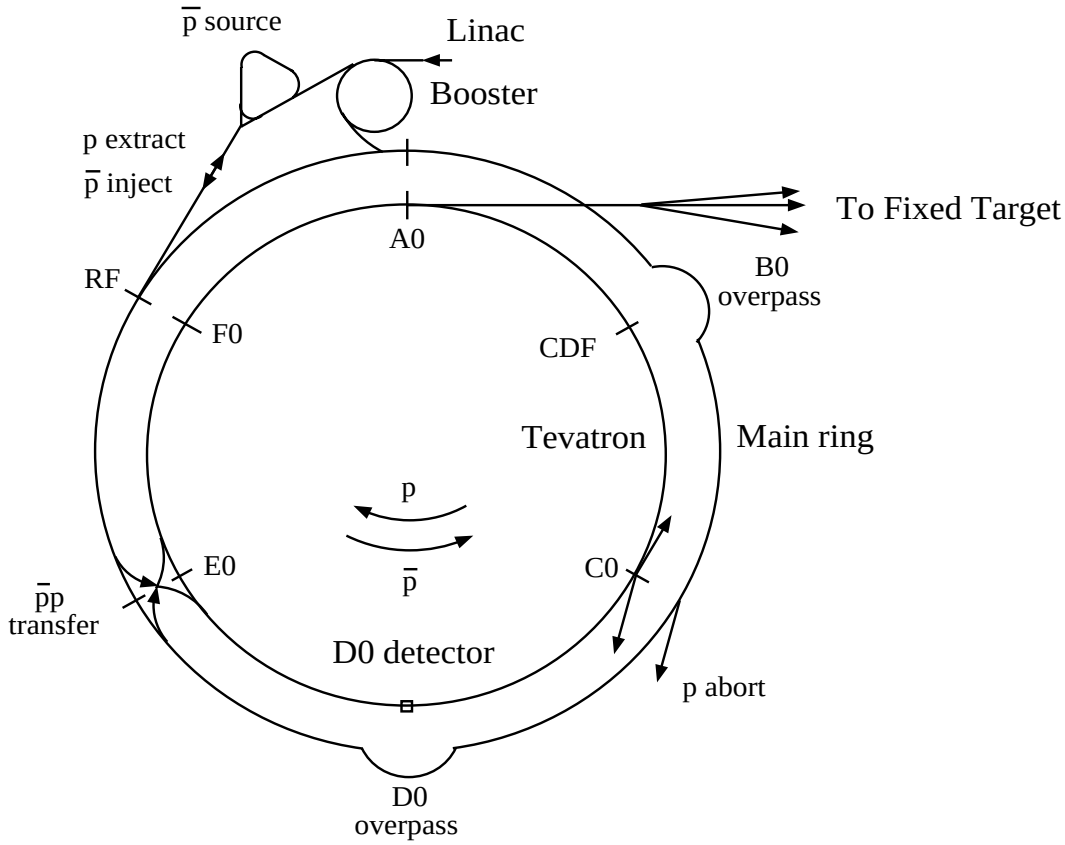

Figure 2.1: Schematic view of the Fermilab accelerator complex.

The superconducting Tevatron is located 65 cm directly below the Main Ring beam except in the regions of the two collider detectors were significant vertical separation of the two beams is achieved to avoid having them both pass through the most sensitive parts of the collider detectors.

Antiprotons are produced when 120 GeV protons from the Main Ring hit a nickel target that is followed by a lithium lens to focus negative secondaries. The secondary beam energy spread needs to be reduced before it can be stochastically cooled in the accumulator. The cooling of the antiprotons starts in the Debuncher, where the beam remains for two seconds during which time the spread in energy ($\approx 2\%$) is reduced while the bunch length is increased before being directed into

the Accumulator. There the antiprotons are stochastically cooled and stored. A new antiproton pulse from the Debuncher is transferred to the Accumulator every two seconds. After several hours of collecting antiprotons in the Accumulator, the stack reaches 50 to 100 mA which is sufficient to inject six bunches that are each about 30×10^9 antiprotons per bunch into the Main Ring to be accelerated to an energy of 150 GeV. After the antiprotons reach 150 GeV in the Main Ring they are transferred into the Tevatron were six bunches of protons are already circulating.

Since protons and antiprotons have opposite charges, they circulate in opposite directions inside the Tevatron. Simultaneously the beams of protons and antiprotons are accelerated to an energy of 900 GeV, and the six bunches of protons pass the six bunches of antiprotons at twelve interaction points around the accelerator ring. At ten of these points the beams are separated by electro–static devices to avoid the collisions. At two of the straight sections in the Tevatron lattice the nominal beta function that characterizes the beam envelope is reduced in the transverse dimension to produce a 30 μm spot size where the beams collide. One of these low beta interaction points is located within 10 cm of the center of the DØ detector.

2.2 The DØ detector

The DØ detector [17] is a large multi–purpose detector operating with the Fermilab proton–antiproton collider. It has been designed to precisely measure electrons, muons, jets and missing energy. The detector consists of three major components: the central detector, the uranium–liquid argon calorimeters and the muon system. In the following sections, each of these subdetectors will be briefly described, as

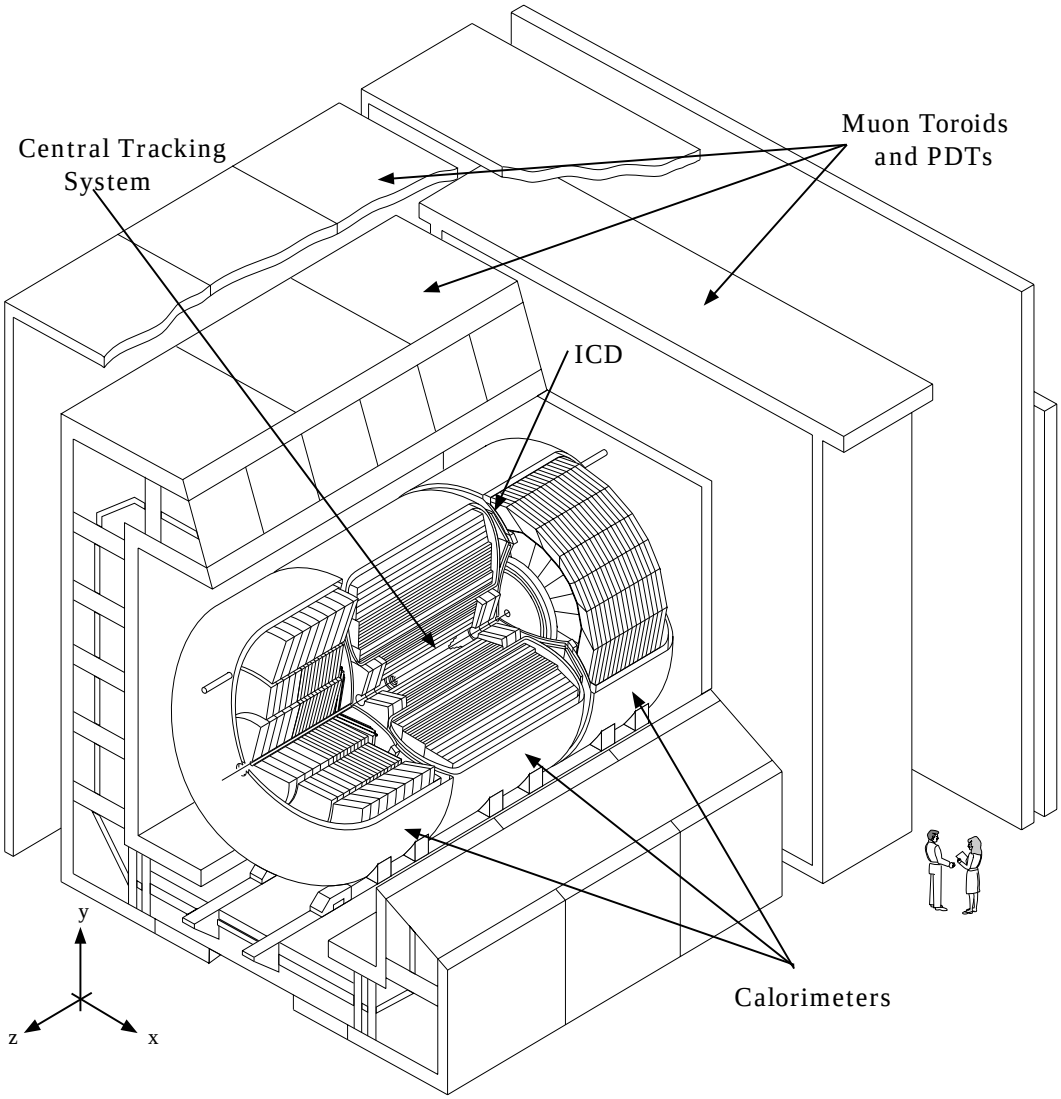

Figure 2.2: The DØ detector.

will the triggering and data acquisition system.

Figure 2.2 shows a view of the full detector, including the Tevatron beam pipe centered within the detector and the lower energy Main Ring beam pipe which passes 2 m above the detector center, through the calorimeter and the muon system. The DØ coordinate system is defined with the z axis parallel to the beam pipe in the direction of the protons, while the y axis points up.

2.2.1 The DØ central detector

The DØ central tracking detector is composed of four different systems: the Vertex Drift Chamber (VTX), the Transition Radiation Detector (TRD), the Central Drift Chamber (CDC) and two Forward Drift Chambers (FDC). The VTX, TRD and CDC are arranged in three cylinders concentric with the beam pipe, while the two FDC detectors are orientated perpendicular to that direction, as shown in figure 2.3. The full Central Detector fits within the inner cylindrical aperture of the calorimeters, in a volume of 78 cm in radius and 270 cm in length. As the DØ detector does not have a central magnetic field, the tracking system was designed and optimized to achieve high efficiency, resolve overlapping tracks by measurement of dE/dx and accurately locate the vertex in transverse and longitudinal space.

The Vertex Chamber is the innermost tracking detector in DØ . Its inner (outer) radius of 3.7 cm (16.2 cm) is concentric with the beam pipe, and it has a maximum length of 116.8 cm.

As is typical for a drift chamber the $r\varphi$ measurement relies on information from anode wires which run parallel to the beam direction and are surrounded by a cathode. In order to resolve the left–right ambiguities (i. e. to determine on

Figure 2.3: The DØ central detector.

which side of the wire plane the particle passed), the sense wires are staggered, breaking the symmetry and allowing for the determination of the correct side. The DØ vertex chamber has three concentric layers of cells with eight staggered sense wires in each cell to provide a measurement of the $r\varphi$ coordinate with a typical resolution of 50 to 100 μm and a pulse pair separation of about 2 mm in $r\varphi$.

The z coordinate is determined by a method known as charge division. Since the sense wires are resistive, the charge signals from both ends can be used to determine the location of a hit, achieving a resolution of $\approx$ 2 mm in the z coordinate.

The Transition Radiation Detector occupies the space between the VTX and the CDC, and is meant to provide independent electron identification in

addition to that given by the calorimeters. When a charged particle passes through an interface between two types of material with different dielectric constants, the requirement that the fields of the particle satisfy the boundary conditions at the transition point requires a radiative component of the field. Although the effect is weak, if a large number of interfaces are put together in a short distance, the produced radiation can be observed. As the amount of radiation depends on the mass of the objects, it can be used to discriminate between different particles.

Based on this principle, the DØ TRD provides a factor of about 50 for rejection of isolated pions and is used as an additional confirmation for the calorimeter electron identification.

The Central Drift Chamber has a cylindrical shape with a length of 184 cm, inner radius of 49.5 cm and outer radius of 74.5 cm. It is located between the TRD and the Central Calorimeter. As for the VTX chamber, the CDC $r\varphi$ measurement in based on information provided by staggered anode wires.

The CDC consists of four concentric rings of 32 cells per ring; each cell contains seven staggered wires that are parallel to the z axis and successively displaced in radius. To further improve the pattern recognition and minimize dead regions, alternating radial cells are offset in φ by one half cell. The measured resolution as obtained from the residuals of hits for fully reconstructed tracks is about $150 - 200$ μm in $r\varphi$. The pulse pair separation in the $r\varphi$ drift direction is about 2 mm.

The z coordinate is measured using delay lines that lie parallel to the outer sense wires in each cell. When an avalanche occurs on an outer sense wire, pulses are induced on the delay line and the difference in arrival times at the two ends allows for a determination of the z coordinate with a resolution of ≈ 2 mm.

The Forward Drift Chambers are located at either end of the VTX, TRD

and CDC, and before the End Calorimeters, extending the coverage for charged particle tracking down to $\theta \approx 5$ degrees. They consist of three separate chambers: a Φ module whose sense wires are radial for measurement of the φ coordinate, and two Θ modules (one at each side of the Φ module), which provide a measure of the θ coordinate. Each Θ cell is equipped with one delay line to provide a coarse measurement of the θ coordinate with a resolution of ≈ 4 mm. The resolution in the drift direction, measured as in the CDC, is found to be between $150 - 200$ μm in $r\varphi$ ($r\theta$) for Φ (Θ) chambers. The pulse pair separation in the drift direction is ≈ 2 mm.

2.2.2 The DØ calorimeter

The DØ uranium–liquid argon sampling calorimeters are used to identify electrons, photons, jets and muons and to provide the energy measurements for electrons, photons and jets. Further, by using the ganged nature of the pads that form towers, they are used in the calculation of transverse energy and in triggering. Figure 2.4 shows a schematic view of the DØ calorimeters, which surround the Central Detector. The Central Calorimeter provides coverage out to a value of pseudorapidity[1] of $|\eta| \leq 1$, and the two End Calorimeters extend the coverage out to $|\eta| \leq 4$. Two scintillation counter arrays called intercryostat detectors (ICD) are used to correct for energy deposited in the walls of the cryostats between the Central and the two End Calorimeters. Both the Central and the End Calorimeters have three different types of modules: an electromagnetic section made of thin (3 or 4 mm) uranium absorber plates, a fine hadronic section with thicker (6 mm) uranium plates, and a coarse hadronic section with thick (46.5 mm) cop-

[1]The pseudorapidity η is defined as $\eta = -ln(tg\frac{\theta}{2})$, with θ being the polar angle.

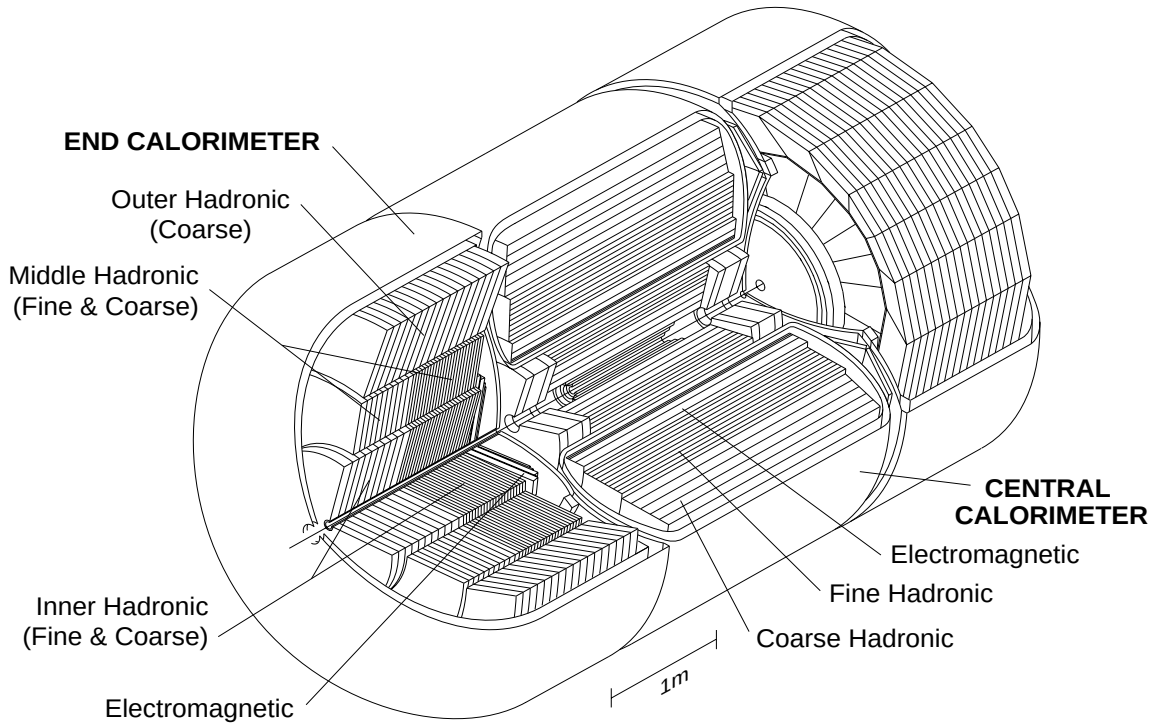

Figure 2.4: The DØ Calorimeter.

per or stainless steel plates. The resolutions are $\approx 15\%/\sqrt{E(\mathrm{GeV})}$ for electrons and photons and $\approx 50\%/\sqrt{E(\mathrm{GeV})}$ for hadrons.

2.2.3 The DØ muon detection system

The muon system is DØ's outermost detector, which surrounds the calorimeters both in the central and in the end regions. Its purpose is to identify muons produced in $p\overline{p}$ collisions and to determine their trajectories and momenta. Its outside dimensions are 11.6 m wide, 12.9 m high and 19.7 m long in the direction of the beam. It consists of five magnetized iron toroids and a set of proportional drift tube (PDT) chambers that provide coverage down to within $\theta \approx 3$ degrees of the beams.

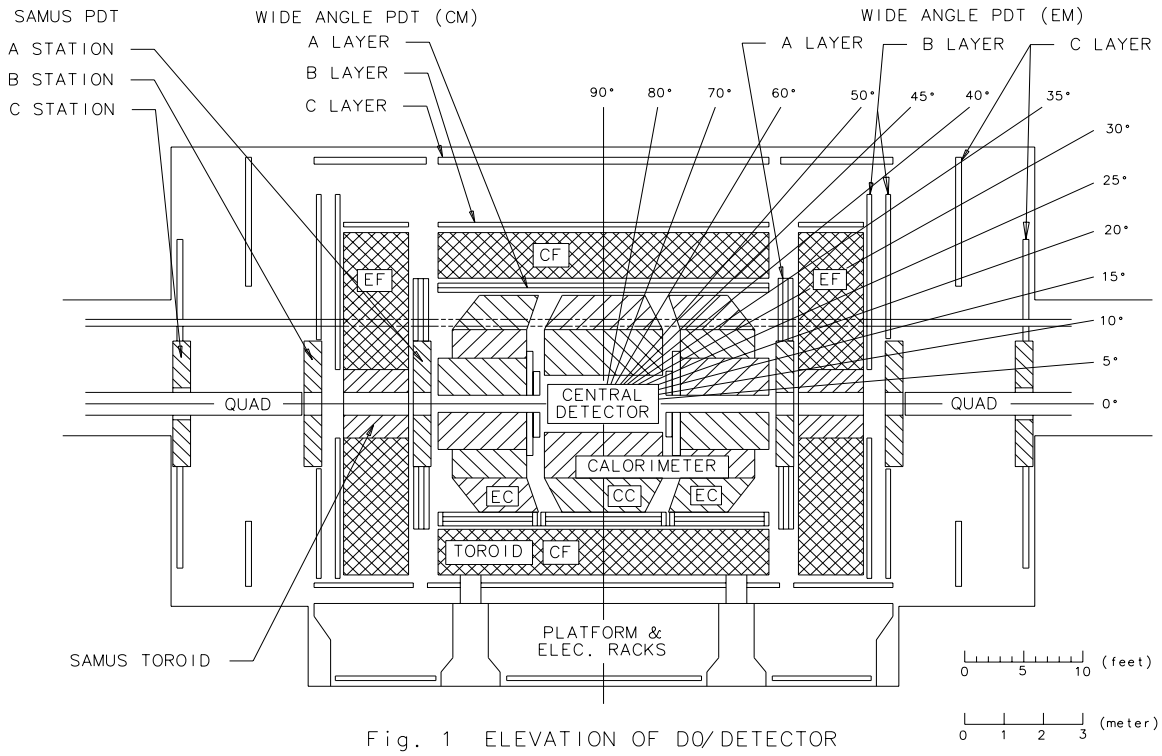

Figure 2.5: Elevation view of the DØ detector. The different regions of the muon system are displayed.

Figure 2.5 shows the elevation view of the DØ detector and indicates the position of the five toroids and their associated PDT layers. The central toroid (CF) has a width of $\approx$ 110 cm and covers the region of $|\eta| \leq 1$; the two end toroids (EF) are somewhat broader ($\approx$ 150 cm) and extend the coverage to $1 < |\eta| \leq 2.5$. These detectors are labeled the Wide Angle Muon System (WAMUS). In addition, two Small Angle Muon System (SAMUS) toroids ($\approx$ 150 cm wide), that fit into the central hole of the EF toroids, extend the $|\eta|$ coverage from 2.5 to 3.3. The large interaction lengths provided by the calorimeters assures that most of the hadrons and electrons are filtered out before reaching the muon system which ensures a clean environment for identification and momentum measurement of high p_T muons. Figure 2.6 shows the total interaction length of the calorimeter

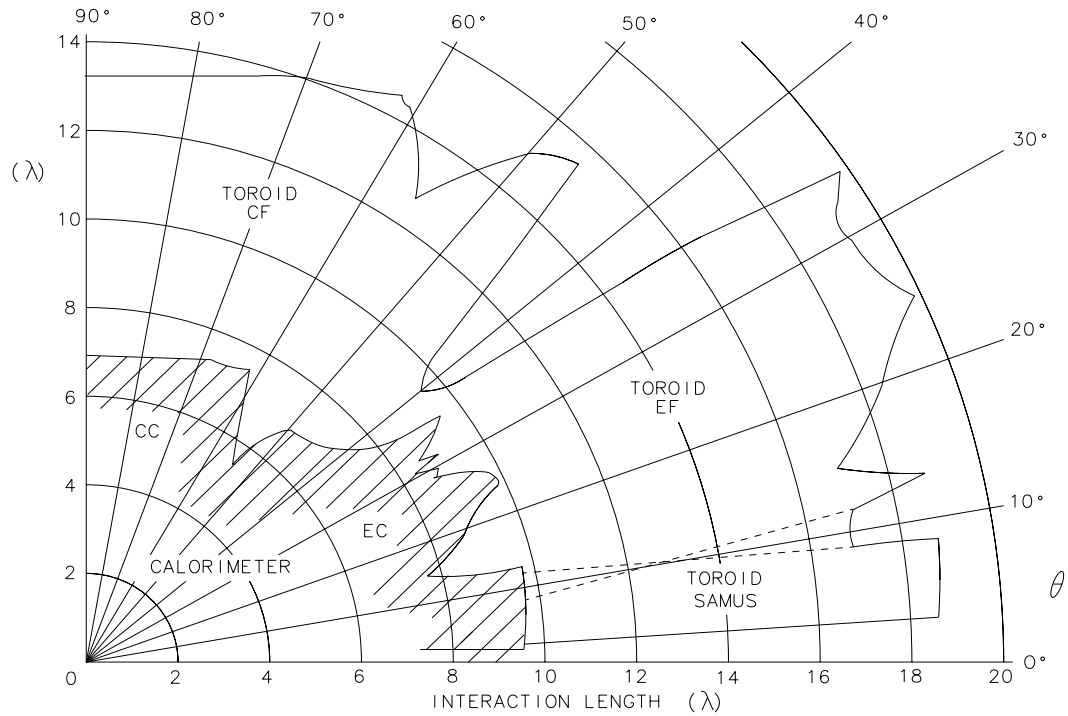

Figure 2.6: Total interaction lengths of the calorimeter and the muon system as a function of the polar angle θ.

and the muon system as a function of the polar angle θ.

The 1.9 Tesla magnetic field inside the toroids ($\vec{B} \sim B_o\hat{\varphi}$) bends the muons in the rz plane. A set of determinations of the muon track both before and after the bend provide a measurement of the bending angle in the toroid and hence the momentum of the particle. As the wide angle muon system is crucial for the analysis that is being presented, it will be described in somewhat more detail than the other DØ subdetectors.

The Wide Angle Muon System consists of a central toroid (CF), two end toroids (EF), and 164 proportional drift tube chambers separated in three layers: the A layer is located between the calorimeter and the toroids; the B and C layers are located outside the toroids and separated about 1 meter from each other. Figure 2.7 shows a transverse view of the WAMUS PDT cells, as

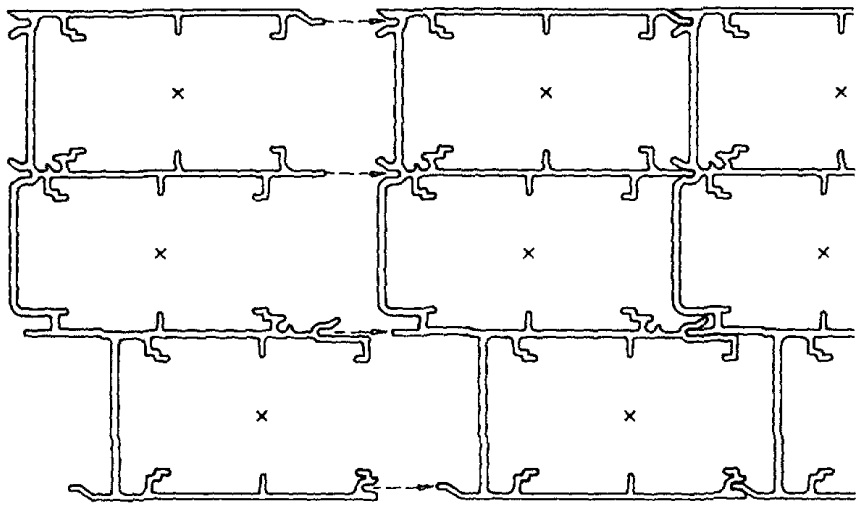

Figure 2.7: Assembly of a 3–deck muon chamber.

well as the relative offset between different planes that allows for resolving the left–right drift ambiguity. Each unit cell has an anode wire at its center and a repeating diamond pattern cathode pad strip at its top and bottom as can be seen in figure 2.8. The anode wires are oriented along the toroid's magnetic field to give accurate measurement of the bend coordinate by achieving a resolution in the drift coordinate of $400 - 900\ \mu$m.

Wires from adjacent cells in the drift direction are jumpered together at one end, providing a coarse determination of the coordinate along the wire (ξ) by measuring the time difference Δt for a particular anode signal to arrive at the two ends of the paired wire. The Δt measurement determines ξ with a precision of

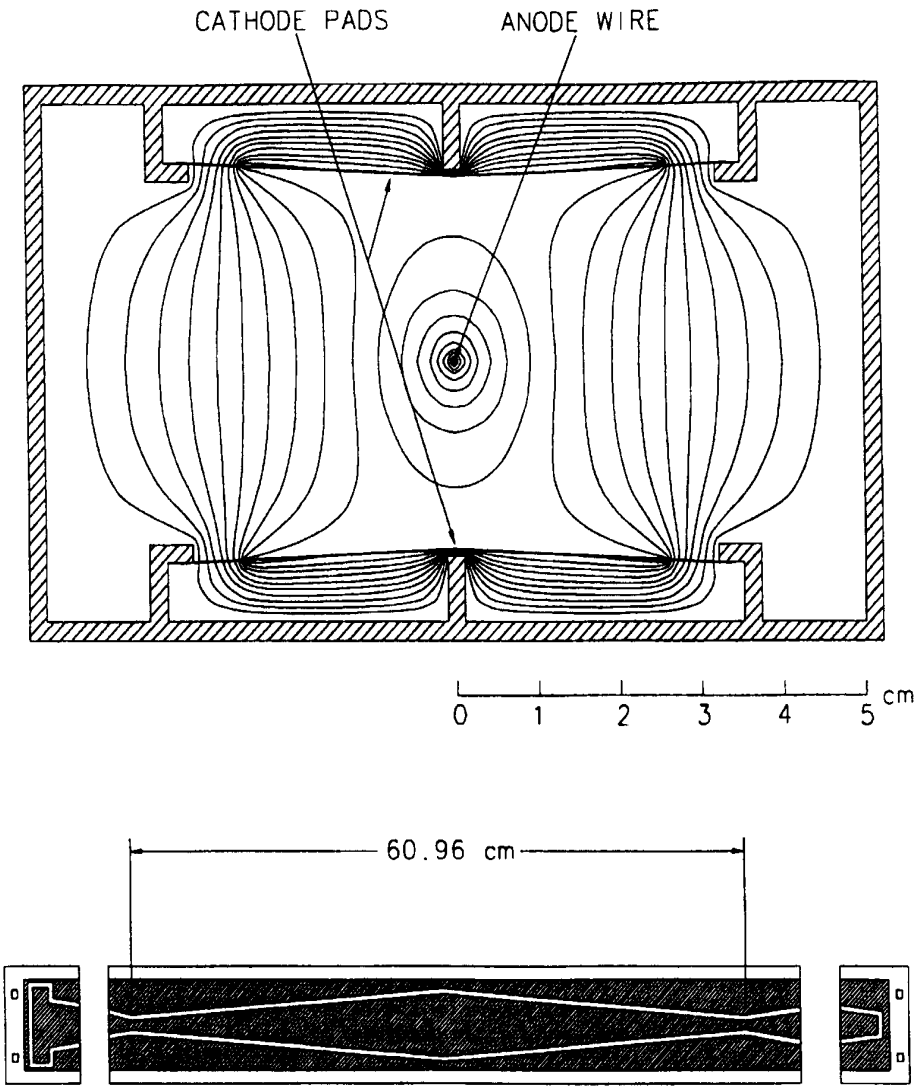

Figure 2.8: Top: Cross section of a wide angle PDT cell. The lines represent the equi–potential electrostatic field produced by the anode wire and the cathode pads. Bottom: Diamond pattern cathode pad strips of the wide angle PDT cell.

about 10 to 20 cm along the wire, which allows a determination of correct cathode pad period. The fine determination of ξ is obtained using the information from the relative charges accumulated in the inner and outer cathode pads. Thus a resolution of ≈ 1 cm is obtained for the ξ coordinate.

During operation the cathode pads are held at +2.3 kV and the anode wire at +4.56 kV. The gas mixture of Ar(90%), CF_4(5%) and CO_2(5%) provides a drift velocity of about 6.5 cm/μs; the maximum drift distance is 5 cm.

There are four PDT planes in the A layer chambers and three PDT planes in the B and C layer chambers. The trajectory of the incident muon is determined using information provided by the muon system A layer, the matching track seen by the central tracking and the reconstructed interaction point. The trajectory of the muon after the toroids gets reconstructed based on information provided by the muon B and C layers. Comparing the directions of the incident and emerging muon provides a measurement of the bending angle, and hence a determination of the momentum of the detected particle. Multiple scattering in the iron toroids limits the momentum resolution to $\approx 20\%$ at low momenta. At higher momenta the limit is imposed by the bend coordinate resolution in the PDT's. The momentum resolution of the WAMUS system is described in more detail in section 4.4.

The Small Angle Muon System consists of two sets of three stations: the A station located in the inner surface of the SAMUS toroids, and the B and C stations located outside the toroids. Each station consists of three doublets of cylindrical 2.5 cm diameter proportional drift tube chambers, oriented in the x, y and u directions, where u is rotated 45° with respect to x and y. As for the WAMUS, the determination of the muon momentum is obtained from the bending of tracks in the SAMUS toroids.

2.2.4 Trigger and Data Acquisition

The DØ trigger and data acquisition systems are the key to selecting and recording interesting events. As the operation of the Tevatron with six bunches of protons and antiprotons gives a time of 3.5μs between crossings, several levels of increasingly sophisticated event characterization are needed in the trigger to minimize the dead time.

Three levels of trigger exist in DØ : The **Level 0** scintillator based trigger, that indicates the occurrence of an inelastic collision, serves at the same time as the luminosity monitor of the experiment[2]. The **Level 1** hardware trigger, that operates in the time between crossings, and which introduces no deadtime, is complemented with the **Level 1.5** trigger, that requires several bunch crossings to complete the event characterization. The rate of events passing Level 0 for a luminosity of 5×10^{30} cm^{-2} s^{-1} is about 150 kHz, while the rate out of Level 1 is about 200 Hz. This rate is further reduced to less than 100 Hz after Level 1.5.

Events that are considered interesting candidates by the hardware triggers are passed on by the DØ data acquisition system to a farm of microprocessors. These processors make a first pass reconstruction of the events in a time budget of 250 ms to perform the last trigger decision. This process is referred to as the software **Level 2** trigger. The rate of events passing all the levels of trigger requirements is about 2 Hz. Digitized event data are then sent to a host computer both for monitoring and recording on 8 mm magnetic tapes.

High p_T single muon triggers contained entirely within the WAMUS detector are essential for the analysis that is being presented here and will thus be described in further detail. The basic information provided by the wide angle muon cham-

[2]The next section describes this process in more detail.

bers to the hardware muon trigger system is a single pad latch bit for each drift cell of the muon system that is hit during a collision. A pad latch bit is defined as a cathode pad signal that sets a bit to *true* if its associated cell has been fired. This determines the bend coordinate of hit cells with a granularity of 10 cm. This information is then delivered to a digital logic circuit that combines pad latch bits corresponding to different planes within each layer of the muon system to generate bit patterns corresponding to hit centroids. A centroid is defined as the most likely half cell traversed by a track projected to the midplane of a chamber. A valid centroid requires hits in at least two of the planes within a layer. The Level 1 trigger then compares combinations of B and C centroids with A layer centroids to determine if they correspond to possible tracks in a 60 cm wide road, giving an effective p_T threshold cut of 5 GeV. A successful Level 1 decision allows for a Level 1.5 confirmation, which is done by comparing all combinations of A, B and C layer centroids to determine if they correspond to tracks within a finer road, giving an effective p_T cut of 7 GeV. The Level 1 decisions are available within the 3.5μs bunch crossing time, while the Level 1.5 typically takes less than 10μs.

An event with a successful level 1.5 determination moves on to the software Level 2 triggers, which perform a first pass muon reconstruction[3] using the information provided by the muon system and the interaction vertex provided by the Level 0 system. To speed up the Level 2 trigger decision, the software only looks for a muon track in the same trigger sector were a Level 1 candidate was reported. The trigger sectors are geometrically defined by the toroid the muon track passes through as CF, EFN and EFS for the central and both north and south ends respectively. If a reconstructed muon is found with a p_T above a certain thresh-

[3]Next chapter describes the offline muon reconstruction in detail.

old that satisfies certain quality criteria, the event is recorded. A more detailed description of the Level 2 muon quality cuts used by the $W/Z \rightarrow \mu$ triggers can be found in section 6.1.2. The p_T threshold for these triggers is set to 15 GeV.

2.3 Luminosity Monitoring at DØ

The monitoring of the luminosity delivered by the accelerator to the DØ detector is one of the tasks of the Level 0 trigger. The Level 0 trigger logic identifies the presence of inelastic collisions and provides a fast determination of the z coordinate of the primary collision vertex. Timing information comes from two hodoscopes of scintillation counters mounted on the front surfaces of the end calorimeters at 140 cm from the center of the detector and thus provides a time resolution of $\approx$ 150 ps for particles hitting the scintillators.

Inelastic $p\overline{p}$ interactions are identified by detecting the two beam jets which result from the breakup of the incident beam particles. Diffractive interactions and beam–gas events are more likely to produce a single beam jet [18] and no coincidence. In the case of an inelastic interaction, the z coordinate position is determined from the difference in arrival time for particles hitting the two Level 0 detectors.

The luminosity is obtained by measuring the rate for inelastic collisions, selected as events satisfying a Level 0 coincidence with an interaction vertex located within 100 cm of the center of the detector along the beam pipe. These rates are corrected for lifetime, multiple interactions, and Main Ring Deadtime, before being converted to luminosity using the value of 55.5 mb for the non–diffractive inelastic cross section, as measured by other experiments [19]. The effective cross section seen by the scintillator counters is 42.9 mb, with an theoretical error of

7.6% [20], and a systematic error of 1.5% $\oplus$ 8% [21], giving a 12% error for the luminosity calculation.

DØ has the unique feature that the Main Ring accelerator runs through its calorimeter and its muon system. During a normal store the protons that are circulating in the Main Ring to produce antiprotons affect these two subdetectors. In particular the muon system suffers from loss of efficiency due to high voltage sag and amplifier saturation, and triggering on fake hits. For these reasons it is necessary to provide a Main Ring blanking scheme that vetoes events with any Main Ring activity in them, minimizing at the same time the introduced deadtime [22].

To understand the Main Ring blanking scheme it is necessary to briefly describe what happens during a $\overline{p}$ production cycle. The sequence starts when a single Booster bunch is injected into the Main Ring, filling up about 1/13 of the ring with 8 GeV protons. The beam begins ramping up to 120 GeV, passing through transition[4] 0.3 s later. Both processes are the source for large losses that are detected by DØ . 1.5 s later, the beam reaches 120 GeV and is extracted onto the $\overline{p}$ production target. The losses during this ramping period are much smaller than during injection/transition. After extraction, there is a quiet time when no beam is circulating. The whole cycle typically takes 2.4 s but can be made longer by increasing the quiet time interval.

A simple gate from $0.1 - 0.5$ s during a $\overline{p}$ production cycle effectively vetoes events during injection/transition and allows for the muon high voltage to recover. In addition, $p\overline{p}$ events where the Main Ring beam is present at DØ and the muon

[4] "Transition" is a point in the accelerator cycle when the phase of the RF accelerating fields has to be changed appropriately to maintain a stable bunch. It is described in more detail elsewhere[23].

system is live are vetoed, effectively covering any losses taking place during the ramping. The first veto introduces a deadtime of $\approx 17\%$, while the second adds a typical deadtime of 7–9%.

Figure 2.9 shows the luminosity delivered by the accelerator and the luminosity written to tape by the DØ detector as a function of time in days. For the Tevatron run that extended from April 1992 to May 1993, referred to as Run 1A, the overall DØ efficiency in accepting luminosity was 54%.

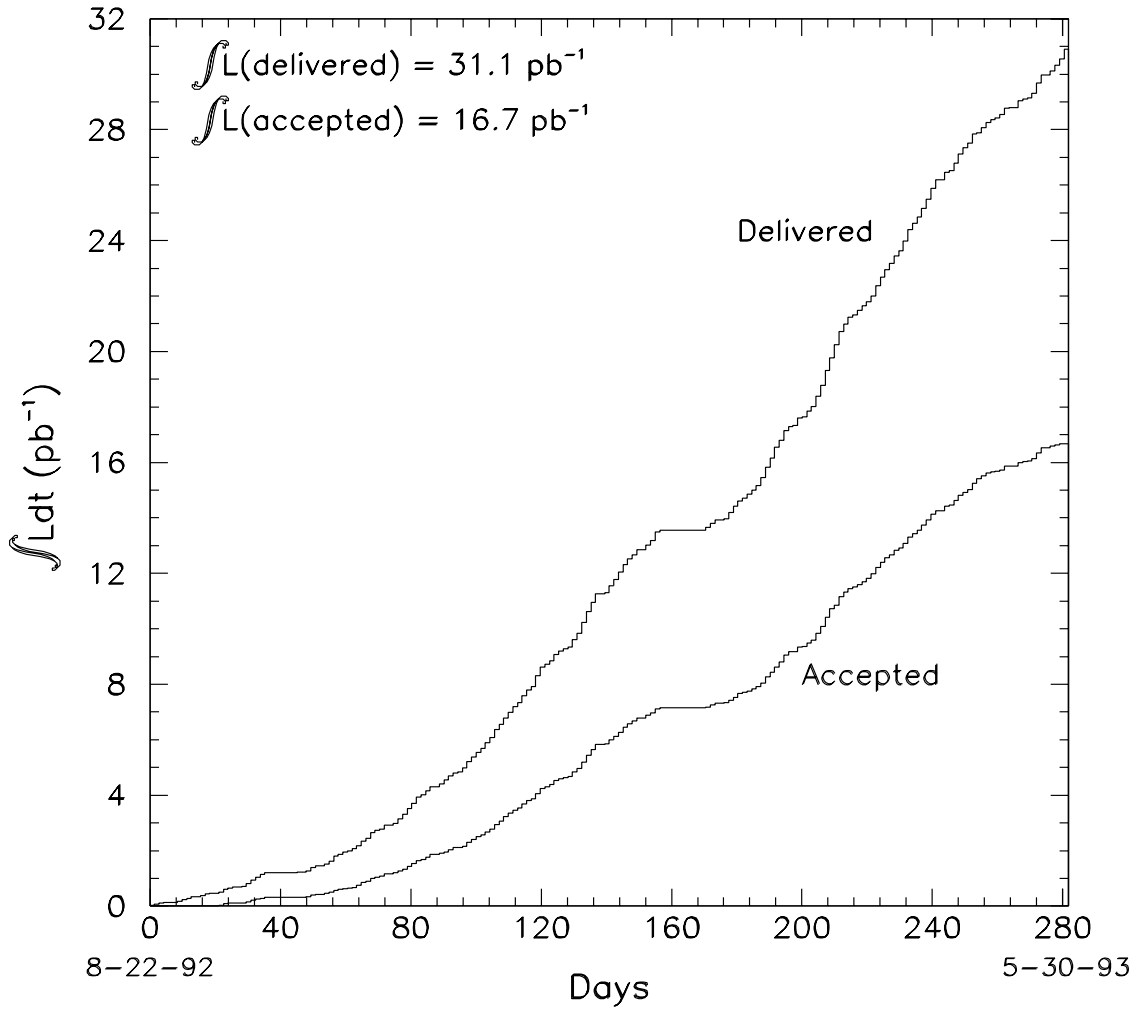

Figure 2.9: Luminosity delivered and accepted during DØ's run 1A.

Chapter 3

Event Reconstruction

The DØ reconstruction program (referred to as DØRECO) is responsible for converting raw data taken by the detector in the form of ADC counts and pulse heights into a reconstructed $\bar{p}p$ event, identifying the involved particles and their kinematic characteristics. Different algorithms have been developed to identify muons, electrons, photons, taus and jets. The program also calculates interaction vertices and the transverse energy imbalance of an event, referred to as the missing transverse energy ($\not{E}_T$). In the following sections each of these algorithms will be briefly described, making special emphasis on the muon reconstruction. In the last section some examples of objects reconstructed by these algorithms are shown in the form of DØ event displays.

3.1 Interaction Vertex Determination

The accurate determination of the interaction vertex in a $\bar{p}p$ collision is very important to calculate the transverse momentum of the resulting objects in the plane perpendicular to the beam pipe, referred to as p_T. The finite length of the proton and antiproton bunches circulating in the Tevatron cause collisions to occur over an extended distance along the beam pipe; furthermore, the interaction

vertex was displaced from the geometrical center of the DØ detector during the running period 1992–1993. Therefore the distribution of the z position of the interaction vertex is properly represented by a gaussian distribution with a width of about 30 cm centered at $z \approx -10$ cm of the center of the detector.

The reconstruction of the interaction vertex is accomplished by the central tracking detectors [24]. The vertex position in the $r\varphi$ plane is determined by the Vertex Chamber, being approximately stable during each run. For this reason the average position of the vertex is used for every event of a certain run.

The position of the vertex in the z direction is determined for each event by the Central or the Forward Drift Chambers, extrapolating the reconstructed tracks to intercept the beam axis. A gaussian fit is performed on each cluster of tracks associated to a vertex, yielding the z position with a resolution of 0.65 cm to 0.95 cm, depending on the number of tracks associated with the vertex and their angular distribution. The vertex with the highest number of tracks associated to it is identified as the primary vertex. Two vertices can be resolved if they are separated by more than 7 cm [25]. At the luminosities involved in DØ run 1A, the probability of multiple interactions is low, resulting in less than 20% of events having multiple vertices [26].

3.2 Muon Reconstruction

The muon reconstruction is divided into three parts [27], referred to as Hit Sorting, Track Finding and Global Fit. The first two are based on information provided exclusively by the muon chambers, while the Global Fit incorporates additional information from other subdetectors.

The **Hit Sorting** converts raw data provided by the muon chambers, into

points in the DØ global coordinate system that can be used by the track finding. To do so, it loops over the muon chambers, correcting the hits for time and delta time calibration constants, and checking the integrity of the data. The pad latch and the time information are used to assign the hit to the even or the odd cell of each set of paired cells, flagging inconsistent data. The address of each hit is then converted to a point in space in the global DØ coordinate system, using geometrical information for each particular chamber. The final step of the hit sorting is to transform the delta time and the pad information in a position along the wire, and the drift time in a drift distance perpendicular to the wire, correcting for time of flight.

The **Track Finding** is the process of recognizing that a certain set of hits correspond to the track of a single charged particle passing through the muon system. The Wide Angle track starts from a list of hits, looking for a BC track segment with at least four points. If found, a matching A layer segment with at least two hits is searched for. If no BC segment is found, the search starts by looking for an A layer segment with at least three points and then extends into the B or C layer. In either case, all segments are required to point to the vertex within a coarse road of 3 to 5 meters. Each segment found by this method is stored as a possible candidate, and the best one is selected based on its number of hits, pointing to the vertex and quality of fit.

If a track is found, a fit is performed in both the bend and the non–bend view[1] in order to resolve ambiguities. In the non–bend view a straight line is fitted through the magnet and the track is constrained to point to the vertex. In the bend view, the fit is performed differently depending on the number of layers with

[1]The bend view corresponds to the rz plane perpendicular to the wires, while the non–bend view is the xy plane, parallel to the wires.

hits that have been found. For three layer ABC tracks, a line is first fitted to the BC points and then extrapolated to the center of the magnet. The resulting point is combined with the A layer hits to fit the segment inside the magnet. In this case the vertex point is not used in the fit, unless there are less than three hits in the A layer. BC layer tracks use the projection of the BC segment to the magnet center plus the vertex point to define the segment inside the magnet. AB or AC layer tracks use the vertex point plus the A layer hits to define the inside segment, which is then extrapolated to the center of the magnet and combined with the B or C layer hits to define the outside segment.

In either case, the bend in the magnet gives a first pass muon momentum calculation. Finally a preliminary track quality flag is set, using the projection of the track to the vertex and the goodness of the fit in each view.

The procedure described above only applies to tracks that are completely reconstructed using only the Wide Angle Muon System. Track with larger pseudorapidity combining hits found in both the WAMUS and the SAMUS are reconstructed using other methods, some of which are still under development. The analysis that is being presented here only uses tracks wholly reconstructed within the WAMUS detector.

The last step in the muon reconstruction is referred to as the **Global Fit** [28]. It provides the final determination of the muon momentum and position, using information provided by the muon system, the Vertex Chamber and the Central or Forward Drift Chambers. This algorithm performs a fit using a least square method that considers seven parameters: four parameters describe the position of the muon track before the calorimeter in both the bend and the non–bend view as provided by the drift chambers; two parameters describe the bending of the

muon due to multiple scattering in the calorimeter as predicted by Monte Carlo with detector simulation, and the seventh parameter is the inverse of the muon momentum $1/p$. This seven parameter fit is applied on sixteen data points: two vertex position measurements provided by the Vertex Chamber and the Central or Forward Drift Chambers, four tracking measurements provided by the Central or Forward Drift Chambers, two angles representing the multiple scattering of the muon in the Calorimeter and eight measurements provided by the muon chambers inside and outside the magnet. The errors for the drift chamber parameters include the resolution of these subdetectors as well as the track fitting uncertainty; the muon track errors per hit are considered to be 0.2 cm in the bend–view and 1.5 cm in the non–bend view [29]. The multiple scattering in the muon system magnets is not being considered in this method.

High quality tracks resulting from the reconstruction steps described above are considered muon candidates; information about their spatial location, energy and quality are stored to be used by physics analysis programs.

3.3 Jet Reconstruction

A jet is defined as a collimated beam of hadrons resulting of a scattered parton than undergoes fragmentation [30]. There are several algorithms that can be used to reconstruct a jet. The most widely used at DØ is the fixed jet cone algorithm [31], that adds up the transverse energy deposited in the calorimeter cells in a radius of 0.7 in $\eta\varphi$ space. This is done in several iterations. It starts by finding an energy tower above 1 GeV, that is then considered a seed. The algorithm proceeds by looking at the nearest neighbors of this seed tower, joining them into the cluster if they are above 1 GeV. The average η and φ is calculated

and used as the center of the cone. All calorimeter cells within that cone are joined into the jet recalculating η and φ. This procedure is repeated until η and φ converge.

If the reconstructed object has more than 90% of its energy deposited in the electromagnetic section of the calorimeter, it is considered an electron or photon candidate. For electrons, the additional requirement that a Central Detector track matches the calorimeter cluster is applied.

3.4 Missing Transverse Energy Determination

If a neutrino is produced in a $p\overline{p}$ collision it will escape the detector without interacting. For an experiment to be able to reconstruct the neutrino's kinematic properties, it has to rely on momentum conservation. As the longitudinal momenta of the incident partons is unknown, only the conservation of the momentum in the plane perpendicular to the beam can be applied. This is known as the transverse momentum p_T.

In DØ the transverse momentum of the neutrino is determined by performing a vectorial sum of the transverse energy of all calorimeter cells [32]. If a muon is present in the event, its transverse momentum is added after subtracting the expected energy deposition of the muon in the calorimeter as estimated from Monte Carlo with detector simulation, to avoid double counting. The transverse momentum of the neutrino, also referred to as "missing energy" ($\not{E}_T$), is then considered to be equal in magnitude, but opposite in direction to this calculated quantity.

The $\not{E}_T$ resolution is dominated by the muon momentum resolution[2] for events

[2]The muon momentum resolution is discussed in detail in section 4.4.

containing any high p_T reconstructed muon.

3.5 Example of reconstructed events

The output of the reconstruction program contains a first pass identification of the various objects in the event (muons, electrons, jets, etc.), as well as their kinematic properties and quality parameters to be used in the final event selection. This identification is rather loose in order to assure a high reconstruction efficiency; the final cleanup is left to each analysis group which develops the particle identification as needed for its individual physics interest.

Examples of reconstructed events as can be viewed by using the DØ event display package [33] are shown in figures 3.1 and 3.2. The identified objects in those events are based on the loose assignments made by the DØ reconstruction program.

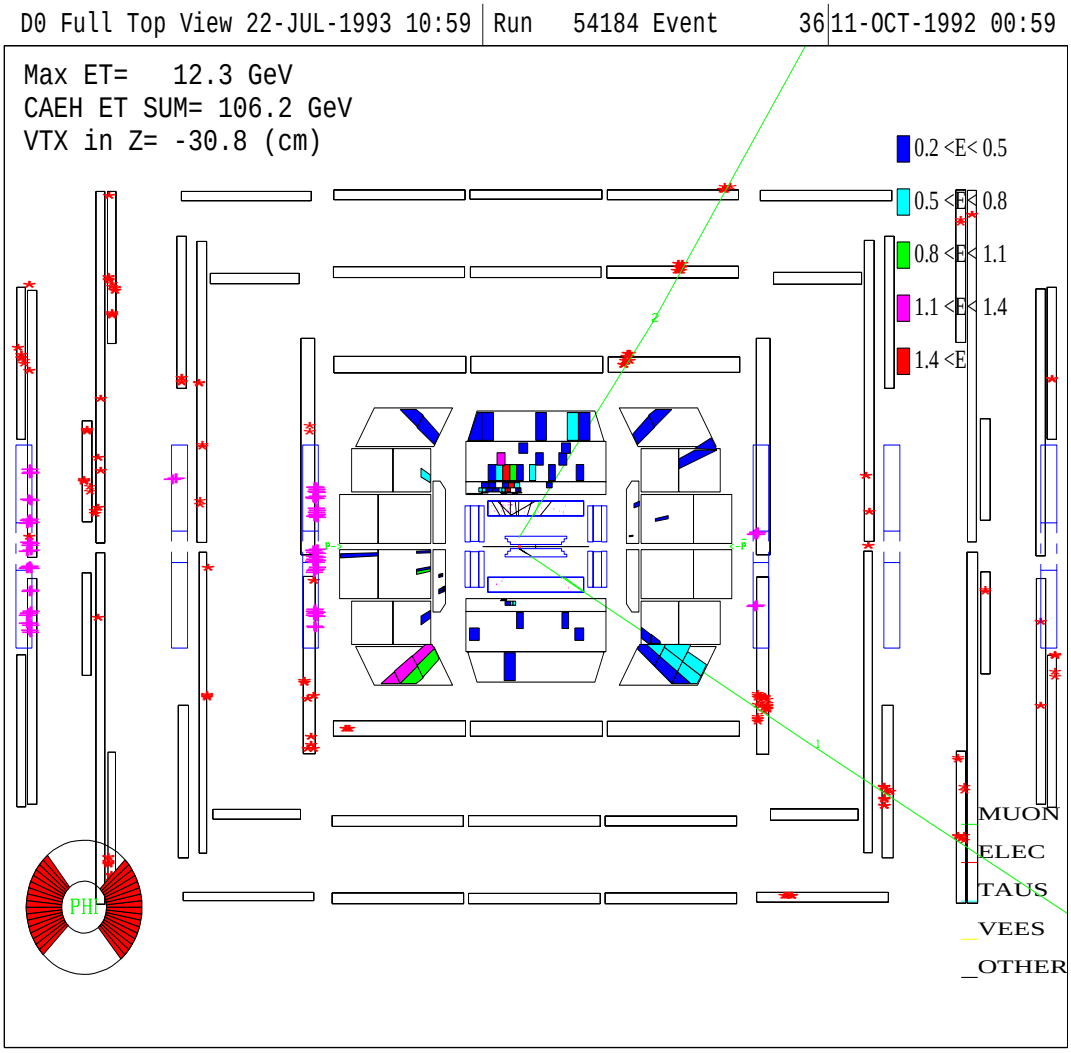

Figure 3.1: The full DØ top view of a $Z \to \mu\mu$ candidate is shown. Each of the muon tracks has hits in the three layers of the muon system, a matching track in the central detectors and points to the reconstructed interaction vertex, that is displaced from the geometrical center of the detector. A small jet has also been reconstructed in the central calorimeter.

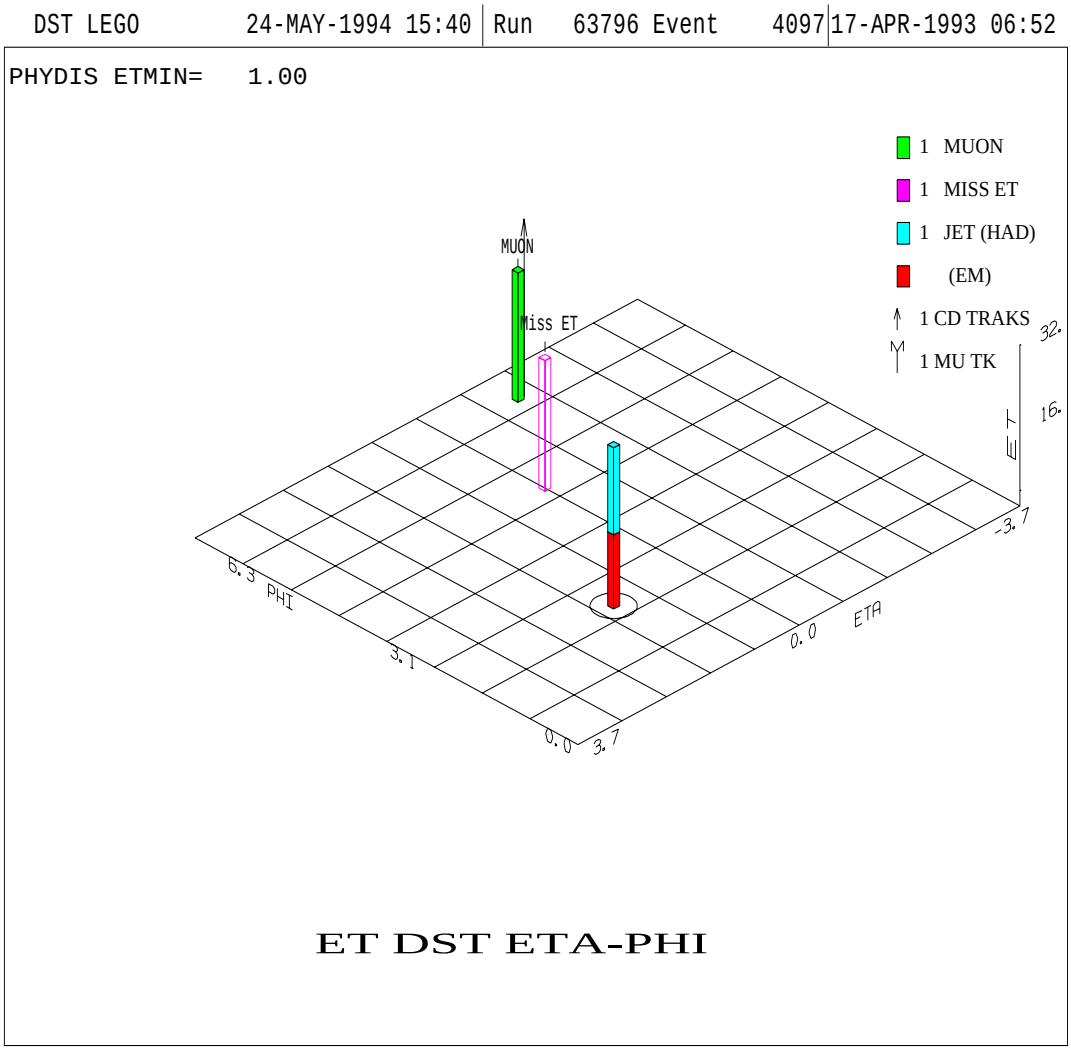

Figure 3.2: The DØ lego plot is shown for an event where a muon and a neutrino (represented by the missing energy $\not{E}_T$) recoil against a jet. All the objects found by the reconstruction program are clearly labeled, their transverse energy can be observed on a vertical scale and their relative position in the $\eta\varphi$ space is also indicated. The η coordinate of the $\not{E}_T$ is not actually measured, so it is displayed arbitrarily at $\eta = 0$.

Chapter 4

Monte Carlo Event Simulation

In elementary particle applications, "Monte Carlo" is usually a simulation technique based on a random number generator that is used to directly represent what happens physically. Within DØ, different software packages are used to produce Monte Carlo data. First, an event generator is used to simulate a $\overline{p}p$ collision. Then, a detector simulation represents the passage of the particles through the detector, and a trigger simulator predicts whether that event would have been selected for detector readout. Finally, the simulated detector output gets reconstructed by the same program used on real data, reaching the user in the same format as the collider events for offline analysis. It is very important to compare the output of these predictions with real collider data and to introduce further refinements needed to improve the Monte Carlo representation of the reality. Examples of such comparisons are shown in Appendix A.

In the next sections each of the steps involved in the Monte Carlo simulation of collider data will be briefly described.

4.1 Event Generators

Although various event generators are used within DØ to simulate different final states of the collision of a proton with an antiproton at a center of mass energy of 1.8 TeV, the one that was used almost exclusively [1] for the $W/Z \rightarrow \mu$ analysis has been ISAJET [34].

The ISAJET Monte Carlo event generator is based on perturbative QCD plus phenomenological models for parton and beam jet fragmentation. The events are generated following four basic steps:

1. **Hard Scattering**

   A primary hard scattering is generated according to the appropriate QCD cross section for simple two body scattering based on the first order Feynman diagrams for the required process.

2. **QCD Evolution**

   All partons which participate in the hard scattering are evolved through repeated parton branchings, generating both initial and final state radiation and allowing for the possibility of many jets. This cascade process continues until the energy of the partons fall below 6 GeV.

3. **Hadronization**

   Hadronization is the process dictated by color confinement where only colorless objects are allowed to emerge from the interactions. This process has to be described based on an empirical scheme; in ISAJET quarks and

[1] The PYTHIA [35] event generator was used to study the systematic error in the geometric acceptance due to the choice of parton distribution functions, as described in section 6.1.1.

gluons are fragmented into hadrons using the Feynman–Field fragmentation scheme [36].

4. **Beam Fragmentation**

   The beam fragmentation accounts for the remaining constituents of the proton and the antiproton that were not involved in the hard scattering. They are added by superimposing a Monte Carlo generated minimum bias event on top of the hard scattering event.

4.2 Detector Simulation

The Monte Carlo simulation of the DØ detector has been very important during the detector design, and during the development and optimization of the reconstruction code and the physics analysis programs. In order for the simulation to be useful to all these different tasks, the events had to be simulated down to the level of the raw ADC counts, and include all detailed physical processes of scattering and interactions.

The FULL DØGEANT Monte Carlo is based on the GEANT [37] package developed at CERN. This package provides tools for specifying volumes containing particular materials and the framework for transporting particles through these volumes with appropriate physical scattering and interaction processes included. It also provides the tools to transform the energy deposited in each volume into digitalized signals.

The geometric simulation for the DØ detector is quite detailed, specifying the central tracking chambers and the muon detector down to the level of the sense wires, cathode material and support structures. The calorimeter modelling is less

complete due to the complexity of the showering process, reaching a compromise between accurate simulation and CPU time requirements. Furthermore, as the simulation of hadronic showers in the calorimeter consumes much computer time, the SHOWER LIBRARY [38] method has been developed.

The idea behind this method is to make a library of single particle showers generated by using the full simulation of the calorimeter. In subsequent generations, the shower information is directly taken from the library resulting in a effective speedup of the simulation process. Obviously it is impossible to have an exactly matching shower in the library for each generated object. Therefore, it is necessary to represent the particles with corresponding showers based on a few common parameters. Five quantities have been chosen: z vertex position, η, φ, momentum and particle identity.

The agreement between the SHOWER LIBRARY and the FULL DØGEANT simulations is excellent [39]. Furthermore, even when using the SHOWER LIBRARY, the passage of muons through the calorimeter is simulated in full detail. As this analysis is mainly concentrated in identifying muons, SHOWER LIBRARY Monte Carlo samples have been used both to simulate signal and background samples.

4.3 Trigger Simulation

DØ has developed two packages(L1SIM and L2SIM) to simulate the different levels of trigger decisions that are made on real collider data. Both simulations are deterministic and involve no random number generator.

L1SIM [40] is a program that simulates the Level 1 Trigger System, and performs the same computations offline using Monte Carlo or real collider data. It

simulates the following trigger subsystems:

1. the Level 1 Calorimeter Trigger
2. the Level 1 Muon Trigger
3. the Level 1 Decision
4. the Level 1.5 Muon Trigger
5. the Level 1.5 Decision

The triggering requirements are programmed into the simulator using the same set of directives that are used online during normal data taking, and reproducing the actual configurations. As output L1SIM generates the simulated trigger decision which is added to the data by storing them into trigger banks.

The Level 2 triggers are software routines that can be run on real data or Monte Carlo events using the L2SIM [41] package. As it is a software trigger it can be used both to filter events based on Level 2 requirements and to actually simulate the triggers.

As for the Level 1 simulation, the actual configuration files and trigger decisions used during collider data taking are also used in the simulation.

4.4 Realistic detector effects

Although the Monte Carlo simulation of the DØ detector is quite accurate, there are a number of extra steps that have to be taken to make it even more realistic. One that is especially important for any high p_T muon analysis is related to the muon momentum resolution.

The standard DØ detector simulation package assumes for the muon detector the design resolution of $dP/P = 20\%$, which is certainly true for low momentum muons, but has not yet been achieved for higher momentum tracks. As the momentum resolution has been changing during time as calibration and alignment constants were updated, it is impractical to generate Monte Carlo event samples at various resolutions. Furthermore, the simulation can not predict certain time dependant effects such as changing hardware chamber efficiencies. A program referred to as MUSMEAR [42] has been developed to account for these time dependent efficiencies and resolutions.

This smearing package contains values for resolution factors for Times and Delta Times and an offset in the muon chamber alignment. In addition, it contains efficiencies for Times, Delta Times and Pad Latches for each PDT and the option of turning off complete chambers. Each of these parameters has been tuned by comparing the distributions produced by MUSMEAR with distributions obtained from collider data.

The values for the resolutions have been obtained from data as a result of the Times and Delta Times calibration [43]. The additional misalignment factor is tuned to fit the shape of the $Z \rightarrow \mu\mu$ and $W \rightarrow \mu\nu$ mass distributions, following the procedure described in reference [44]. Based on these comparison studies, it was determined that for the data recorded by DØ during the running period 1992–1993, the muon system momentum resolution is consistent with a drift resolution of 700μm, a delta time resolution of 20 cm and a chamber misalignment of 3 mm.

Figure 4.1 shows the transverse mass distribution for a $W \rightarrow \mu\nu$ sample, as well as the invariant mass distribution for a $Z \rightarrow \mu\mu$ sample, for Monte Carlo samples without detector simulation, with DØ GEANT simulation (design resolution), and

with MUSMEAR simulation. It can be observed how the detector resolution degrades the shape of the distributions.

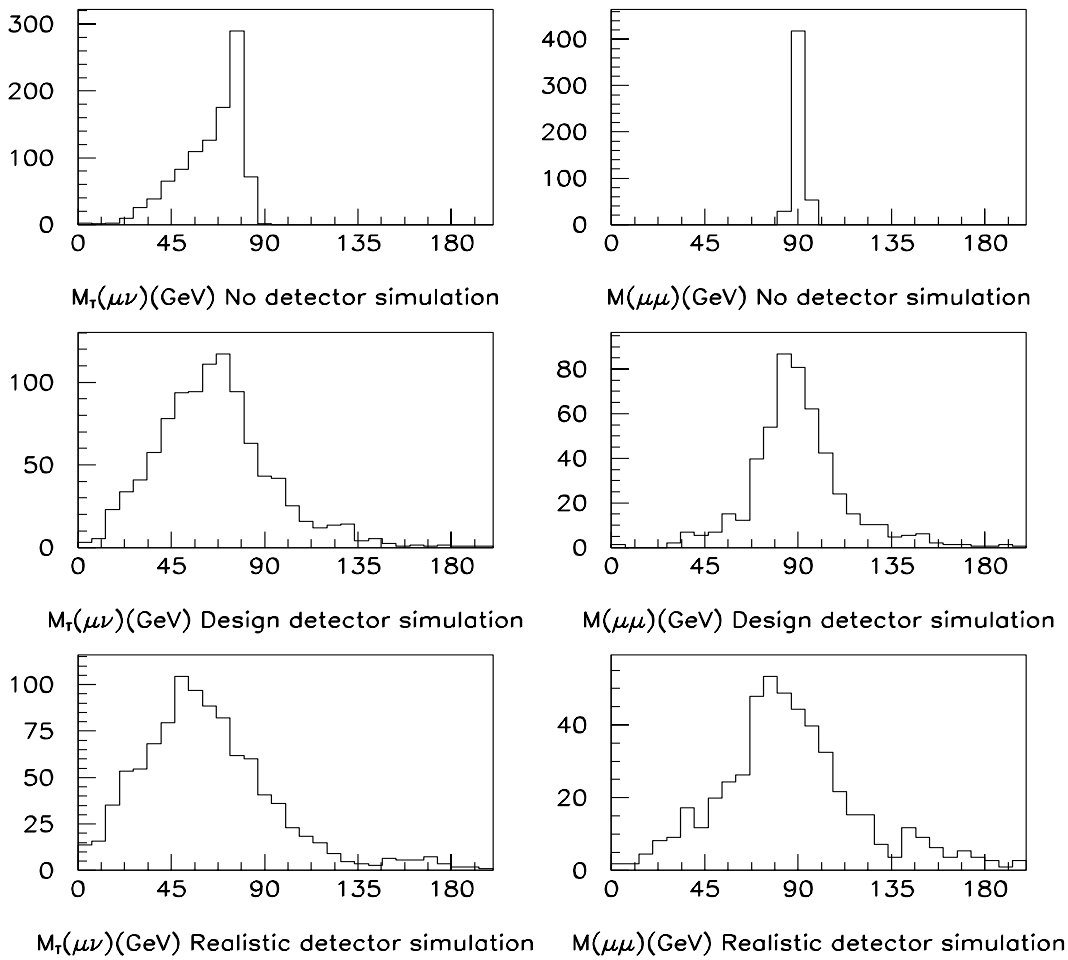

Figure 4.1: Transverse mass distribution for a $W \to \mu\nu$ sample and invariant mass distribution for a $Z \to \mu\mu$ sample generated without detector simulator and with the design and actual resolution detector simulation. The $W(Z)$ histograms are normalized to the number of events in the sample with no detector simulation.

In the past [46], the muon momentum resolution has been parameterized as a function of the muon momentum with a functional form given by

$$\Delta(1/p) = \sqrt{(A/p)^2 + B^2}\,(\mathrm{GeV/c})^{-1},$$

with $A = 0.2$ for the multiple Coulomb scattering term and $B = 0.01$ for the position–dependent term. Although this parameterization has not been used in the present analysis, it is compared in figure 4.2 with the results obtained from a sample of smeared $W \to \mu\nu$ Monte Carlo events, for completion purposes.

The individual muon chamber efficiencies have also been calculated from data by comparing the number of planes with hits on a track to the number of planes on the track. This is done for each of the signals (Pad Latch, Times, Delta Times), and the result is included into the smearing package. The efficiencies obtained from smeared Monte Carlo agree within a few per cent with the results obtained from data [45]. For the data recorded by DØ during the running period 1992–1993, the different efficiencies per hit are $\approx 97\%$ for Drift Time and $\approx 91\%$ for Delta Time. The efficiencies for the Pad Latches are very much dependant on the geometric position of the chambers with respect to the beam; the efficiency for chambers perpendicular to the direction of the incident beams is degraded due to beam background. The solution to this problem is still under investigation.

For A layer chambers both in CF and in EF, and for CF B and C layer chambers, the pad latch efficiency is $\approx 90\%$. For the B and C layers in the EF though, the pad latch efficiency is found to be much lower, $\approx 40 - 60\%$ depending on how close the chamber is from the beam pipe and also depending on the incoming direction of the protons and the antiprotons. Given the poor EF chamber performance and the fact that the trigger decisions are based entirely on the Pad Latches, (requiring that 2 out of 3 pad latches have been set for the B and

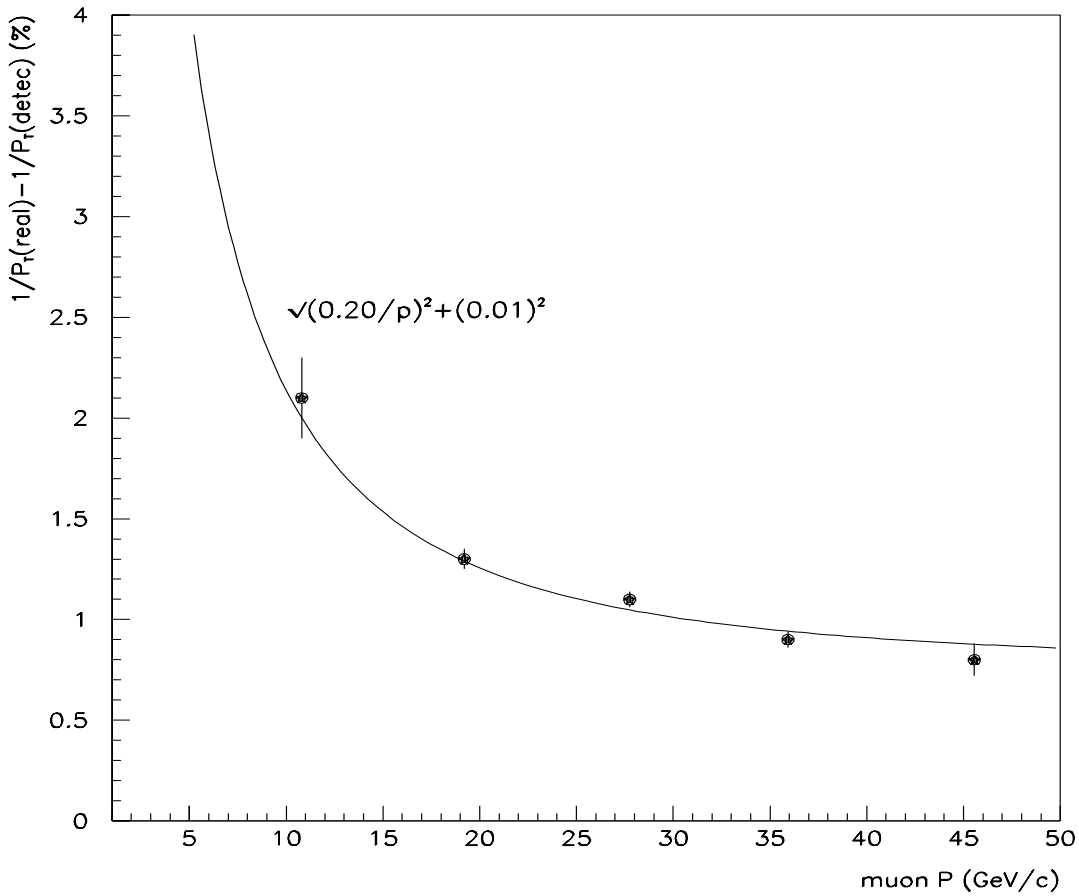

Figure 4.2: Parameterization of the muon momentum resolution as a function of muon momentum. The dots are points obtained from a sample of smeared $W \to \mu\nu$ Monte Carlo events; the full line is the parameterized representation of the muon momentum resolution.

C layers, and 3 out of 4 (2 out of 4) for the EF (CF) A layers to pass the event), the result is a very low trigger efficiency for detecting muons in pseudorapidity regions of $\eta > 1$.

Chapter 5

Event Selection

As was mentioned in section 1.2, the experimental signature of intermediate vector bosons decaying in their muonic channels is the presence of a high p_T isolated muon accompanied by a second muon for the Z or by an imbalance in the transverse energy of the event for the W boson. The following discussion describes the offline identification procedures for muons and the actual $W \rightarrow \mu\nu$ and $Z \rightarrow \mu\mu$ candidate sample selection.

A description of the data set used for the cross section calculations is included in the last section. This analysis is based on data recorded during the first operating run of the DØ detector. Therefore a considerable amount of effort was invested in the first time identification of the elements used in the event selection of the different physics analyses, in particular in the identification of high p_T isolated muons.

5.1 Offline Muon Identification

This section describes the selection of high p_T single isolated muons which are used to identify both W and Z bosons in their muonic decay channel. The factors are divided into those which would affect the finding of a "loose" muon (mostly

Table 5.1: Summary of selection cuts used to define a single high p_T isolated muon.

Loose Muon	CF	EF
Muon Pseudorapidity	$\lvert\eta_\mu\rvert \leq 1.7$	
Muon Quality Flag $IFW4$	$IFW4 \leq 1$	
Magnetic Field check	$\int B \cdot dl > 0.6$ GeV for $\lvert\eta\rvert > 0.7$	
Muon Calorimeter Deposition	$Cal(1nn) \geq 1.0$ GeV	$Cal(1nn) \geq 1.5$ GeV

Tight Muon	CF	EF
Muon Global Fit Cut	$0 \leq \chi^2 \leq 100$	
Muon–CD track match	$\Delta\theta \leq 0.12$ radians and $\Delta\varphi \leq 0.04$ radians	
Bend View Impact Parameter	$\lvert b_{bend}\rvert \leq 15$ cm	$\lvert b_{bend}\rvert \leq 20$ cm
Non Bend View Impact Parameter	$\lvert b_{non-bend}\rvert \leq 20$ cm	$\lvert b_{non-bend}\rvert \leq 25$ cm
Floating time shift	$t_0^f \leq 100$ ns	
2nn Isolation Cut	$I_\mu \leq 3\sigma$	
Halo Cut	$E(0.6 - 0.2) \leq 6$ GeV	

effects which lose a muon) and those which would affect the finding of a "tight" muon (mostly effects which reduce the quality of a muon) [47]. The selection cuts are summarized in table 5.1 and briefly described in the following discussion.

Figures 5.1 to 5.6 show distributions for each of the selection cuts for "signal" samples. The shape for each of the quality variables was taken from a sample selected by tightening all the other quality cuts except the one in question, on which no cut was applied at all. The signal shape for variables used to define the isolation of a muon was taken from a subset of the $W \rightarrow \mu\nu$ sample with no jets in the opposite half of the detector (in φ) with respect to the muon.

5.1.1 Loose Muon Definition

Four factors contribute to the definition of a "loose" muon:

- **Muon Pseudorapidity**

  This analysis has been restricted to muons contained entirely within the WAMUS detector by requiring that $|\eta_\mu| \leq 1.7$, for the muon system performance is not fully understood in the overlap region between the WAMUS and the SAMUS detectors which begins beyond this point.

- **Muon Quality Flag** $IFW4$

  Although the muon reconstruction program [27] applies very loose cuts on a candidate tracks to pass it along as a muon candidate, it does require that certain minimum conditions are satisfied to reduce the number of muon candidates that reach the user for offline analysis. Several quantities are calculated during the track fitting stage that carry information about the reconstructed object and can be used to set a preliminary track quality flag. The primary separating factors are the quality of the track fit both in the bend and in the non–bend view (as measured by the rms residuals of the hits from the fitted track) as well as the impact parameters with respect to the event vertex of the extrapolated muon track in both views[1]. Other discriminating factors are based on the number of hits associated with a given track; the code checks the number of hits used to fit the track, and whether or not a given track projects to a muon chamber but hits from that module are not associated to the track.

[1] Angular and momentum dependent values are used to decide on the quality of the track projections to the vertex.

Based on very loose quality cuts on these quantities, the muon reconstruction code adds one count to the Muon Quality Flag known as $IFW4$ for each quantity that fails a cut. $IFW4$ thus counts the number of "bad" track qualities and is equal to zero for a "golden" track. Only tracks with $IFW4 \leq 2$ are passed on as muon candidates for offline analysis. Furthermore, most of the offline analyses, including the one presented here, tighten this cut by requiring that

$$IFW4 \leq 1$$

for any muon candidate.

Although a preliminary muon reconstruction is performed in Level 2, the existence of a reconstructed muon with $IFW4 \leq 1$ is not guaranteed and has to be explicitly required during the offline analysis.

- **Fiducial Cut**

  Muons that pass through the gap between the CF and the EF toroids (roughly corresponding to a region of $0.8 < |\eta| < 1.0$) do not traverse much magnetized iron and therefore will have a poor momentum determination. To enforce a proper muon momentum measurement a cut is done on the minimal value of the integral of the magnetic field along the muon track requiring that

$$\int B \cdot dl \geq 0.6 \text{ GeV},$$

  where the field integral is expressed in terms of the lateral momentum kick of a particle passing through that field. (Note that this corresponds to a

value of $\int B \cdot dl \geq 2$ Tm.) Furthermore, the DØ detector only has about 9 interaction lengths for this η range, while it is typically 13–18 interaction lengths anywhere else (see figure 2.6); therefore the probability of hadron punchthrough out of the calorimeter increases in this region [48].

- **Calorimeter Confirmation**

  Real muons produced in collider events deposit energy in the calorimeter that is consistent with the passage of one minimum ionizing particle (mip). On the other hand, tracks originating from cosmic ray muons or from spurious hits in the muon system chambers do not originate from the interaction vertex and therefore less energy in the calorimeters is expected along the path from the muon chambers to the vertex. This can be evaluated measuring the energy deposited in the calorimeter cells traversed by the muon plus their first nearest neighbors, which roughly corresponds to a cone[2] in $\eta\varphi$ space of $\Delta R = 0.1$.

  In order to separate the muons produced in $\overline{p}p$ collisions from the cosmic/combinatoric background based on their energy trace in the calorimeter, it is required that

  Calorimeter deposition (muon cell + 1nn)$\geq$ 1.0 GeV for CF tracks

  Calorimeter deposition (muon cell + 1nn)$\geq$ 1.5 GeV for EF tracks

  Figure 5.1 shows the Calorimeter deposition distribution for a signal and a background sample. The background shape was obtained selecting collider

[2] ΔR is defined as $\Delta R = \sqrt{\Delta\eta^2 + \Delta\varphi^2}$.

events with two isolated high p_T muons that are back to back in θ and φ ($\Delta\theta(\mu_1, \mu_2) > 170^o$ and $\Delta\varphi(\mu_1, \mu_2) > 160^o$). Such a sample is assumed to be dominated by cosmic rays and has been used to obtain all the background distributions in this chapter.

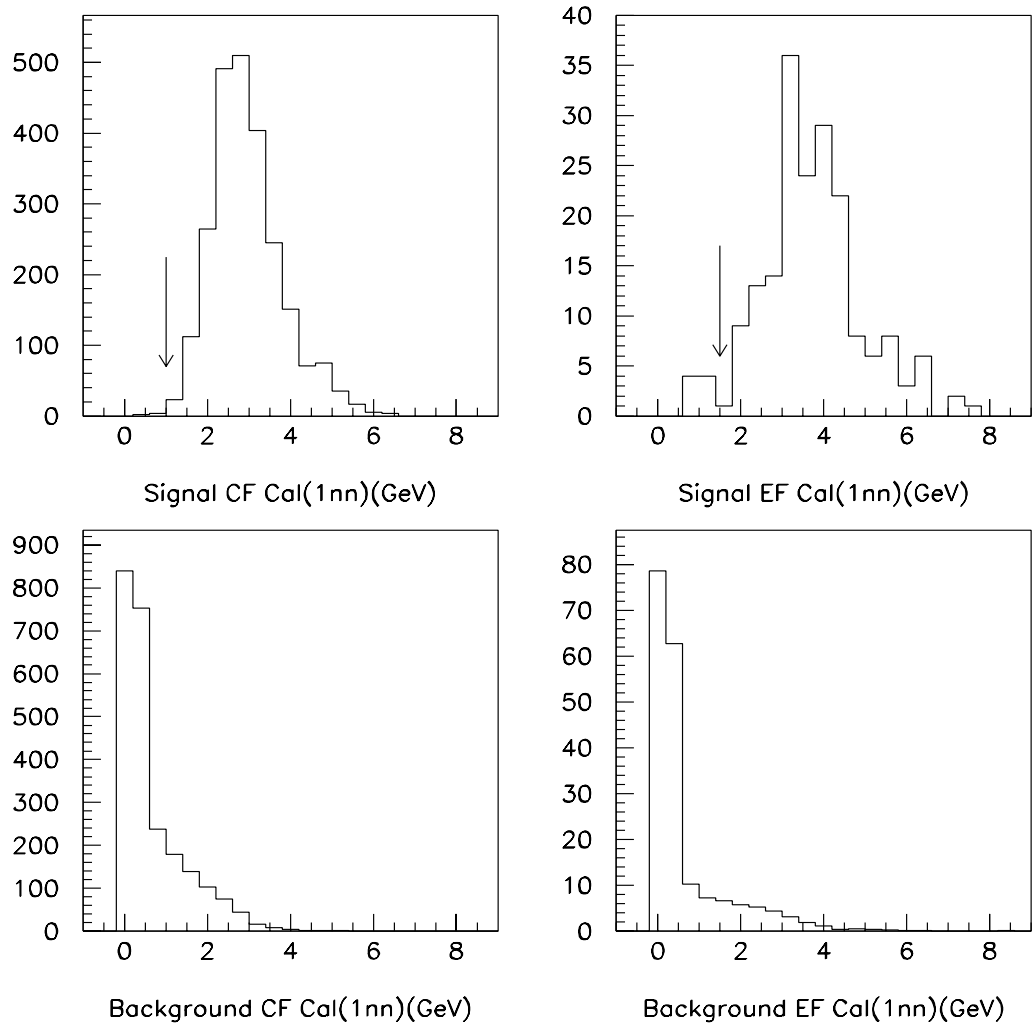

Figure 5.1: The energy deposited in the calorimeter in the direction of the muon is plotted for a signal and a background sample for CF and EF muon tracks.The arrows indicate the position of the quality cut. Real muons produced in collider events deposit an energy in the calorimeter that is consistent with the passage of one minimum ionizing particle; tracks that do not originate from the interaction vertex deposit less energy in the calorimeter along the path from the muon chambers to the vertex.

5.1.2 Tight Muon Definition

Six quantities are used to define a "tight" muon:

- **Muon Global Fit**

  The quality of the Muon Global Fit [28] for a track, which is measured by the value of the χ^2 of the fit, depends not only on muon system track parameters but also on information provided by the central tracking for a CD track found to match the muon track in question, thus providing a quantitative measurement of the global quality of the muon track.

  For a muon to pass the selection criteria based on the value of the Muon Global Fit χ^2, it is required that

  $$0 \leq \chi^2 \leq 100$$

  where a value for the χ^2 of -1 corresponds to muon tracks that do not have a matching Central Detector track.

  The χ^2 distribution for signal and background samples are plotted in figure 5.2.

- **Central Detector Track match**

  A tighter requirement on the quality of the muon–CD track match has been introduced to minimize the number of fake matches between muon and CD tracks given the big cone sizes allowed for matching in the standard reconstruction program ($\Delta\varphi < 0.45$ radians, $\Delta\theta < 0.45$ radians). This is especially important in the EF region were the density of CD tracks is very high and spurious track matching is more likely to occur.

In order to reduce the number of fake matches it is required that a CD track is located within a cone around the muon given by

$\Delta\varphi$(muon track, CD track)$\leq$ 0.04 radians,

$\Delta\theta$(muon track, CD track)$\leq$ 0.12 radians.

Figure 5.3 shows the distribution of these two variables for a signal sample.

- **Muon Impact Parameter**

  The impact parameter for muon tracks in the non–bend view is calculated extrapolating the muon trajectory outside the magnet back towards the primary interaction vertex. (Note that the trajectory inside the magnet is constrained to the interaction vertex in the xy plane). The bend view impact parameter is obtained from the trajectory inside the magnet.

  For any prompt muons the impact parameter distributions peak at zero with a finite width produced by multiple scattering and measurement errors; for cosmic rays the primordial impact parameter distributions are flat, although the quality cuts imposed cause a broad enhancement of these distributions near zero [49].

  Requiring the muon track to pass close the interaction vertex reduces the cosmic/combinatoric contamination. In this analysis the muon track is constrained to point to the primary interaction vertex requiring that

  |Impact Parameter Bend View| $\leq$ 15 cm (20 cm) for CF (EF) tracks

  |Impact Parameter Non–Bend View| $\leq$ 20 cm (25 cm) for CF (EF)

Figure 5.4 shows the distribution for the impact parameters in a signal sample.

- **Floating time shift**

  The floating time shift t_0^f is defined as the difference between the t_0 (the time origin for the calculation of the drift distances) which gives the best fit and the nominal t_0 corresponding to the time of the beam crossing. It is obtained by allowing the t_0 used in calculating all muon drift distances on a track to float in the track fit. Prompt muons give a t_0^f distribution which peaks at zero since they are produced in coincidence with beam crossing. For cosmics, the time of arrival is random, but in order to pass the trigger and be reconstructed the muon must be within about ± 400 ns of beam crossing (total drift time is ≈ 750 ns), and the probability is enhanced for cosmics which arrive a bit early [49].

  Restricting the values for t_0^f to be consistent with tracks originating in time with the beam crossing provides another useful tool for rejecting cosmic/combinatoric contamination. To do so it is required that

$$t_0^f \leq 100 \text{ ns}.$$

  Figure 5.5 shows the distribution of t_0^f for signal and background samples.

- **Muon Isolation Variable**

  The two nearest neighbors isolation variable I_μ is measured by summing the calorimeter energy in cells hit by the muon and their two nearest neighbors, then subtracting the expected contribution from the muon ionization and

dividing the difference by the expected error. For an isolated muon, such as the ones originating from W and Z events, the energy deposited close to the track is expected to be consistent with one mip plus some additional energy due to the underlying event. For non–isolated muons located close to a jet, the energy deposited around the track is expected to be much higher due to the energy of the jet.

The cut

$$I_\mu \leq 3\sigma$$

accepts muons where the sum of the energy in cells hit plus 2nn is less than 3σ above the amount expected from the muon ionization alone, effectively rejecting muons that are located very close to a jet, such as the ones originating from b- and c- decays [49].

- **Halo Cut**

  The muon halo energy $E(0.6) - E(0.2)$ is defined as the difference in the energy deposited by the muon in the calorimeter in an $\eta\varphi$ cone of 0.6 around the muon minus that in a cone of 0.2 . Note that the cone of 0.2 used in the determination of $E(0.2)$ is equivalent to the region of hit cells plus two nearest neighbors used in I_μ.

  It provides a method to further reject QCD background by requiring that

$$E(0.6) - E(0.2) \leq 6 \text{ GeV}.$$

Figure 5.6 shows the distribution for I_μ and for $E(0.6) - E(0.2)$ for a sample of isolated muons.

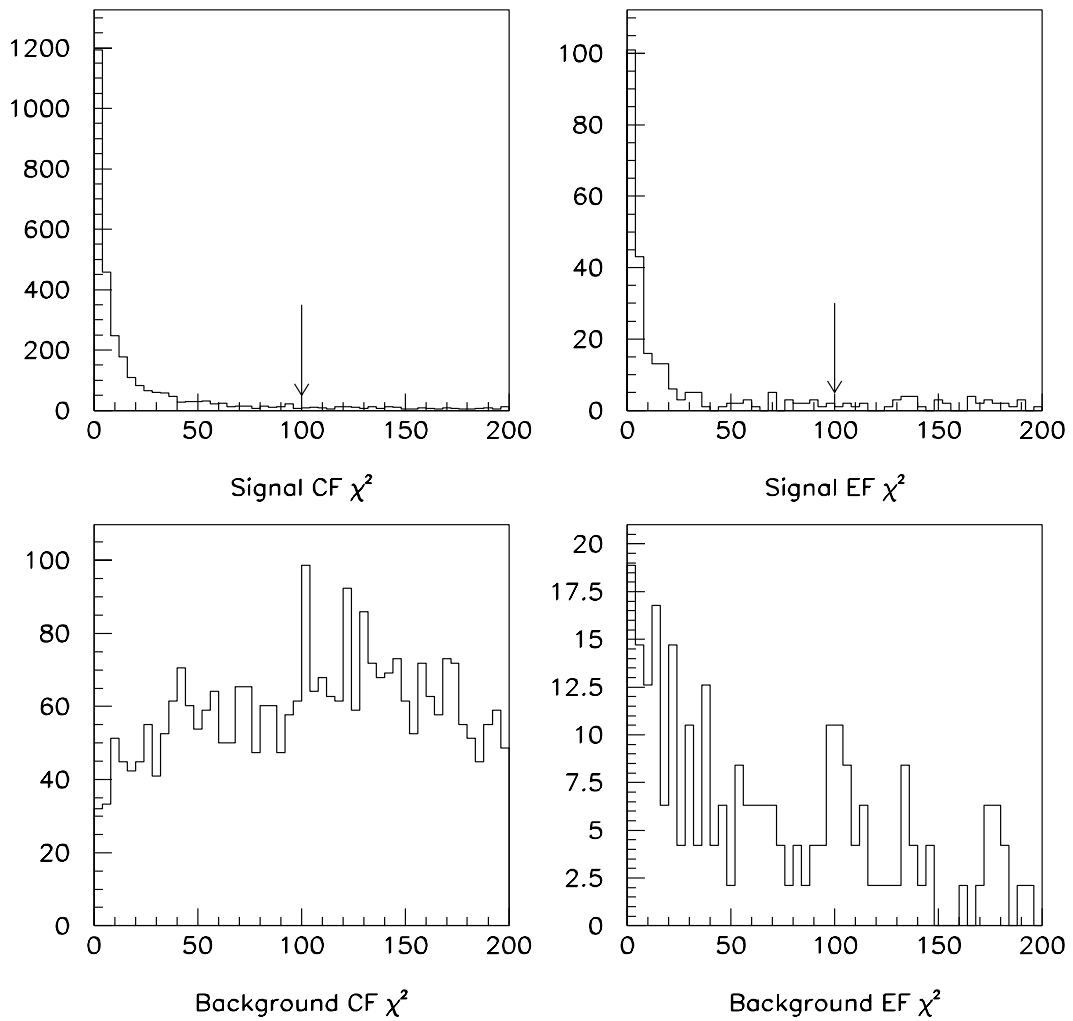

Figure 5.2: The Muon Global Fit χ^2 is plotted for a signal and a background sample for CF and EF tracks. The arrows indicate the position of the quality cut.

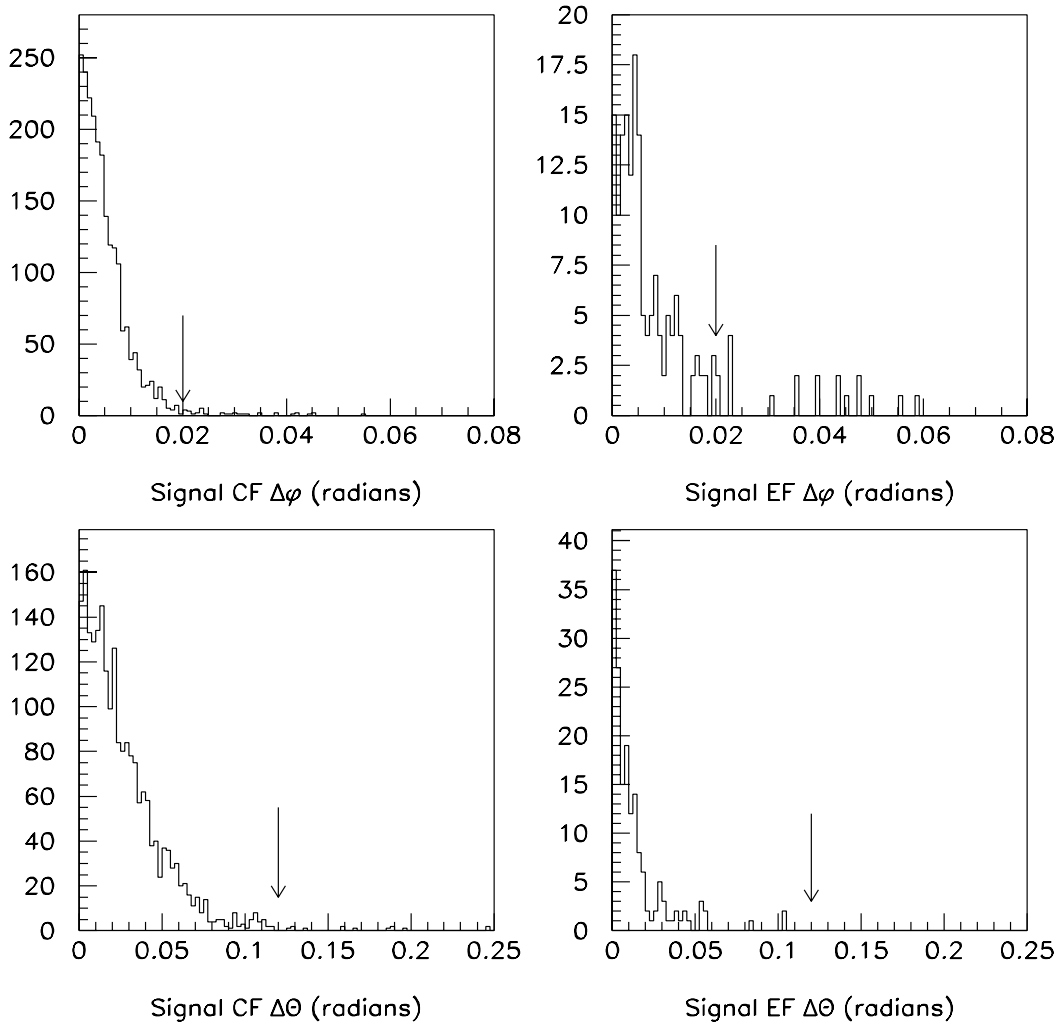

Figure 5.3: The distributions for $\Delta\varphi$ and $\Delta\theta$ between the muon and the matching CD track are plotted for CF and EF muon tracks. The arrows indicate the position of the quality cut. Tightening the allowed opening angle between the muon and the matching CD track reduces the number of fake track matches.

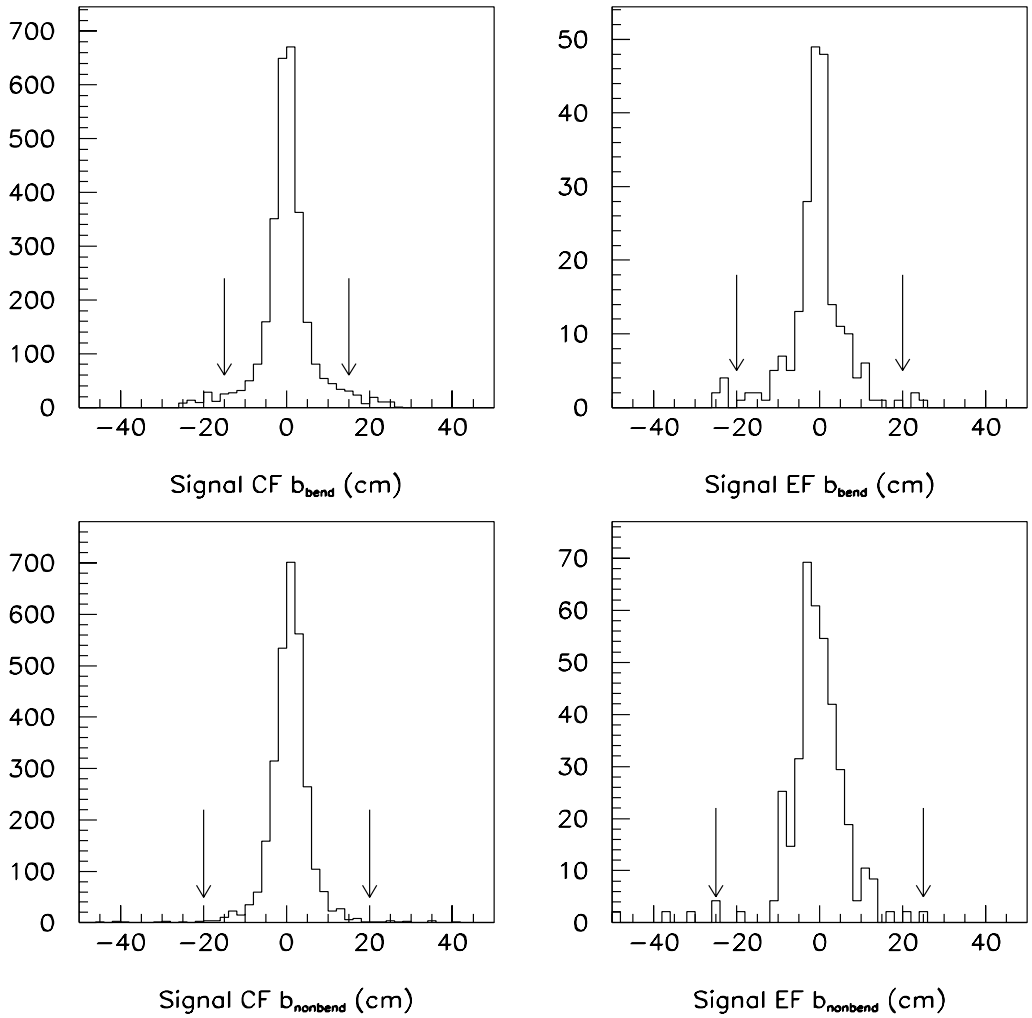

Figure 5.4: The muon impact parameters are plotted for CF and EF tracks.The arrows indicate the position of the quality cut. For any prompt muons the impact parameter distributions peak at zero with a finite width produced by multiple scattering and measurement errors; for cosmic rays the primordial impact parameter distributions are flat.

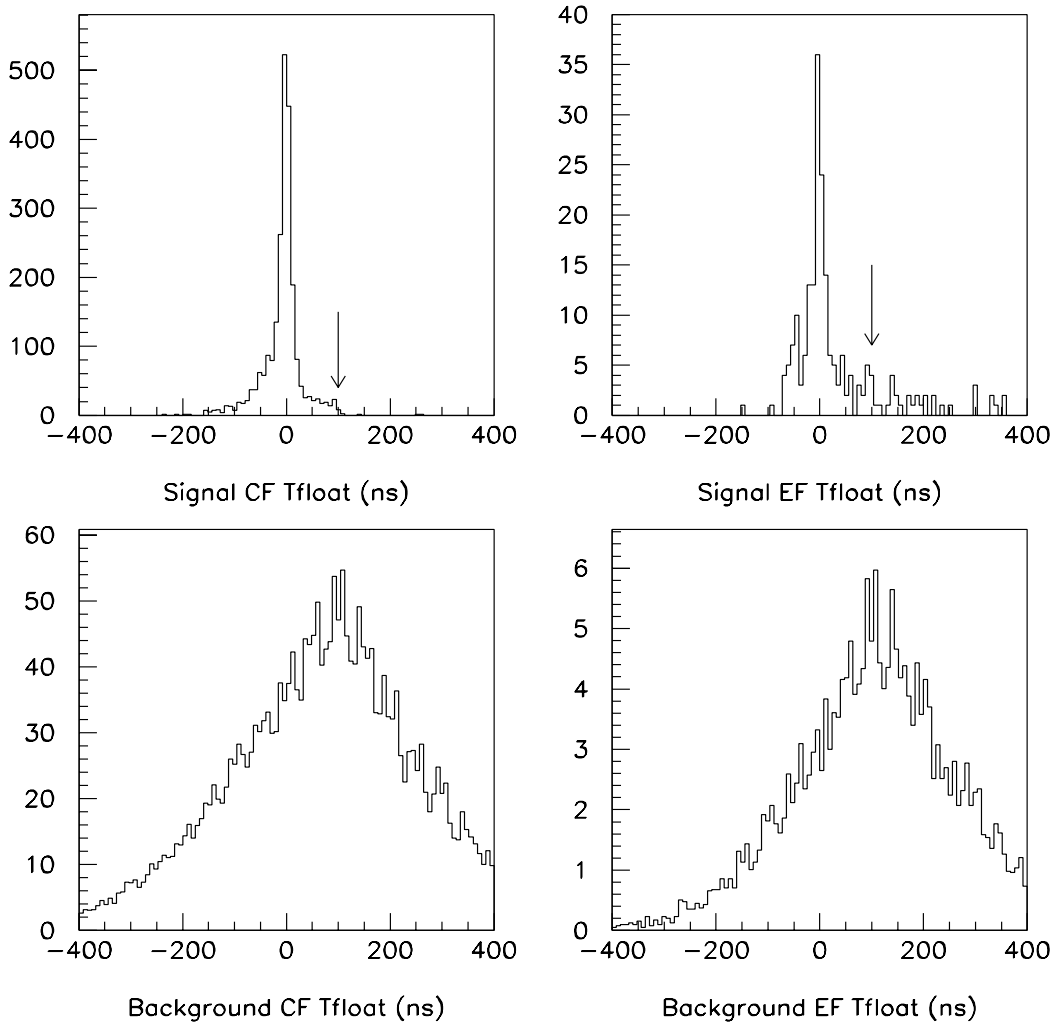

Figure 5.5: The floating time shift t_0^f is plotted for signal and background samples for CF and EF tracks.The arrows indicate the position of the quality cut. Prompt muons give a t_0^f distribution which peaks at zero since they are produced in coincidence with beam crossing. For cosmics, the time of arrival is random, and the probability is enhanced for cosmics which arrive a bit early.

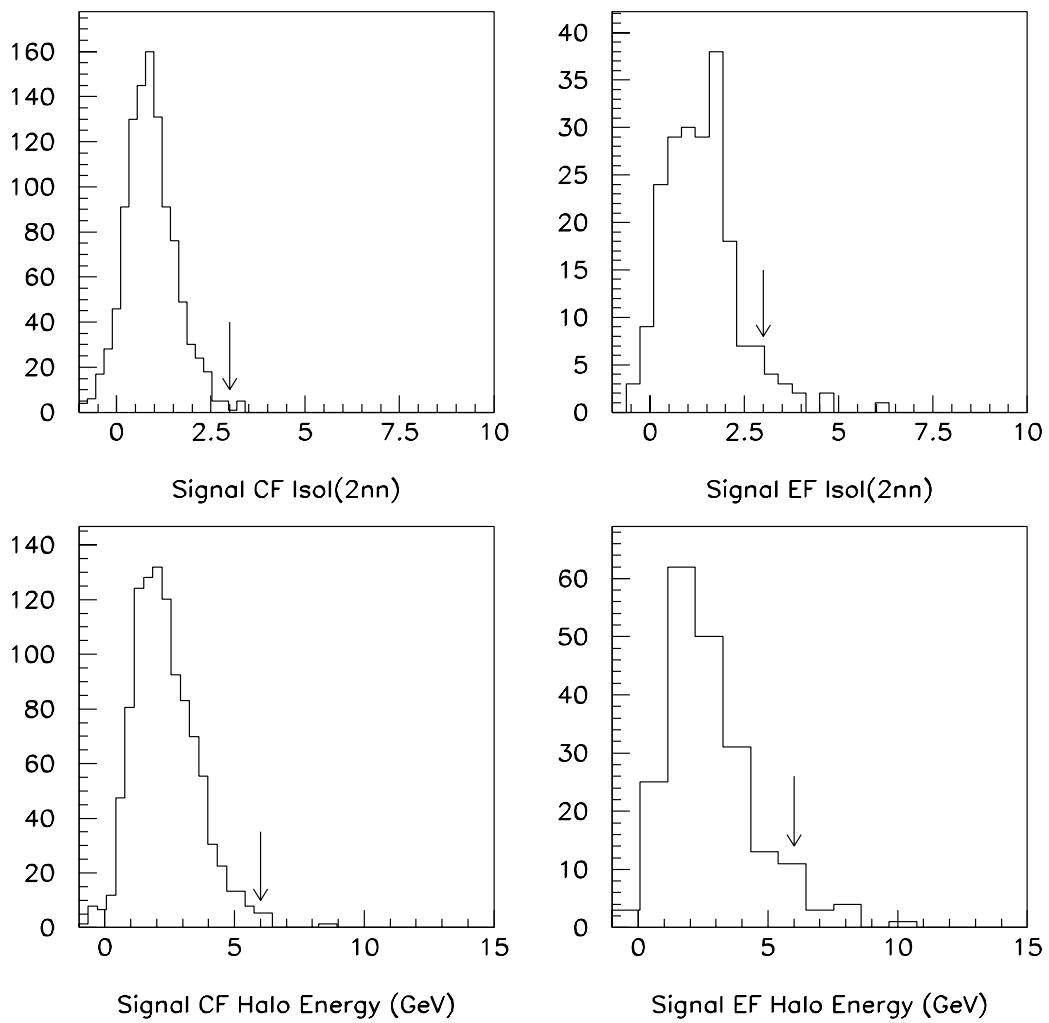

Figure 5.6: The two nearest neighbors isolation variable I_μ and the Halo Energy $E(0.6)-E(0.2)$ are plotted for CF and EF tracks. The arrows indicate the position of the quality cut used to define an isolated muon.

5.2 Candidate Samples Selection

5.2.1 Data set used

The analysis presented in this document is based on data recorded during the first running period of the DØ detector from April 1992 to May 1993. Runs corresponding to the very early period of data taking (April 1992 to November 1992) have been removed for the trigger definitions were still under development and therefore very unstable. In addition, bad runs with known hardware and/or software problems have been excluded for the efficiency estimations for such pathological situations are very difficult to estimate.

The integrated luminosity corresponding to this cleaned set of runs has been corrected for multiple interactions, Main Ring blanking, and for runs lost in the reconstruction process. The prescales that affected the $W \rightarrow \mu\nu$ and $Z \rightarrow \mu\mu$ triggers are calculated in section 6.1.2, resulting in an average factor of $\approx 88\%$. The prescales have not been included in the luminosities quoted for the cross section calculations, because they are considered as part of the trigger efficiencies.

Five different running periods are considered for this analysis, and the unprescaled integrated luminosity for each period is listed in table 5.2. The major changes that took place at these separations were:

1. The muon triggers were completely redefined in late December. The main difference was the combining of the CF and EF regions into a single trigger.

2. Major hardware changes occurred during the January shutdown. Approximately 1/3 of the muon electronics were affected. In addition, the detector was opened and closed, changing the geometry.

3. Level 2 (and offline) calibration and geometry constants were changed shortly after the shutdown. The new constants reflect the electronics changed during that period.

4. The Level 2 executable was changed, relaxing some quality cuts. This change took place in the last month of the run and affected mostly low p_T muon filters.

Table 5.2: Luminosities for each of the five running periods considered in the analysis. The major changes that occurred at these run boundaries are described in the text. The prescales are not included in the luminosities, for they will be considered as part of the trigger efficiencies; the average factor is included at the bottom of this table for completion only.

Running Period	Luminosity (pb^{-1})
Early Preshutdown	2.71 ± 0.33
Late Preshutdown	2.56 ± 0.31
Early Postshutdown	1.84 ± 0.22
Mid Postshutdown	5.63 ± 0.68
Late Postshutdown	0.68 ± 0.08
Total Run 1A	13.42 ± 1.61

Average Prescale	0.88
Run 1A (prescaled)	11.90 ± 1.43

5.2.2 Event Selection

The selection of $W \to \mu\nu$ and $Z \to \mu\mu$ events starts at trigger level by requiring at least one muon candidate within the WAMUS detector ($|\eta| \leq 1.7$) at Level 1, Level 1.5 and Level 2. The hardware triggers introduce an effective p_T^μ cut of ≈ 7 GeV; the Level 2 software trigger accepts muons with a cut on $p_T^\mu \geq 15$ GeV.

The same trigger requirement is applied to both the W and the Z selection to reduce systematics in the calculation of the ratio of the production cross sections. A more detailed description of the triggers is given in section 6.1.2.

The $W \rightarrow \mu\nu$ offline selection requires that:

- The event contains at least one tight muon[3].
- The MUCTAG [50] cut has been applied to reject muons with back–to–back muon tracks or hits. Furthermore, it has been extended to reject muons with back–to–back muon tracks in the EF region [51].
- Kinematic cuts $p_T^{\mu} \geq 20$ GeV and $p_T^{\nu} \geq 20$ GeV. The determination of p_T^{ν} has been described in section 3.4. For the $W \rightarrow \mu\nu$ selection only a maximum of two high p_T tight muons with $|\eta_{\mu}| \leq 1.7$ are considered for the muon correction of the $\not{E}_T$ determination.
- Removal of $Z \rightarrow \mu\mu$ events.

The $Z \rightarrow \mu\mu$ offline selection requires that:

- The event contains at least one tight and one loose muon.
- To reject cosmic background it is required that $\Delta\varphi \leq 170^o$ or $\Delta\theta \leq 170^o$ between both muons. To eliminate low mass dimuon pairs it is asked that $\Delta\varphi \geq 30$ degrees.
- Kinematic cuts $p_T^{\mu 1} \geq 20$ GeV and $p_T^{\mu 2} \geq 15$ GeV.

[3]The definitions for "tight" and "loose" muons correspond to the ones that have been presented in the previous section.

Chapter 6

Efficiencies and Backgrounds

In order to obtain the $W \to \mu\nu$ and $Z \to \mu\mu$ production cross sections, the total event selection efficiency and the remaining background contamination in the final candidate samples have to be calculated. The following sections of this chapter describe the methods used in this analysis to estimate those factors.

6.1 Selection Efficiencies

The following contributions to the total event selection efficiency correspond to the different selection cuts that have been defined in chapter 5.

6.1.1 "Loose" Muon Efficiency

The "loose" muon efficiencies are derived from a combination of data and Monte Carlo studies.

The geometric and kinematic acceptance and the efficiency of fiducial cuts applied to the samples are obtained from SHOWER LIBRARY Monte Carlo[1] $W \to \mu\nu$ and $Z \to \mu\mu$ events generated with ISAJET, run through MUSMEAR and reconstructed with the official DØRECO program used for collider data.

[1]For a description of the Monte Carlo generation of events, refer to chapter 4.

As was described in chapter 4, the MUSMEARed Monte Carlo has been corrected for resolution factors for Times and Delta Times, muon chamber alignment and efficiencies for Times, Delta Times and Pad Latches for each PDT. Each of these factors has been tuned comparing Monte Carlo distributions with collider data. Therefore, the loose muon efficiency estimated based on these Monte Carlo samples takes into account factors such as chamber efficiency, Main Ring effect and p_T smearing.

The systematic error of this Monte Carlo study is obtained from three sources:

1. The uncertainty in the chamber efficiencies used as input to the MUSMEAR package has been estimated by varying the efficiencies in $\pm 1\sigma$ and repeating the efficiency calculation. The resulting systematic error is $\approx 0.7\%$ in CF and $\approx 15\%$ in EF.

2. The uncertainty in the misalignment factor is estimated by varying this factor by ± 1 mm and repeating the efficiency calculation. This yields a systematic error of $\approx 1\%$ in CF and $\approx 1.5\%$ in EF.

3. The contribution to the systematic error estimated when using different[2] structure functions is $\approx 2\%$.

The systematic error in the EF region is much bigger than in the CF, and is clearly dominated by the determination of the chamber efficiencies.

The muon reconstruction efficiency has been estimated directly from data [52]. Unbiased events from a mark and pass run[3] have been selected by requiring that

[2]The sets used for the systematic study were CTEQ2M, CTEQ2MS, DFLM260, BMA, GRVH0, MRSD0D, MRSDMD and MRSS0D.

[3]In a mark and pass run, the trigger decisions are stored in the event but all events are written to tape, independently of having satisfied a trigger or not.

a muon Level 1 trigger is in the same $\eta\varphi$ region as an offline reconstructed jet, and further categorized as a "good" or "bad" muon track by scanning. To reduce the systematic error of this method, the scanning was performed by at least two different persons. The offline reconstruction efficiency for "good" tracks that had passed a muon Level 2 filter was estimated to be $95 \pm 3\%$ for CF and $95 \pm 3\%$ for EF tracks. This efficiency is not properly simulated by the Monte Carlo, where all tracks that satisfy a muon Level 2 filter are reconstructed offline. For these reasons, the muon offline reconstruction efficiency is taken directly from data.

In addition, the efficiency for the calorimeter confirmation cut is also obtained directly from data, for the underlying event is not properly simulated in the Monte Carlo samples, resulting in a lower energy muon trace in the calorimeter. The method used is the same as for the tight muon efficiencies, and is described in section 6.1.3.

The loose muon efficiencies, including the efficiencies of the fiducial and kinematic cuts, are summarized in tables 6.1 and 6.2 for the $W \to \mu\nu$ and the $Z \to \mu\mu$ selections respectively.

Table 6.1: Loose muon efficiency for the $W \rightarrow \mu\nu$ selection. The first error in the total acceptance calculation is statistical, the second is systematic.

Loose Muon Eff(%)	CF	EF
Eta Coverage	51.6 ± 0.7	24.9 ± 0.5
Geometrical Acceptance	76.9 ± 1.2	63.1 ± 1.6
$\int Bdl$	84.1 ± 1.5	95.6 ± 2.5
Kinematic Cuts	75.2 ± 1.5	71.1 ± 2.2
Total Acceptance	25.1 ± 0.5 ± 0.6	10.6 ± 0.3 ± 1.6
Muon Reconstruction	95 ± 3	95 ± 3
Calorimeter Confirmation	100 ± 1	100 ± 1
Total Loose	23.9 ± 1.0	10.1 ± 1.6

Table 6.2: Loose muon efficiencies for the $Z \rightarrow \mu\mu$ selection. The first error in the total acceptance calculation is statistical, the second is systematic.

Loose Muon Eff(%)	CF CF	CF EF	EF EF
Eta Coverage	23.1 ± 0.5	24.6 ± 0.5	6.3 ± 0.3
Geometrical Acceptance	57.9 ± 1.6	50.0 ± 1.4	41.6 ± 2.6
$\int Bdl$	70.5 ± 2.3	80.8 ± 2.6	92.8 ± 5.9
Kinematic Cuts	88.3 ± 3.1	85.9 ± 2.9	80.3 ± 5.7
Track angle cut	80.1 ± 3.1	100.0 ± 0.1	82.7 ± 6.5
Total Acceptance	6.7 ± 0.2 ± 0.3	8.5 ± 0.3 ± 0.9	1.6 ± 0.1 ± 0.4
Muon Reconstruction	90 ± 7	90 ± 5	90 ± 6
Calorimeter Confirmation	100 ± 1	100 ± 1	100 ± 2
Total Loose	6.0 ± 0.6	7.7 ± 1.0	1.5 ± 0.4

6.1.2 Trigger Efficiency

The trigger efficiencies have been estimated directly from data since they are difficult to simulate properly in the Monte Carlo. Although the Level 1 and 1.5 efficiencies obtained from data agree quite well with the ones predicted by the trigger simulator when run on MUSMEARed Monte Carlo, the Level 2 efficiency differs by $\approx$ 10 to 40 %, as is shown Appendix A. An additional complication is that the trigger simulator corresponding to the preshutdown period is not available.

The data sample used to estimate trigger efficiencies was selected with the following set of cuts:

1. The event passed a non–muon Level 2 trigger. This condition assures that the sample is unbiased for muon trigger studies. In addition, the microblank veto was applied to reject events where the Main Ring beam was present at DØ . This condition is required during normal data taking for the triggers used in the $W/Z \rightarrow \mu$ analysis.

2. The event contains at least one offline reconstructed muon with $p_T \geq 20$ GeV.

3. The muon track satisfies tight offline selection cuts: $\chi^2 \leq 50$, $|t_0^f| \leq 80$ ns, $Cal(1nn) \geq 1.5$ GeV, muon–CD track match.

The results were cross–checked with the ones obtained from the $Z \rightarrow \mu\mu$ sample where one of the muons triggered and the second muon is unbiased for the trigger studies.

Two different trigger configurations were used to select $W/Z \rightarrow \mu$ events during DØ run 1A. The change took place in late December, separating the running period

referred to as early preshutdown in section 5.2.1 from the rest of the run. For the first running period, two Level 1 $\times$ Level 1.5 triggers, and three Level 2 filters were used to collect $W \rightarrow \mu\nu$ and $Z \rightarrow \mu\mu$ candidates. Trigger MU_1_HIGH accepted events where one muon track was found within $|\eta_\mu| \leq 1.7$ at Level 1 and Level 1.5. The Level 2 requirement for MU_HIGH was a muon track with $p_T^\mu \geq 15$ GeV, $IFW4 \leq 1$, $|\eta_\mu| \leq 1.7$, and cosmic rejection cut given by MUCTAG [50]. This trigger combination was prescaled both at Level 1 and at Level 2.

In addition, trigger MU_1_CENT accepted events where one muon track was found within $|\eta_\mu| \leq 1.0$ at Level 1 and Level 1.5. Two Level 2 filters, differing only in the cut applied to the muon flag word $IFW4$, were applied to events selected by this trigger requirements: both filters passed events containing a muon track with $p_T^\mu \geq 15$ GeV, $|\eta_\mu| \leq 1.0$, and MUCTAG cosmic rejection cut; MU_CENT required $IFW4 \leq 1$, and MU_MAX accepted only events with $IFW4 = 0$. Although the triggers were prescaled at Level 1, only MU_CENT suffered a Level 2 prescale.

The second trigger configuration, used in the rest of the run, included two Level 1 $\times$ Level 1.5 triggers (MU_1_HIGH and MU_1_MAX) and two corresponding Level 2 filters (MU_HIGH and MU_MAX). They both selected muons found within $|\eta_\mu| \leq 1.7$ at the three trigger levels, $p_T^\mu \geq 15$ GeV and MUCTAG cosmic rejection at Level 2, and differed only in the accepted value for $IFW4$ at Level 2: MU_HIGH passed tracks with $IFW4 \leq 1$, while MU_MAX had the tighter requirement of $IFW4 = 0$. Both combinations were prescaled at Level 1, but only MU_HIGH suffered an effective Level 2 prescale.

Furthermore, a new tool was introduced during the shutdown for specific triggers requiring a Level 1.5 confirmation. During the preshutdown, an event failing Level 1.5, but passing another Level 1 trigger that did not require Level 1.5,

would reach the Level 2 filter and possibly be selected. The new tool assures that Level 2 filters corresponding to triggers that require Level 1.5 actually check that Level 1.5 was set to test the event. This feature has been reproduced offline for preshutdown data for the $W/Z \rightarrow \mu$ analysis.

In addition to these two trigger configurations, three different Level 2 executables were used during the postshutdown (see table 5.2). Studies performed both with the Trigger Simulator and on unbiased data show that the Level 2 efficiency does not change significantly among these different executables for high p_T single muon triggers. The three postshutdown running periods are thus combined into one.

The different components of the total trigger efficiency are the Level 1 $\times$ Level 1.5 efficiency (ϵ_{L1}), the Level 1 prescale ($L1ps$), the Level 2 efficiency (ϵ_{L2}), and the Level 2 prescale ($L2ps$). The first two components are measured from the unbiased data sample selected as described earlier in this section; the last two are obtained from a combination of this data and the $W \rightarrow \mu\nu$ sample itself.

The ϵ_{L1} is measured by counting the number of events that satisfy a Level 1.5 OTC requirement compared to the total number of events in the unbiased sample. The $L1ps$ is obtained from the number of those events that also fired at least one of the $W/Z \rightarrow \mu$ triggers at Level 1. The events that in addition fired a $W/Z \rightarrow \mu$ filter at Level 2, give $\epsilon_{L2} * L2ps$.

The trigger efficiency for the $W \rightarrow \mu\nu$ cross–section calculation can be obtained very easily from these numbers for only one muon is present in the event, by doing:

$$\epsilon_{Trig}(W) = \epsilon_{L1} * L1ps * \epsilon_{L2} * L2ps.$$

For the $Z \rightarrow \mu\mu$ analysis the trigger efficiencies apply to either muon, but the

prescales apply to each event; for this reason it is necessary to separate the ϵ_{L2} from the $L2ps$.

The $W \rightarrow \mu\nu$ sample is used to calculate the Level 2 prescale independently. The $L2ps$ is a combination of prescale to the looser filter MU_HIGH and a ratio of "HIGH" to "MAX" efficiency. These two factors are obtained from the $W \rightarrow \mu\nu$ sample. Since MU_MAX implies MU_HIGH (except for the prescale), the prescale factor can be calculated by looking at events which satisfy "MAX" and seeing how many of those also satisfy "HIGH". Since MU_MAX is a subset of MU_HIGH, the "HIGH" to "MAX" efficiency factor can be measured by looking at events which satisfy "HIGH" and seeing how many of them also satisfy "MAX". The results for the loose Level 2 prescale ($LOps$) and the "HIGH" to "MAX" ratio (m/h) are summarized in table 6.3.

There is an additional complication because during the earliest running period, the CF and EF L1 triggers were on different bits. This introduces an additional prescale factor in the EF only ($EFps$), that is also included in table 6.3. The overall Level 2 prescale factor can be obtained by doing:

$$L2ps = (LOps + m/h - LOps * m/h) * EFps$$

where the values for $LOps$ are common to CF and EF, but the m/h ratio varies with the geometric region.

As was said earlier, in the calculation of the trigger efficiency for the $Z \rightarrow \mu\mu$ analysis the prescales apply to each event, although the trigger efficiencies apply to either muon.

Furthermore, as two muons are involved, it can occur that the same muon fires the three trigger levels, or that a different muon triggered at Level 1 $\times$ Level 1.5 than the one that fired Level 2. The Level 2 filter looks for muon candidates in

Table 6.3: Prescale factors and ratios of efficiencies for "HIGH" and "MAX" filters.

Running Period	Loose Ps	CF m/h	EF m/h	EF Prescale
Early Pre	.74	.97	0	.73
Late Pre	.49	.94	.83	1
Early Post	.56	.93	.88	1
Mid Post	.36	.90	.62	1
Late Post	.25	.91	.50	1

the complete CF region, independent of the Level 1 trigger; but it only unpacks muon hits in roads around the position where a Level 1 trigger was found in the EF. The second triggering option can thus only take place for $Z \rightarrow \mu\mu$ events where both muons are located in the CF.

The trigger efficiency for the $Z \rightarrow \mu\mu$ study is therefore obtained from the single muon triggers by requiring that either muon passes Level 1 $\times$ Level 1.5 and either muon passes Level 2, only for the CFCF sample. For the CFEF and EFEF regions, either muon has to pass all the trigger levels by itself.

$$\epsilon_{Trig}^{CFCF}(Z) = [\epsilon_{L1} * (2 - \epsilon_{L1})] * [\epsilon_{L2} * (2 - \epsilon_{L2})] * L1ps * L2ps$$

$$\epsilon_{Trig}^{EFEF}(Z) = [\epsilon_{L1} * \epsilon_{L2} * (2 - \epsilon_{L1} * \epsilon_{L2})] * L1ps * L2ps$$

$$\epsilon_{Trig}^{CFEF}(Z) = \left[\epsilon_{L1}^{CF} * \epsilon_{L2}^{CF} + \epsilon_{L1}^{EF} * \epsilon_{L2}^{EF} - \epsilon_{L1}^{CF} * \epsilon_{L2}^{CF} * \epsilon_{L1}^{EF} * \epsilon_{L2}^{EF})\right] * L1ps * L2ps$$

Based on these studies, the trigger efficiency could not be determined for the EF preshutdown region. This is a consequence of the very limited statistics available both in the unbiased sample and in the $Z \rightarrow \mu\mu$ sample for this particular region and the fact that the efficiencies estimated from these two samples do not

agree with each other. In addition, no trigger simulator is available to represent the trigger configuration existing at this early period. As the amount of data available for this period is very limited[4], the preshutdown EF has been excluded from the cross section calculations.

The results for the single muon trigger efficiencies and prescales are summarized in table 6.4; they are broken up into different geometrical regions and trigger configurations. The total results can be obtained combining the different running periods weighted by their luminosities.

Table 6.4: Single muon trigger efficiencies, corresponding to the triggers used in the $W/Z \rightarrow \mu$ cross section calculation. The efficiencies correspond to muon tracks that have been reconstructed offline. The preshutdown EF data have been excluded, for the trigger efficiency is not known for that period.

Running Period	Preshutdown		Postshutdown	
Geometric Region	CF	EF	CF	EF
Level 1 $\times 1.5$ (%)	43 ± 4	??	52 ± 2	14 ± 3
Level 1 prescale	0.97	??	0.90	1.0
Level 2 (%)	72 ± 5	??	88 ± 3	86 ± 9
Level 2 prescale	0.98	0.72	0.94	0.94

6.1.3 "Tight" Muon Efficiency

The "tight" muon efficiencies are derived directly from data. A background free, unbiased sample of isolated high p_T muons should be used in the ideal case to measure the efficiencies properly. A good approximation to such a sample is given by the $Z \rightarrow \mu\mu$ events selected with the requirement that at least one of the muons pass all the quality cuts, and the other muon all but the cut in question.

[4]See table 7.1 in section 7.1 for the number of events for each region.

This allows for the determination of the individual efficiencies for each quality cut when applied last.

The combined efficiency for the entire set of cuts is obtained applying them all together to a $Z \rightarrow \mu\mu$ sample selected with the requirement that at least one of the muons pass all the quality cuts, with no other condition on the second muon besides of being constrained to the geometrical region considered in this analysis. The kinematic cuts on this sample have been raised to 20 GeV for each muon in order to minimize the background. The efficiency obtained by this method is different from the product of the individual efficiencies because of correlations and anticorrelations among the cuts. As a consistency check, the combined efficiency was obtained for the two different running periods separated by the accelerator shutdown when several hardware changes were performed on the detector; the efficiency was found to be independent of these changes.

Table 6.5 summarizes the efficiency for each cut when applied last. The final line in that table gives the combined efficiency for all cuts applied together. Each value has been estimated for CF and EF tracks separately. Note that the CD Matching corresponds to the tighter $\Delta\varphi$ and $\Delta\theta$ values used in this analysis, and that the efficiency for Isolation combines the I_μ and the Halo Energy Cut. The efficiencies for the bend and non–bend view impact parameters are also combined into a single value.

Table 6.5: Tight single muon efficiencies.

Tight Muon Eff(%)	CF	EF
Global Fitting	100 ± 1	82 ± 8
CD Matching	82 ± 4	92 ± 5
Impact Parameters	95 ± 2	95 ± 5
Floating time	94 ± 3	90 ± 7
Isolation	85 ± 4	86 ± 8
Product of Tight	62 ± 7	55 ± 15
Total Tight	63 ± 5	43 ± 8

6.2 Background Estimates

The background estimates were done from a combination of data and Monte Carlo studies. The results are summarized in table 6.6.

6.2.1 Cosmic Background

The cosmic background was estimated from floating t_0 studies following the technique described in reference [47]. The t_0^f distribution for the prompt signal was obtained from a sample of muons with $p_T^\mu > 5$ GeV and very tight quality cuts: CD match, $\chi^2 < 20$, $E(0.2) > 5$ GeV, $b_{nonbend} < 20$ cm. A cosmic/combinatoric junk sample was selected with a complementary set of cuts: $E(0.2) < 0.5$ GeV, no CD match, $b_{nonbend} > 40$ cm. The distribution for the candidate sample was given by a $W \rightarrow \mu\nu$ sample selected applying all the quality cuts except the floating time cut. The background fraction was determined by fitting the candidate sample to a linear sum of the signal and background t_0^f distributions. The fitting was performed separately in the CF and EF regions. The resulting fit is shown in figure 6.1 for the CF region.

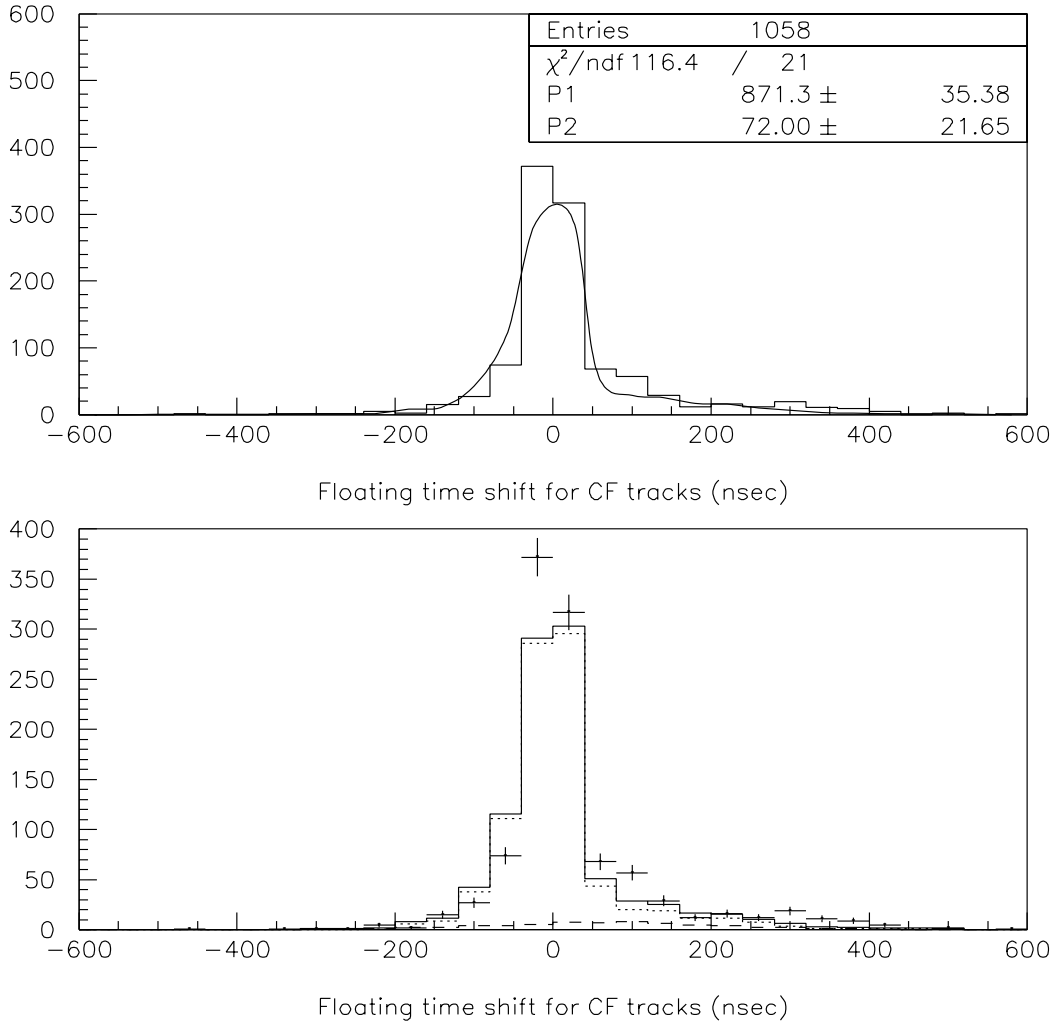

Figure 6.1: The t_0^f distribution for the candidate sample is fitted to a linear sum of the signal and background shape(top). The dotted line corresponds to the clean sample, the dashed line to the cosmic/combinatoric tracks and the solid histogram to their linear sum. The candidate sample shape is given by the data points (bottom).

The final $W \to \mu\nu$ selection requires that the muon track is on time with the beam crossing, by asking that $t_0^f \leq 100$ ns. The efficiency of this cut for prompt muons and for cosmic/combinatoric tracks is obtained from the respective samples described above, resulting in $91.9 \pm 0.6\%(82.0 \pm 2.4\%)$ for CF(EF) for prompt muons and $59.0 \pm 1.0\%(47.0 \pm 4.7\%)$ for CF(EF) cosmic/combinatoric tracks. The remaining cosmic/combinatoric contamination in the final $W \to \mu\nu$ sample is therefore estimated in $3.8 \pm 1.6\%$ in the CF and $7.0 \pm 5.4\%$ in the EF region.

For the $Z \to \mu\mu$ sample, the background was estimated using the same procedure. The distribution for the candidate sample was given by a $Z \to \mu\mu$ sample selected applying all the selection cuts except the floating time cut. The final $Z \to \mu\mu$ selection requires that at least one of the muons in the event passes the $t_0^f \leq 100$ ns cut. The efficiency of this cut for prompt muons and for cosmic/combinatoric tracks is taken from the ones used for the $W \to \mu\nu$ study, properly weighted by the number of CF and EF tracks in the candidate sample. The cosmic/combinatoric background in the final $Z \to \mu\mu$ sample is therefore estimated in $5.1 \pm 3.6\%$.

6.2.2 QCD Background

The QCD background originating from prompt muons was obtained using a method similar to the one used for the cosmic/combinatoric background estimation. In this case the halo energy in an $\eta\varphi$ cone of 0.6 around the muon minus that in a cone of 0.2 was used to fit the background fraction.

The background shape was obtained from a sample of muons passing all the quality cuts except the isolation cuts, and with $10 < p_T^\mu < 15$ GeV. The signal

shape was taken from a subset of the $W \rightarrow \mu\nu$ candidate sample with no jets in the opposite half of the detector (in φ) with respect to the muon. The distribution for the candidate sample was given by a $W \rightarrow \mu\nu$ sample selected applying all the quality cuts except the isolation cuts.

The background fraction was determined by fitting the candidate sample to a linear sum of the signal and background halo distributions. The fitting was performed separately in the CF and EF regions. The resulting fit is shown in figure 6.2 for the CF region.

The final $W \rightarrow \mu\nu$ selection requires that the muon track is isolated, by applying cuts on the muon isolation variable I_μ and on the halo energy $E(0.6) - E(0.2)$ The efficiency of these cuts applied together on isolated muons and on muons originating from QCD processes is obtained from the respective samples described above, resulting in $90.6 \pm 1.2\%(76.5 \pm 5.1\%)$ for CF(EF) for isolated muons and $13.8 \pm 1.0\%(7.3 \pm 2.0\%)$ for CF(EF) for non–isolated muons. The remaining QCD contamination in the final $W \rightarrow \mu\nu$ sample is therefore estimated in $5.1 \pm 0.8\%$ in the CF and $5.3 \pm 2.5\%$ in the EF region.

For the $Z \rightarrow \mu\mu$ sample, the background was estimated using the same procedure. The distribution for the candidate sample was given by a $Z \rightarrow \mu\mu$ sample selected applying all the selection cuts except the isolation cuts. The final $Z \rightarrow \mu\mu$ selection requires that at least one of the muons in the event passes the isolation cuts $I_\mu \leq 3\sigma$ and $E(0.6) - E(0.2) \leq 6$ GeV. The efficiency of these cuts on isolated and non–isolated muons is taken from the ones used for the $W \rightarrow \mu\nu$ study, properly weighted by the number of CF and EF tracks in the candidate sample. The remaining QCD background in the final $Z \rightarrow \mu\mu$ sample is thus estimated as $2.6 \pm 0.8\%$.

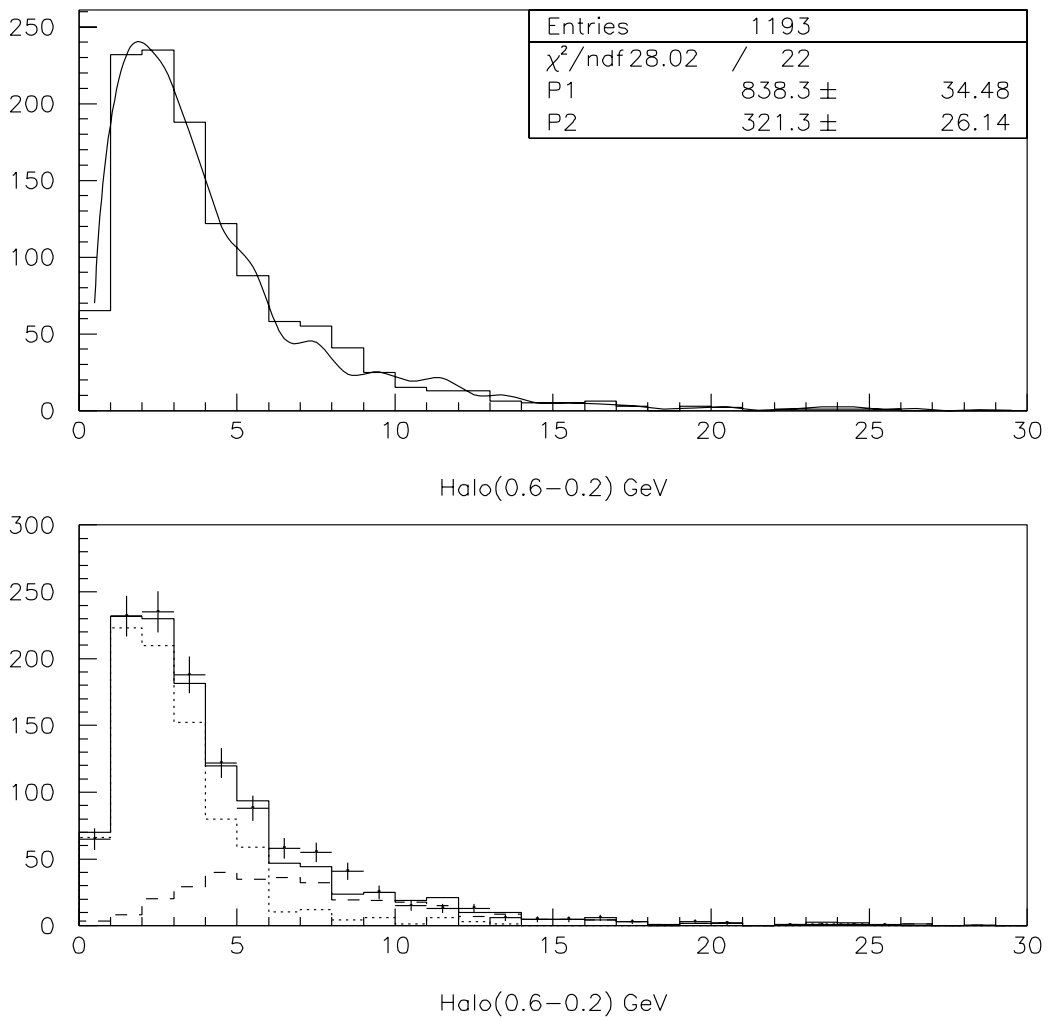

Figure 6.2: The $E(0.6) - E(0.2)$ distribution for the candidate sample is fitted to a linear sum of the signal and background shape(top). The dotted line corresponds to isolated tracks, the dashed line to muons originating from QCD processes and the solid histogram to their linear sum. The candidate sample shape is given by the data points (bottom).

The QCD background originating from punchthrough and π/K decays produces muons with an estimated rate of $\approx$ 10 times smaller than the rate from b decays for $p_T^\mu > 12$ GeV [53]. The rate from punchthrough is expected to be yet another order of magnitude lower [48]. The reason for the low rate is the thickness of the calorimeter + iron system at DØ, combined with the fact that the momentum measurement is made after most of the material. The background contamination from these sources in the $W \to \mu\nu$ and $Z \to \mu\mu$ samples is therefore considered negligible.

6.2.3 Physics Backgrounds

The Physics backgrounds to the $W \to \mu\nu$ and $Z \to \mu\mu$ samples have been estimated by running the selection code on Monte Carlo signal and background samples, normalizing the number of selected events to the size of the input samples, and correcting for the respective branching ratios. The different contributions are estimated as follows:

1. Running the $W \to \mu\nu$ selection code on Monte Carlo $Z \to \mu\mu$ events produces a sample that contains two kinds of events: dimuon events that also pass the $Z \to \mu\mu$ selection and can therefore be removed from the final $W \to \mu\nu$ sample ("removable" dimuon background) and events where one of the two muons has not been reconstructed ("one–legged" $Z \to \mu\mu$ background). The first kind of events can be removed from the $W \to \mu\nu$ sample by rejecting events that also pass the $Z \to \mu\mu$ selection; the second kind can not be distinguished from the $W \to \mu\nu$ events themselves.

   The estimated background for the first type of events as obtained from the Monte Carlo study is $3.5 \pm 0.3\%$. The amount of "two–legged" dimuons re-

moved from the actual $W \rightarrow \mu\nu$ data sample, was $3.5 \pm 0.4\%$; this agreement adds confidence to the Monte Carlo estimations for the other physics backgrounds. The remaining "one–legged" $Z \rightarrow \mu\mu$ background to the $W \rightarrow \mu\nu$ sample is estimated as $6.5 \pm 0.5\%$ for the CF and $7.0 \pm 1.0\%$ for the EF region.

2. An event where $W \rightarrow \tau\nu$ is followed by $\tau \rightarrow \mu\nu\nu$ cannot be distinguished on an event-by-event basis from the direct $W \rightarrow \mu\nu$ decays. The rate of the τ mode is suppressed by the branching ratio for $\tau \rightarrow \mu\nu\nu$ ($\approx 17\%$) and the acceptance is reduced because the muons from the τ cascade have a much softer p_T spectrum than the muons from the direct decays. Due to the difference in the p_T^μ spectrum between the two decay modes, the background has been estimated using Monte Carlo samples that had been run through MUSMEAR. The background resulting from this source has been estimated to be $5.9 \pm 0.5\%$ for CF and $5.7 \pm 0.9\%$ for EF.

3. As in the previous item, a Monte Carlo sample was used to calculate the $Z \rightarrow \tau\tau \rightarrow \mu\mu$ background resulting in $0.8 \pm 0.2\%(1.3 \pm 0.4\%)$ in CF(EF) for the $W \rightarrow \mu\nu$ and $0.7 \pm 0.2\%$ for all eta regions in the $Z \rightarrow \mu\mu$ sample.

4. The Drell–Yan background to the $W \rightarrow \mu\nu$ and $Z \rightarrow \mu\mu$ samples was estimated from a Monte Carlo Drell–Yan to dimuon sample, resulting in $1.7 \pm 0.3\%$ for all eta regions in the $Z \rightarrow \mu\mu$ sample. The estimated background from this source in the $W \rightarrow \mu\nu$ sample is $< 0.1\%$ and is therefore considered negligible.

Table 6.6: Background Summary to $W \to \mu\nu$ and $Z \to \mu\mu$ samples.

	$W \to \mu\nu$		$Z \to \mu\mu$
Backgrounds (%)	CF	EF	all
Cosmic–Combinatoric	3.8 ± 1.6	7.0 ± 5.4	5.1 ± 3.6
QCD	5.1 ± 0.8	5.3 ± 2.5	2.6 ± 0.8
One-legged $Z \to \mu\mu$	6.5 ± 0.5	7.0 ± 1.0	—
$W \to \tau \to \mu$	5.9 ± 0.5	5.7 ± 0.9	—
$Z \to \tau\tau \to \mu(\mu)$	0.8 ± 0.2	1.3 ± 0.4	0.7 ± 0.2
Drell–Yan	—	—	1.7 ± 0.3
Total	22.1 ± 1.9	26.3 ± 6.1	10.1 ± 3.7

Chapter 7

Cross Sections

The event selections described in chapter 5 are applied to data recorded during DØ's run 1A to obtain the $W \rightarrow \mu\nu$ and $Z \rightarrow \mu\mu$ candidate samples. The number of events in those samples and their selection efficiencies and background contaminations estimated in chapter 6 are combined to calculate the $W \rightarrow \mu\nu$ and $Z \rightarrow \mu\mu$ production cross sections.

7.1 $W \rightarrow \mu\nu$ and $Z \rightarrow \mu\mu$ candidate samples

1799 $W \rightarrow \mu\nu$ and 119 $Z \rightarrow \mu\mu$ candidates are selected applying the cuts presented in chapter 5. Table 7.1 shows their distribution for each running period and for each geographic region.

Figures 7.1 to 7.4 show different distributions for these samples.

Table 7.1: Number of events in the $W \rightarrow \mu\nu$ and $Z \rightarrow \mu\mu$ candidate samples for each running period and geographic region.

	$W \rightarrow \mu\nu$		$Z \rightarrow \mu\mu$		
Running Period	CF	EF	CF-CF	CF-EF	EF-EF
Early Preshutdown	304	24	21	9	0
Late Preshutdown	273	29	15	10	0
Early Postshutdown	208	18	12	3	0
Mid Postshutdown	800	50	26	16	3
Late Postshutdown	80	13	3	1	0
Total per region	1665	134	77	39	3
Total samples	1799		119		

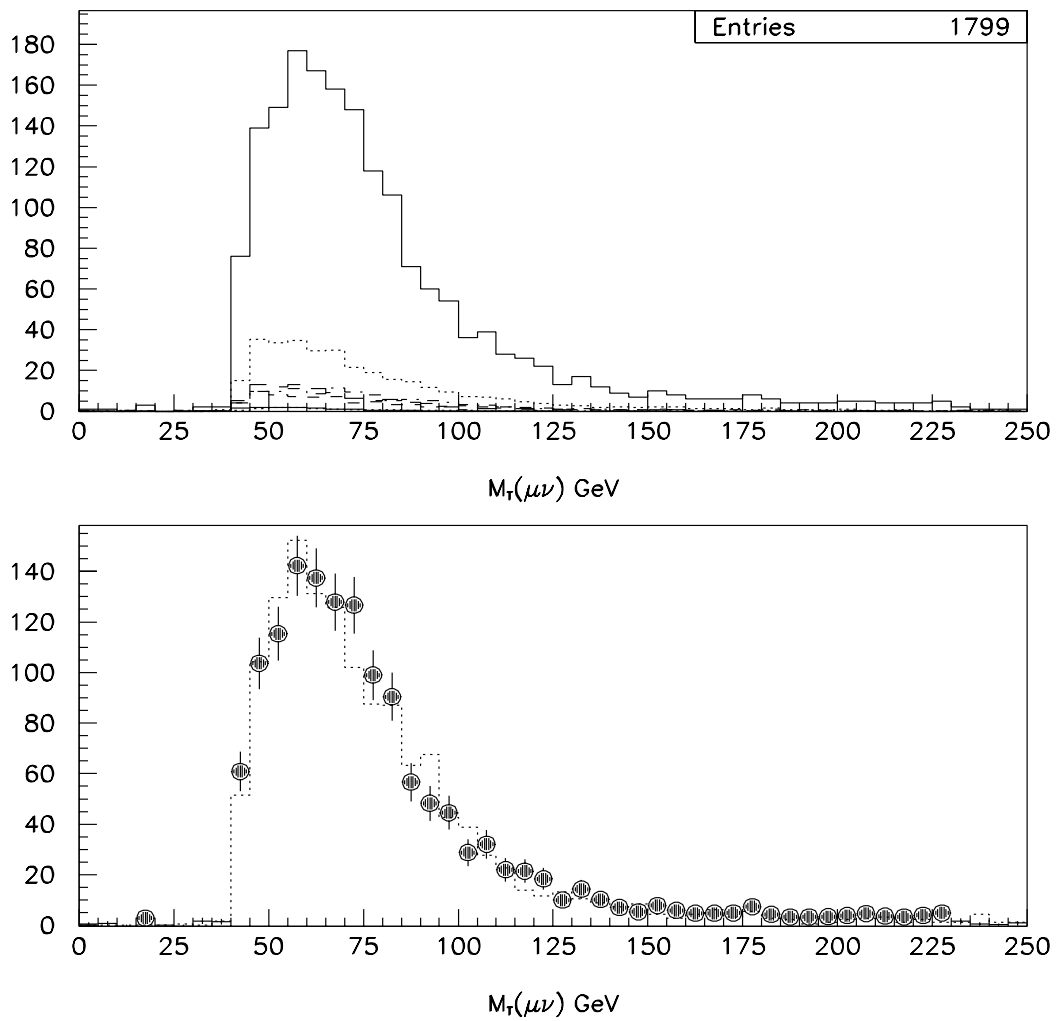

Figure 7.1: Top: The $\mu - \nu$ transverse mass is plotted for the $W \to \mu\nu$ sample in full line and for the combined backgrounds in dotted line. Bottom: the same distribution is shown for the $W \to \mu\nu$ sample after background subtraction and compared to a smeared Monte Carlo. The sample is given by the data points, and the histogram is the Monte Carlo prediction.

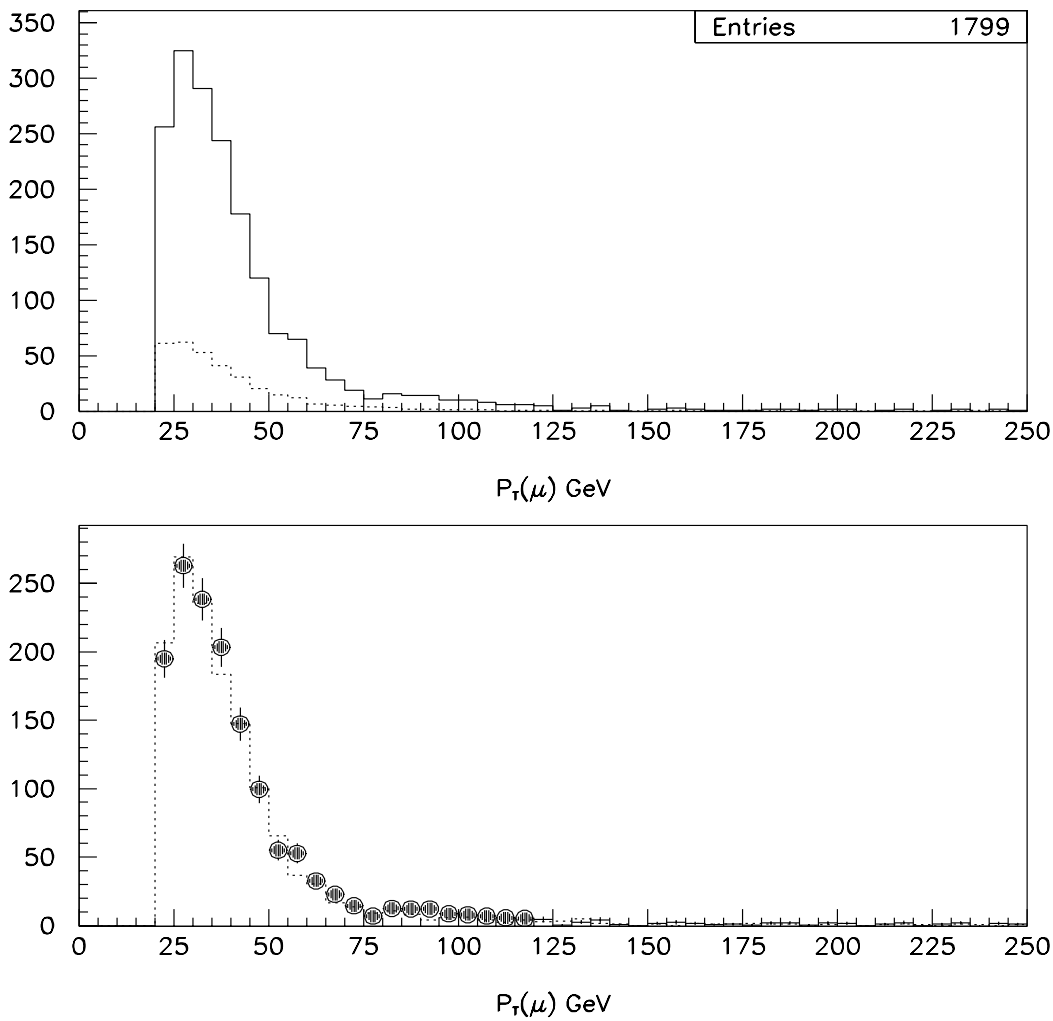

Figure 7.2: Top: The p_T^μ distribution is plotted for the $W \to \mu\nu$ sample in full line and for the combined backgrounds in dotted line. Bottom: the same distribution is shown for the $W \to \mu\nu$ sample after background subtraction and compared to a smeared Monte Carlo. The sample is given by the data points, and the histogram is the Monte Carlo prediction.

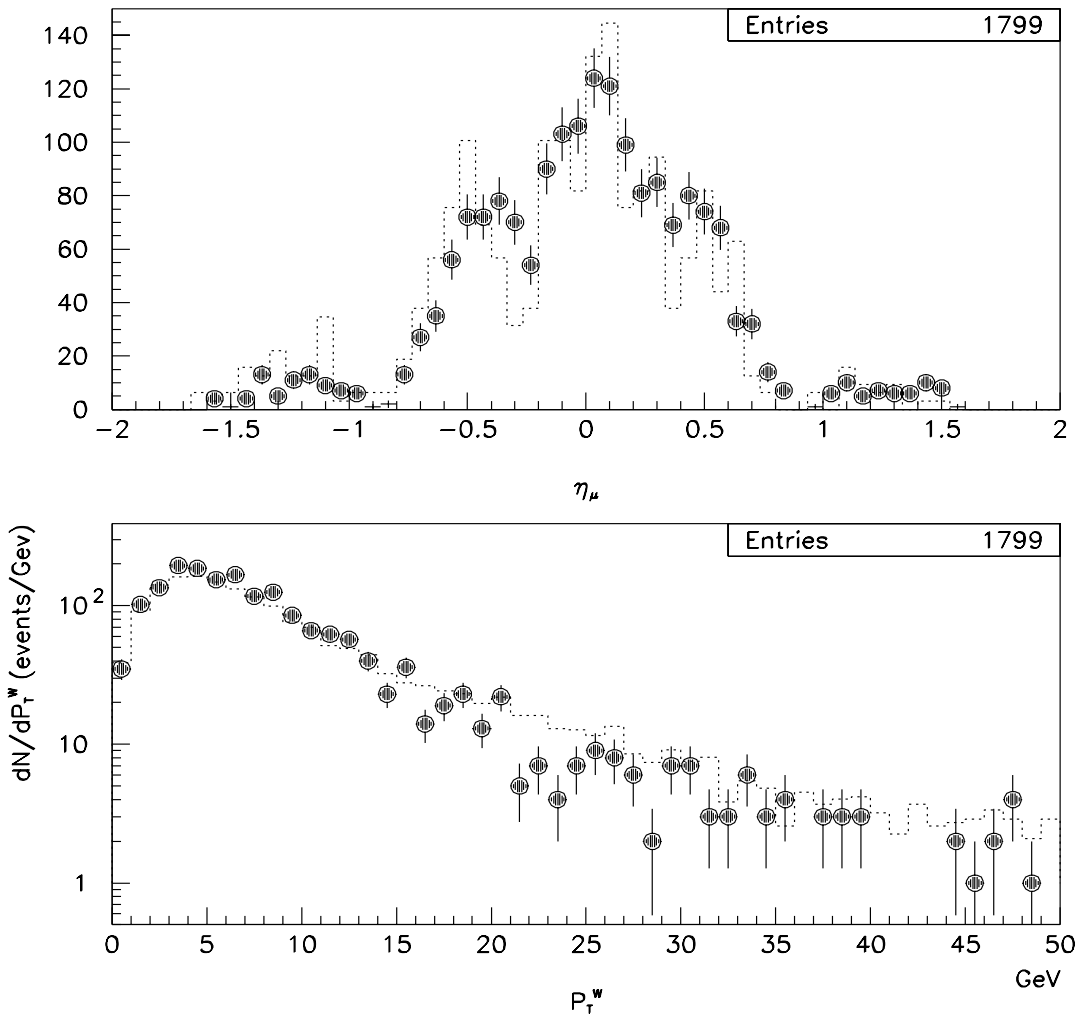

Figure 7.3: Top: The η_μ distribution is plotted for the $W \to \mu\nu$ sample (dots) and for a smeared Monte Carlo that has been run through the trigger simulator (histogram). Bottom: The W p_T distribution is plotted for the $W \to \mu\nu$ sample (dots) and compared to the same distribution for the $W \to e\nu$ sample in dotted line.

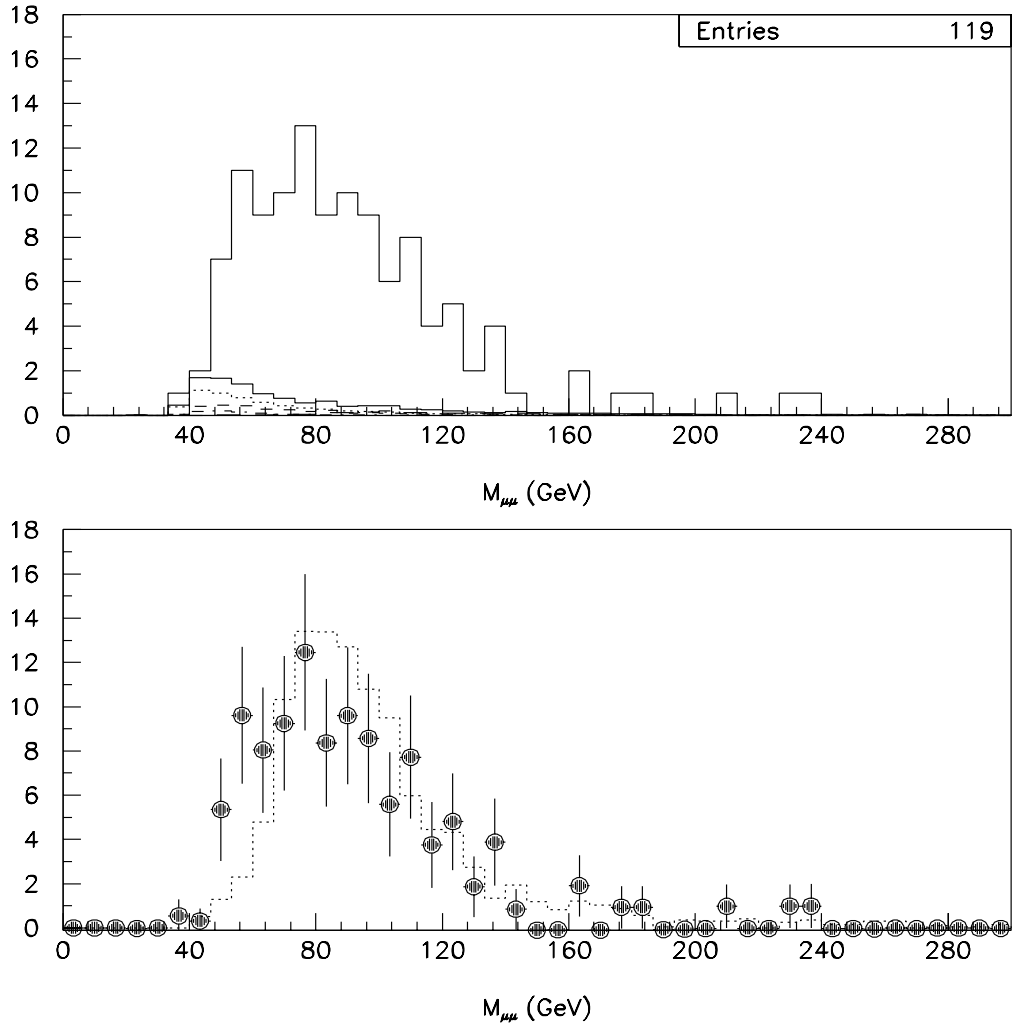

Figure 7.4: Top: The dimuon invariant mass is plotted for the $Z \to \mu\mu$ sample in full line and for the combined backgrounds in dotted line. Bottom: the same distribution is shown for the $Z \to \mu\mu$ sample after background subtraction and compared to a smeared Monte Carlo. The sample is given by the data points, and the histogram is the Monte Carlo prediction.

7.2 Cross Section Measurements

The product of the production cross sections of W and Z bosons times their branching ratios into muons can be computed according to the formulas

$$\sigma_W^\mu \equiv \sigma(\overline{p}p \to W + X)BR(W \to \mu\nu) = \frac{\sum(N_W - N_B)}{\sum(\varepsilon_W A_W L_W)}$$

$$\sigma_Z^\mu \equiv \sigma(\overline{p}p \to Z + X)BR(Z \to \mu^+\mu^-) = \frac{\sum(N_Z - N_B)}{\sum(\varepsilon_Z A_Z L_Z)}$$

where N_W (N_Z) is the number of W (Z) candidates observed, N_B is the estimated number of background events to the sample, ε is the total efficiency for detecting the signal events, A is the geometrical acceptance of the detector and L is the integrated luminosity corresponding to the considered samples. The sum is performed over the different running periods and geometrical regions.

As has been stated in section 6.1.2, the EF preshutdown trigger efficiencies can not be determined and the corresponding data is therefore excluded from the cross section calculations. Furthermore, the inclusion of the EF postshutdown data in the calculations results in an increase in the combined error (statistical + systematic) compared to the CF only results. The major source of this degradation has been shown in section 6.1.1 to be the EF chamber efficiencies used as input to the MUSMEAR package.

For these reasons, the cross section calculations have been restricted to the CF region only yielding:

$$\sigma B(W \to \mu\nu) = 1.86 \pm 0.06(stat) \pm 0.19(sys) \pm 0.22(lum) \text{ nb},$$

$$\sigma B(Z \to \mu\mu) = 0.155 \pm 0.020(stat) \pm 0.016(sys) \pm 0.019(lum) \text{ nb}.$$

These values are compared with the theoretical predictions [54] as well as other experimental results [55] in figure 7.5. The two curves are the extremes obtained

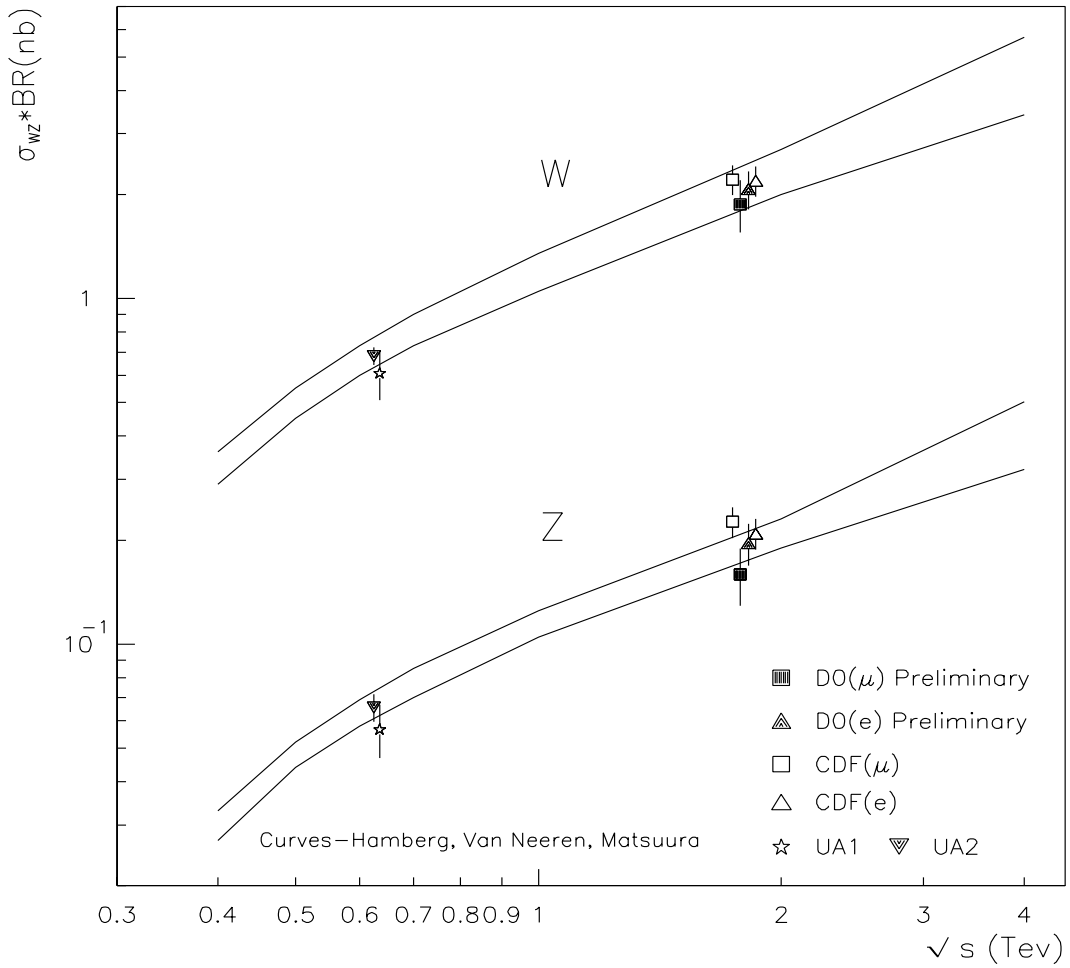

Figure 7.5: Comparison of the obtained cross sections with other experimental results [55] and theoretical expectations [54]. The two curves are the extremes obtained with different parton density functions.

with different parton density functions. CTEQ2M was used to determine the central value and the error band was given by CTEQ2MS, CTEQ2MF, CTEQ2ML, MRSS0', MRSD0', and MRSD-'.

7.3 Measurement of R and Γ_W

The largest source of uncertainty in the measurements of the cross sections themselves are the systematic uncertainties in the efficiency and luminosity calculations. These uncertainties can be reduced by measuring the ratio of the production cross sections, since some of the errors are common to both measurements and therefore cancel in the ratio. For instance, since the $W \rightarrow \mu\nu$ and $Z \rightarrow \mu\mu$ samples are selected as events passing the same trigger requirement, the uncertainty in the luminosity measurement cancels completely. Similarly, applying the same muon identification to the muon produced in the $W \rightarrow \mu\nu$ decay and to one of the two muons produced in the $Z \rightarrow \mu\mu$ decay produces a partial cancellation of the acceptance and efficiency errors. The error cancelation in the determination of R is done with a Monte Carlo program that keeps track of the different correlations.

Based on the cross sections obtained in the previous section, the value for their ratio is:

$$R \equiv \frac{\sigma B(W \rightarrow \mu\nu)}{\sigma B(Z \rightarrow \mu\mu)} = 12.0^{+1.8}_{-1.4}(stat) \pm 1.0(sys).$$

Figure 7.6 shows a comparison with values obtained by other experiments [55, 56].

The ratio R is of interest for other reasons as well since it can be expressed as the following combination of precisely measurable or calculable quantities:

$$R \equiv \frac{\sigma B(W \rightarrow \mu\nu)}{\sigma B(Z \rightarrow \mu\mu)} = \frac{\sigma(\overline{p}p \rightarrow W + X)}{\sigma(\overline{p}p \rightarrow Z + X)} \; \frac{,(W \rightarrow \mu\nu)}{,(Z \rightarrow \mu^+\mu^-)} \; \frac{,_Z}{,_W}. \tag{7.1}$$

The measured value for the Z width is obtained from the LEP experiments [15]

$$,_Z = 2.487 \pm 0.010 \text{ GeV/c}^2.$$

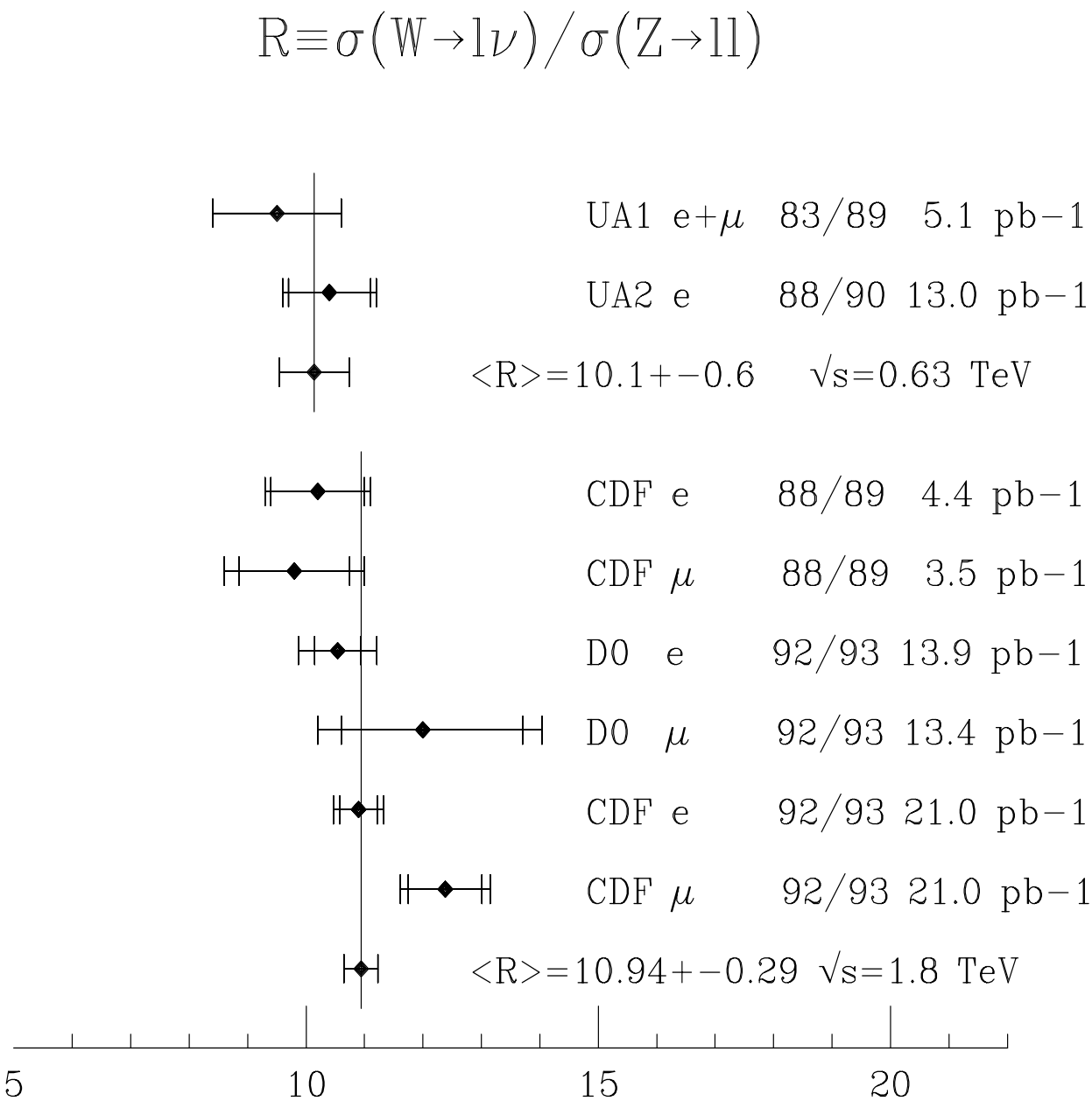

Figure 7.6: Comparison of the obtained cross sections ratio with other experimental results [55,56]. All the 92/93 results, both for DØ and for CDF, are preliminary.

The ratio of the W and Z leptonic decay widths is taken from its theoretical value [57]

$$\frac{,(W \rightarrow \mu\nu)}{,(Z \rightarrow \mu^+\mu^-)} = 2.70 \pm 0.02.$$

The ratio of the W to Z production is determined using the calculation of Hamberg, Van Neerven and Matsuura [54], convoluted with various parton distribution functions [13] to obtain

$$\frac{\sigma(\overline{p}p \rightarrow W + X)}{\sigma(\overline{p}p \rightarrow Z + X)} = 3.26 \pm 0.08.$$

The quoted error corresponds to an error on $,_W$ of 60 MeV, dominated by systematic differences in the structure functions.

Combining these numbers with the quoted value of R in equation 7.1, yields the total width of the W

$$,_W = 1.83 \pm 0.24(stat) \pm 0.15(syst) \pm 0.05(theory + LEPsyst) \text{ GeV}.$$

This result can be compared with the Standard Model prediction [58] of

$$,_W = 2.09 + 0.02 \text{ GeV}$$

for $M_t > M_b + M_W$ where M_t, M_b and M_W are the masses of the top quark, bottom quark and W boson, respectively.

For a top mass below the W mass, the total width of the W would reflect possible decays into top. A limit on the top quark mass, independent of the top quark decay modes, can therefore be extracted from this measurement. Figure 7.7 shows the 95% confidence level limit for $,_W$ based on the measured value presented above. The calculation has been done integrating over the complete range of $,_W$ as well as over the region that excludes non–physical values of $,_W$ corresponding to $M_t > M_W$.

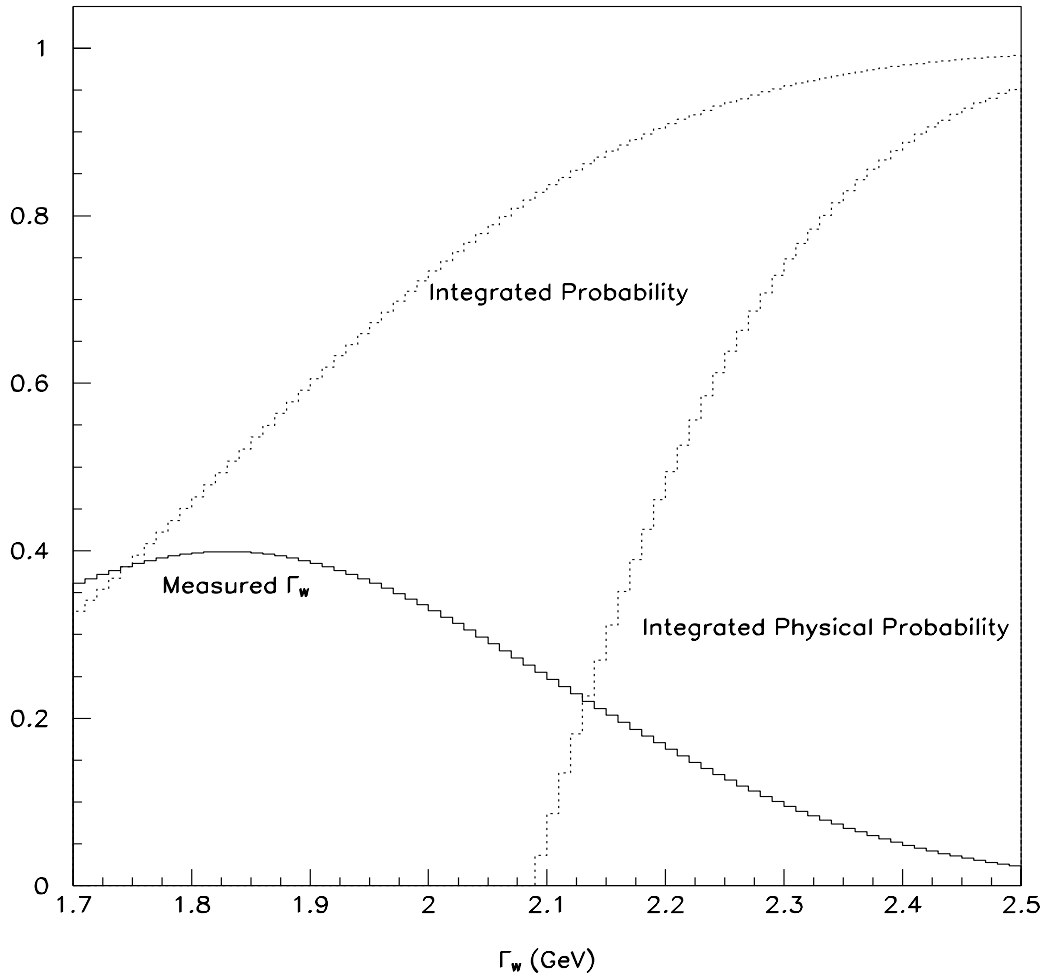

Figure 7.7: The 95% confidence level limit for , $_W$ is obtained integrating over the complete range of , $_W$ and restricting the calculation to the region that excludes non–physical values for , $_W$.

Figure 7.8 shows a prediction for , $_W$ as a function of the top quark mass, together with the limits for , $_W$ as obtained from figure 7.7. The 95% confidence level lower limit on the top mass is extracted from this plot, resulting in 45 GeV when the non–physical values for , $_W$ are excluded and in 58 GeV when the complete range for , $_W$ is taken into account.

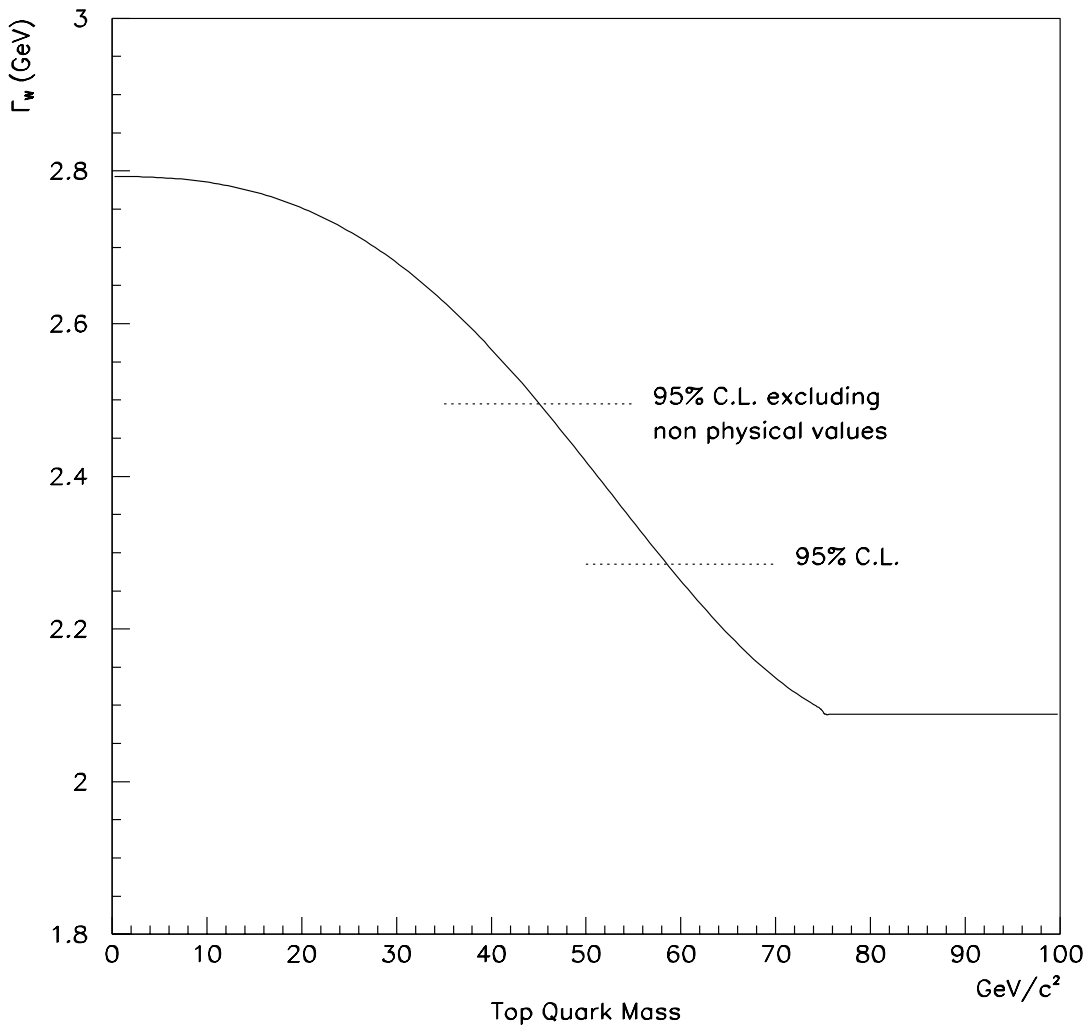

Figure 7.8: , $_W$ is plotted as a function of the top quark mass. Based on the limits for , $_W$ obtained in the previous plot, the 95% confidence level lower limit on the top mass is extracted.

Chapter 8

Conclusions

This thesis described the measurement of $W \to \mu\nu$ and $Z \to \mu\mu$ production cross sections and the derivation of their ratio and the total width of the W boson, based on an integrated luminosity of 13.4 pb^{-1}. As was mentioned earlier, the data corresponds to the complete set recorded during the first collider run of the DØ detector. This analysis thus represents the first use of appropriate trigger configurations and offline muon identification for selecting high p_T isolated muons within the DØ collaboration.

Due to the low performance of the EF chambers during run 1A, the efficiency for detecting and reconstructing muons has been significantly diminished, resulting in reduced event samples for this detector region. Furthermore, the systematic errors arising from the EF chamber efficiency estimation results in larger errors in the final cross section calculations that the ones obtained from statistical origins if the CF only samples are used. For these reasons, the cross section calculations have been obtained from the event samples restricted to the CF region of the WAMUS detector exclusively.

Unfortunately, this corresponds to a very limited acceptance region of the DØ detector (roughly $|\eta_\mu| \leq 0.8$). In addition there is a loss of acceptance due to the

support structure of the detector in the bottom muon chambers. Thus the total geometric acceptance is only $\approx 25\%$ for the $W \rightarrow \mu\nu$ and $\approx 7\%$ for the $Z \rightarrow \mu\mu$ events.

The calculated production cross sections are consistent with expectations, both from theory and from other experimental determinations. The value obtained for the cross sections ratio, R, is about 1σ higher than the average obtained from other CDF and DØ measurements in both the electron and muon channels. The total width of the W boson , $_W$ is consistent with Standard Model predictions for $M_t > M_b + M_W$.

Although the statistical errors resulting from this analysis are higher than the ones expected from the amount of integrated luminosity it is based on, the systematic errors are comparable with other published results ($\approx 9\%$). The limiting factor in the measurement of the cross section ratio is, however, dominated by the number of $Z \rightarrow \mu\mu$ events in the sample.

DØ is currently recording data in a new collider run 1B. The integrated luminosity expected for this period is about three times the one from run 1A. Due to ongoing studies to rise the EF chamber efficiency and the improved understanding of the muon system in the WAMUS–SAMUS overlap region, it is expected to extend the geometrical acceptance for the $W/Z \rightarrow \mu$ analyses out to an $|\eta_\mu|$ of ≈ 2.4 in the near future. The determination of the production cross sections and of their ratio will certainly benefit from the increased number of events when the complete data set for DØ 's run 1 is analysed.

Appendix A

Comparison of efficiencies as derived from data, default Monte Carlo and smeared Monte Carlo.

The efficiency for each of the selection cuts described in section 5.1 is obtained from data through the unbiased muon of the $Z \rightarrow \mu\mu$ sample and from two Monte Carlo $W \rightarrow \mu\nu$ samples: a default detector simulation SHOWER LIBRARY sample, and a sample that has been run through MUSMEAR. The results are shown for CF and EF tracks in table A.1; the efficiencies derived from the data are obtained from the complete run 1A $Z \rightarrow \mu\mu$ sample.

It can be observed that for some of the cuts the discrepancies between the different efficiency estimations are significant; it is a coincidence that the overall efficiency for the combination of cuts used in the $W \rightarrow \mu\nu$ and $Z \rightarrow \mu\mu$ analysis agrees quite well.

The trigger efficiencies as obtained from data (see section 6.1.2) are compared with the ones predicted by the Trigger Simulator when run on MUSMEARed Monte Carlo. The values derived from the data correspond to trigger efficiencies for offline reconstructed tracks. For the comparison to be meaningful, the same

Table A.1: Muon Identification cut efficiencies derived from data, default Monte Carlo and smeared Monte Carlo.

Eff(%) derived from	data		default MC		smeared MC	
Geometric region	CF	EF	CF	EF	CF	EF
Calorimeter Mip	100 ± 1	100 ± 1	92 ± 2	87 ± 2	94 ± 4	85 ± 6
Global Fitting	100 ± 1	82 ± 8	96 ± 2	68 ± 2	97 ± 4	62 ± 5
CD Matching	82 ± 4	92 ± 5	97 ± 2	97 ± 2	96 ± 4	64 ± 5
Impact Parameters	95 ± 2	95 ± 5	93 ± 2	78 ± 2	92 ± 4	82 ± 6
Floating time	94 ± 3	90 ± 7	99 ± 2	99 ± 2	98 ± 4	97 ± 6
Isolation	85 ± 4	86 ± 8	97 ± 2	92 ± 2	98 ± 4	95 ± 6
All cuts	63 ± 5	43 ± 8	71 ± 1	41 ± 2	70 ± 3	42 ± 4

selection has been applied to the Monte Carlo sample. The results are summarized in table A.2 for the CF region only. It can be seen, that the Level 1 $\times$ Level 1.5 efficiency agrees quite well, but this is not the case for the Level 2 efficiency, which differs by $\approx$ 10%. The efficiencies presented in this appendix do not include the prescales that affected the $W \rightarrow \mu\nu$ and $Z \rightarrow \mu\mu$ triggers, and therefore differ from the ones presented in table 6.4.

For the EF region, the determination of the trigger efficiency obtained from data suffers from very few tracks, resulting in large statistical errors.

For the Monte Carlo study, a variation of 1σ in the value of the chamber efficiencies used as input to the MUSMEAR package, produced a variation of 10% in the CF and 40% in the EF Level 1 trigger efficiencies. The version of the Trigger Simulator, which was used for this study, corresponds to the postshutdown trigger configuration.

Table A.2: Muon trigger efficiencies derived from data, default MC, and smeared Monte Carlo, for offline reconstructed tracks. Only statistical errors are shown for the Monte Carlo samples.

Trigger Eff(%)	early pre	late pre	post	def MC	smea MC
Level 1× Level 1.5	48 ± 5	43 ± 5	51 ± 2	62 ± 1	48 ± 2
Level 2	72 ± 7	73 ± 7	88 ± 2	100 ± 1	99 ± 7
Total	34 ± 5	31 ± 5	42 ± 2	62 ± 1	48 ± 4

Appendix B

Summary of Acceptance and Efficiencies.

The different components that contribute to the acceptance and efficiencies are briefly described below and summarized in table B. The numbers are quoted for the CF region only.

- **Acceptance.** This item includes

  1. Eta cut acceptance ($|\eta_\mu| \leq 1$) obtained from ISAJET. Estimated to be 52% for $W \rightarrow \mu\nu$ and 23% for $Z \rightarrow \mu\mu$.
  2. Reco acceptance, calculated from smeared Monte Carlo. This item takes into account the holes that affect the reconstruction of muon tracks and the chamber inefficiency. Estimated to be 77% for $W \rightarrow \mu\nu$ and 58% for $Z \rightarrow \mu\mu$.
  3. Fiducial cut $\int B \cdot dl > 0.6$ GeV, roughly removes the acceptance region $0.8 \leq |\eta_\mu| \leq 1.0$. Estimated to be 84% for $W \rightarrow \mu\nu$ and 71% for $Z \rightarrow \mu\mu$.
  4. Kinematic acceptance, calculated from smeared Monte Carlo, includes the p_T smearing due to chamber resolutions. Estimated in 75% for

Table B.1: Acceptance and Efficiencies affecting the $W/Z \rightarrow \mu$ analysis.

Source	$W \rightarrow \mu\nu$	$Z \rightarrow \mu\mu$
Acceptance(%)	25.1 ± 0.7	6.7 ± 0.4
Trigger Efficiency(%)	39.2 ± 3.0	69.8 ± 3.6
Event Selection(%)	59.6 ± 4.9	78.0 ± 6.2
Prescale	0.88	0.88
Total(%)	5.2 ± 0.6	3.2 ± 0.4

$W \rightarrow \mu\nu$ and 88% for $Z \rightarrow \mu\mu$.

5. Track Angle cuts (applied only in the $Z \rightarrow \mu\mu$ selection). Estimated to be 80% for $Z \rightarrow \mu\mu$.

- **Trigger Efficiency** due to chamber and Level 2 reconstruction inefficiency, also includes the trigger acceptance. As the muon Level 1.5 trigger requires hits in three layers of the muon system, this is more restrictive than the reconstruction that accepts two layer tracks. For this reason a trigger acceptance factor is also included in this item. The prescales affecting the $W/Z \rightarrow \mu$ triggers have been removed.

- **Event Selection.** This item includes:

  1. Offline muon reconstruction, estimated to be 95% for $W \rightarrow \mu\nu$ and 90% for $Z \rightarrow \mu\mu$.

  2. Tight muon selection (applied on either muon of the $Z \rightarrow \mu\mu$). Estimated to be 62% for $W \rightarrow \mu\nu$ and 86% for $Z \rightarrow \mu\mu$.

- **Prescale** includes both Level 1 and Level 2 prescales.

Bibliography

[1] E. Rutherford, Phil. Mag. **21**, 669 (1911)

[2] S. L. Glashow, Nucl. Phys. **B 22**, 579 (1961)

[3] S. Weinberg, Phys. Rev. Lett **19**, 1264 (1967)

[4] A. Salam, in Elementary Particle Theory, edited by N. Svartholm Almqvist and Wiksells, Stockholm, (1968), p. 367

[5] The CDF Collaboration, "Evidence for Top Quark Production in $\overline{p}p$ Collisions at $\sqrt{s} = 1.8\ TeV$", Fermilab–Pub–94/097–E, Submitted to Physical Review **D** April 22, 1994.

[6] B. Hasert et al, Phys. Lett. **B 46**, 138 (1973)
A. Benvenuti et al, Phys. Rev. Lett. **32**, 800 (1973)

[7] C. Rubbia, P. Mc Intyre y D. Cline, in Proc. Int. Neutrino Conf. Aachen, 1976

[8] G. Arnison et al, Phys. Lett. **122 B**, 103 (1983)
M. Banner et al, Phys. Lett. **122 B**, 476 (1983)
P. Bagnaia et al, Phys. Lett. **129 B**, 130 (1983)
G. Arnison et al, Phys. Lett. **129 B**, 273 (1983)

[9] P. Jenni in Proceedings of the 1987 International Symposium in Lepton and Photon Interactions at High Energy.

[10] F. Abe et al, Phys. Rev. Lett. **62**, 1005 (1989)

[11] S. Drell and T. Yan, Ann. Phys. **66**, 578 (1971)

[12] Review of Particle Properties, Physics Letters **B** (1990).

[13] S. Lami and D. Wood, "The W width measurement: an estimate of the error coming from the Structure Functions uncertainties", DØ internal Note # 1462 (1992)

[14] R. Hamberg, W. L. Van Neerven and T. Matsuura, Nucl. Phys. **B 359**, 343 (1991)

[15] The LEP collaborations: ALEPH, DELPHI, L3 and OPAL, Phys. Lett. **B276**, 247 (1992)

[16] Focus on Fermilab, published by the Public Information Office of the Fermi National Accelerator Laboratory.

[17] The DØ Collaboration, "The DØ Detector", Nucl. Instr. and Methods **A 338** issue 2/3, 185–253 (1994).

[18] R. Partridge and B. Lanou, "The Level 0 Trigger", DØ internal Note # 477 (1986)

[19] Amos **et** al. Phys. Lett. **B 243**, 158 (1990)

[20] R. Partridge, "How does DØ measure luminosity?", DØ internal Note # 1788 (1993)

[21] R. Madaras, "DØ W/Z Physics Group Meeting Transparencies", DØ internal Note # 1788 (1993)

[22] J. M. Butler, "Main Ring Deadtime", DØ internal Note # 1682 (1993)

[23] W. J. Thompson, "Search for the Top Quark in the Muon + Jets Channel at DØ ", PhD Thesis (1994)

[24] Chris Klopfenstein, private comunication.

[25] Jaehoon Yu, "Determination of the Strong Coupling Constant α_s and a Test of Perturbative QCD Using W + Jets Processes in the DØ Detector", PhD Thesis (1993)

[26] Freedy Nang, private comunication.

[27] D. Hedin, Muon Reconstruction Note. Online DØ documentation D0$MUON_UTIL$ROOT:[SOURCE]MUON_ANALYSIS.MEM (1992)

[28] T. Hu, "How to find the most important measurement in Least–Square Fit and its application in the muon momentum determination at DØ ", DØ internal Note # 1811 (1993)

[29] D. Zieminska, private comunication.

[30] R. Astur, "A study of the ability of the DØ detector to measure the single jet inclusive cross section" PhD Thesis (1992)

[31] N. J. Hadley, "Cone Algorithm for Jet Finding", DØ internal Note # 904 (1989)

[32] M. Paterno, "A Monte Carlo Study of the DØ Calorimeter Missing E_T Resolution", DØ internal Note # 1374 (1992)

[33] R. Avery et al., "DØ Event Display Users Guide", DØ internal Note # 1355 (1992)

[34] F. Paige and S. Protopopescu, "ISAJET: a Monte Carlo Event Generator for pp and $\overline{p}p$ Reactions", Brookhaven National Laboratory (1987).

[35] Torbjön Sjöstrand, "Pythia 5.6 physics manual", CERN TH 6488/92 (1992)

[36] R. D. Field and R. P. Feynman, Nucl. Phys. **B136**, 1 (1978)

[37] F. Carminati et al. "GEANT User's Guide", CERN Program Library (1991)

[38] W. Womersley, R. Raja and A. Jonckheere, "Shower Libraries for DØ GEANT Monte Carlo", DØ internal Note # 650 (1987)

[39] W. Dharmaratna, R. Raja and C. Steward, "Shower Library Version 2.0", DØ internal Note # 1730 (1993)

[40] "Level 1 simulation user's guide", Online DØ documentation, D0$LEVEL1:L1SIM.DOC (1992)

[41] D. Claes, "Level 2 simulation user's guide", Online DØ documentation, D0$LEVEL2$DOCS:L2SIM.DOC (1991)

[42] H. T. Diehl, "Level 2 Muon Filter in Run 1A", DØ internal Note # 1887 (1993)

[43] P. Quintas and D. Wood,"Muon Offline Calibration Procedures for T_0 and ΔT Constants in run 1A", DØ internal Note # 2103 (1994)

[44] C. Gerber, P. Quintas, "Muon Momentum Resolution from DØ Reco v10", DØ internal Note # 1985 (1993)

[45] D. Hedin, P. Quintas and D. Wood, "Muon Wide Angle Chamber Efficiencies in Run 1A", DØ internal Note # 2127 (1994)

[46] The DØ Collaboration, "Search for the Top Quark in $\overline{p}p$ collisions at $\sqrt{s} = 1.8\,TeV$", Phys. Rev. Lett. **72**, 2138 (1994)

[47] C. Gerber, P. Quintas, D. Wood, "Updated status report on cross section measurements of W and Z to muons at DØ ", DØ internal Note # 1904 (1993)

[48] D. Hedin, "Preliminary DØ punchthrough rates", DØ internal Note # 1738 (1993)

[49] C. Gerber, P. Quintas, D. Wood, "Status report on cross section measurements of W and Z to muons at DØ ", DØ internal Note # 1718 (1993)

[50] H. T. Diehl, "Cosmic Ray Muon Rejection in the Level 2 Filter at DØ ", DØ internal Note # 1517 (1992)
H. T. Diehl, "Updates to Cosmic Ray Muon Rejection in MUON_L2 ", DØ Internal Note # 1517A (1993)

[51] D. Wood, D0WZSOURCE:MUCTAG_TRK.FOR

[52] D. Hedin, "Eye scanning for unbiased events", USR$ROOT3:[HEDIN]SCANXXX.DOC, Online DØ documentation (1993)

[53] T. Heuhn, "A Study of $\pi/K \rightarrow \mu\nu$ In-Flight Decay Backgrounds in the Central Region, $|\eta| < 0.76$", DØ Internal Note # 1288 (1992)

[54] R. Hamberg, W. L. Van Neerven and T. Matsuura, Nucl. Phys. **B359**, 343, (1991)

[55] C. Albajar et al. Phys. Lett. **B 253**, 503 (1991)
J. Alitti et al. Phys. Lett. **B 276**, 365 (1992)
F. Abe et al. Phys. Rev. **D 69**, 28 (1992)
F. Abe et al. Phys. Rev. **D 44**, 29 (1991)
The DØ Collaboration: Preliminary results presented in the general meeting of the APS (1994).

[56] The CDF Collaboration: Preliminary results presented in Tokyo HEP INS (1994)
The DØ Collaboration: Preliminary results presented in the general meeting of the APS (1994)

[57] W. F. Hollik, Firtschr. Phys. **38**, 165 (1990)

[58] The calculation of , $_W$ has been redone with updated values for the masses of the W and Z bosons using the program provided by T. Alvarez, A. Leites and J. Terrón, Nucl. Phys. **B 301** 1 (1988)